Instrumentation of a 2.6 THz heterodyne receiver

Fabien Defrance

UNIVERSITÉ PIERRE ET MARIE CURIE

THÈSE DE DOCTORAT

Spécialité : Méthodes Instrumentales en Astrophysique et leurs Applications Spatiales

Présentée par

Fabien DEFRANCE

Pour l'obtention du grade de docteur de l'université Pierre et Marie Curie

---

Instrumentation d'un récepteur hétérodyne à 2.6 THz

Thèse soutenue le 14 décembre 2015 devant un jury composé de :

M. Aziz BENLARBI-DELAÏ	L2E	Président du jury
M. Paul CROZAT	IEF	Rapporteur
M. Alessandro NAVARRINI	INAF	Rapporteur
Mme. Martina WIEDNER	LERMA	Directrice de thèse
M. Massimiliano CASALETTI	L2E	Examinateur
Mme. Christine LETROU	Télécom SudParis	Examinatrice
M. Julien SARRAZIN	L2E	Invité

Thèse préparée à l'Observatoire de Paris, au Laboratoire d'Études du Rayonnement de la Matière en Astrophysique et Atmosphères (LERMA)

Résumé

Les observations astronomiques nous permettent d'étudier l'univers et de comprendre les phénomènes qui le gouvernent. La matière visible dans l'univers émet des ondes à des fréquences très diverses, réparties sur tout le spectre électromagnétique (domaines radio, submillimétrique, infrarouge, visible, ultraviolet, X et gamma). Ces ondes nous renseignent sur certaines caractéristiques physico-chimiques des éléments observés (nature, température, mouvement, etc.). Des télescopes couvrant différentes plages de fréquences sont nécessaires pour observer l'ensemble du spectre électromagnétique. Les radio-télescopes, sensibles aux ondes (sub)millimétriques, sont principalement dédiés à l'observation de la matière froide présente dans le milieu interstellaire. Le milieu interstellaire est le berceau des étoiles et son étude est essentielle pour comprendre les différentes étapes de la vie des étoiles. La fréquence maximale d'observation des radio-télescopes est en augmentation depuis la fabrication des premiers radio-télescopes dans les années 1930. Récemment, des radio-télescopes capables de détecter des signaux dans l'infrarouge lointain, au delà de 1 THz, ont été développés. Ces avancées technologiques ont été motivées, entre autres, par la présence, dans le milieu interstellaire, de molécules et d'ions uniquement observables à des fréquences supérieures à 1 THz. Pour observer des raies avec une haute résolution spectrale, les radio-télescopes sont équipés de récepteurs hétérodynes. Ce type de récepteur permet d'abaisser la fréquence de la raie spectrale observée tout en conservant ses caractéristiques (une raie observée à 1 THz peut, par exemple, être décalée à une fréquence de 1 GHz). Cette technique permet d'observer des raies avec une très haute résolution spectrale et c'est pourquoi les récepteurs hétérodynes sont largement utilisés pour les observations de raies spectrales aux fréquences GHz et THz. Dans les récepteurs hétérodynes, un oscillateur local (OL) émet un signal monochromatique à une fréquence très proche de celle du signal observé. Les deux signaux sont superposés à l'aide d'un diplexeur et transmis à un mélangeur. Ce dernier réalise le battement des deux signaux et génère un signal identique au signal observé mais à une fréquence plus faible.

Durant ma thèse, j'ai travaillé sur la construction, la caractérisation et l'amélioration d'un récepteur hétérodyne à 2.6 THz. Cette fréquence d'observation (2.6 THz) est l'une des plus hautes atteintes par les récepteurs hétérodynes THz existant actuellement, ce qui constitue un défi technologique très important. Dans le but de caractériser et d'améliorer ce récepteur, je me suis concentré sur trois aspects essentiels :

1. *La stabilité* : C'est l'une des caractéristiques principales des récepteurs hétérodynes. Elle est liée au bruit généré par le récepteur et détermine le temps pendant lequel le récepteur peut intégrer le signal reçu sans avoir besoin d'être recalibré. Meilleure est la stabilité du récepteur, plus longtemps il peut intégrer le signal observé et plus le

bruit de la mesure est atténué. La stabilité d'un récepteur peut être caractérisée par la variance d'Allan. Dans ma thèse, je distingue les variances d'Allan totale et spectrale. La variance d'Allan totale permet d'estimer la stabilité en puissance du récepteur sur l'ensemble de sa bande passante. La variance d'Allan spectrale donne une estimation de la stabilité de la forme du spectre (on considère la variation des canaux de fréquences les uns par rapport aux autres). À l'aide de ces deux types de variances d'Allan, j'ai pu calculer la stabilité de notre récepteur et conclure qu'avec notre oscillateur local à 600 GHz elle est comparable à celle d'autres récepteurs hétérodynes internationaux comme GREAT et HIFI. En mesurant la stabilité des différents éléments du récepteur, j'ai pu en déduire que l'oscillateur local à 1.4 THz et l'alimentation de notre mélangeur étaient les principales sources d'instabilités.

2. *Le diplexeur* : Cet élément permet de coupler le signal observé avec celui de l'oscillateur local (OL). Le but du diplexeur est de transmettre le maximum de puissance du signal observé et suffisamment de puissance de l'OL pour permettre un fonctionnement optimal du mélangeur. Le diplexeur le plus couramment utilisé aux fréquences THz est un film semi-réfléchissant en Mylar®. Il transmet généralement environ 90 % du signal observé et réfléchit environ 10 % du signal de l'OL. À des fréquences inférieures à 1 THz, les OL émettent assez de puissance pour que 10 % suffisent au fonctionnement du mélangeur. Pour notre récepteur à 2.6 THz, cette méthode n'est pas envisageable car les OL standards n'émettent pas assez de puissance. J'ai donc conçu, testé et amélioré un autre type de diplexeur, un interféromètre de Martin-Puplett. Cet interféromètre utilisant deux grilles polarisantes, deux miroirs en toit et un miroir ellipsoïdal pour focaliser le signal de l'OL, peut théoriquement transmettre à la fois le signal observé et celui de l'OL avec très peu de pertes. J'ai donc conçu et caractérisé les différents éléments de l'interféromètre avant de les assembler et de mesurer l'efficacité globale de l'interféromètre. Cela m'a permis d'obtenir une transmission de 76 % du signal de l'OL et d'estimer la transmission du signal observé à 79 % environ. Cet interféromètre est donc opérationnel pour être utilisé dans notre récepteur hétérodyne à 2.6 THz. De plus, les mesures des différents éléments de l'interféromètre m'ont permis de déterminer quels éléments généraient le plus de pertes. Ainsi, le remplacement des grilles polarisantes devrait permettre une amélioration de l'efficacité de notre interféromètre de Martin-Puplett à 2.6 THz.

3. *Le réseau de phase* : Il est utilisé pour diviser le faisceau de l'OL en plusieurs faisceaux et permettre la fabrication de récepteurs hétérodynes à plusieurs pixels. Les récepteurs hétérodynes ne comportent généralement qu'un seul pixel. Pour augmenter le nombre de pixels, il est nécessaire d'utiliser plusieurs mélangeurs qui doivent, chacun, recevoir un signal de l'OL couplé avec une partie du signal observé. Pour permettre la création d'un récepteur hétérodyne multi-pixel, j'ai conçu et testé un nouveau type de réseau de

phase, que nous avons appelé *Réseau de phase global*, permettant de diviser le faisceau de l'OL en plusieurs faisceaux. J'ai développé un programme numérique pour calculer des profils de réseaux de phase permettant de générer le nombre souhaité de faisceaux avec une excellente efficacité. Les profils de phase générés par ce programme n'ont pas de contrainte géométrique, à la différence des réseaux de phase actuellement utilisés aux fréquences THz, les réseaux de Dammann qui ont une géométrie discrète, et les réseaux de Fourier qui ont une géométrie continue. Les Réseaux de phase globaux que j'ai développés peuvent être non-périodiques et pourraient également avoir d'autres applications, comme modifier la forme d'un faisceau. J'ai réalisé deux prototypes de Réseaux de phase globaux divisant le faisceau de l'OL en quatre faisceaux et fonctionnant à 600 GHz. Les deux prototypes sont basés sur le même design, mais l'un fonctionne en transmission (il est en TPX®, un plastique assez transparent à 600 GHz), et l'autre, en laiton, fonctionne en réflexion. J'ai pu vérifier et améliorer l'efficacité théorique de ces prototypes avec FEKO, un logiciel de simulation électromagnétique. Les deux prototypes ont été réalisés par une société extérieure et testés dans notre laboratoire à 600 GHz. J'ai mesuré une efficacité de 76 ± 2 % pour le prototype en réflexion, et 62 ± 2 % pour le prototype en transmission. Ces valeurs sont très bonnes et la correction d'une erreur d'usinage sur le réseau en transmission devrait encore augmenter son efficacité. L'efficacité de ces prototypes de Réseaux de phase globaux est parmi les meilleures au monde pour les fréquences THz, et de prochains prototypes à 1.4 THz et 2.6 THz sont prévus.

Finalement, le travail accompli durant cette thèse de doctorat constitue une étape importante vers la réalisation d'un récepteur hétérodyne multi-pixel à 2.6 THz utilisant un interféromètre de Martin-Puplett comme diplexeur, et possédant de très bonnes caractéristiques de stabilité et de sensibilité. Ce futur récepteur hétérodyne pourrait être utilisé dans d'importants projets internationaux comme CIDRE, Millimetron, CCAT, GUSSTO ou THEO.

Mots clés : Récepteur hétérodyne, térahertz, THz, Martin-puplett, variance d'Allan, réseau de phase, stabilité, multi-pixel, oscillateur local, diplexeur, optique gaussienne, quasioptique, réseau de Dammann.

Abstract

(Sub)Millimeter-telescopes are often used to observe the interstellar medium in the universe and they enable us to study the stellar life cycle. To detect and study some important molecules and ions, we need receivers able to observe at frequencies above 1 THz. Receivers working at such high frequencies are quite new and the 2.6 THz heterodyne receiver I built and characterized during my PhD represents the state-of-the-art of THz heterodyne receivers. I especially focused on three important aspects of this receiver: its stability, the superimposition of the local oscillator signal (LO) and the observed signal by a diplexer, and the splitting of the LO signal by a phase grating. The stability was calculated with the Allan variance and I found that the two elements limiting the stability of our receiver were the 1.4 THz local oscillator and the mixer bias supply. The Martin-Puplett interferometer (MPI) diplexer I designed, built and tested is able to transmit 76 % of the LO power at 2.6 THz and we estimate a transmittance around 79 % for the observed signal. This MPI is operational and ready for the next generation of heterodyne receivers. Splitting the LO signal is essential to build heterodyne receivers with several pixels, which allows us to get spectra of the universe at many positions in the sky simultaneously. I have developed a new kind of grating, called *Global gratings*, and I made two prototypes of these Global phase gratings able to split the LO beam into four beams. These two phase grating prototypes, a transmissive and a reflective one, were optimized for 610 GHz and showed, respectively, an efficiency of 62 ± 2 % and 76 ± 2 %. These excellent results validate the design and fabrication processes of this new kind of grating. In conclusion, the work accomplished during this PhD constitutes an important step toward the realization of a very stable and highly sensitive 2.6 THz multi-pixel heterodyne receiver using a MPI diplexer.

Key words: Heterodyne receiver, THz, Martin-Puplett, Allan variance, phase grating, stability, multi-pixel, local oscillator, diplexer, Gaussian optics, quasioptics, Dammann grating.

Acknowledgements

Je tiens à remercier Martina Wiedner, ma directrice thèse, pour son aide et son soutien tout au long de cette thèse, ainsi que pour ses qualités humaines et scientifiques. Je lui suis très reconnaissant de la grande liberté qu'elle m'a laissé durant ces trois années, ainsi que de l'opportunité qu'elle m'a donné de participer à des conférences aux Pays-Bas, en Russie et aux Etats-Unis, ainsi qu'à une semaine d'observation au 30m de l'IRAM. Je tiens aussi à remercier Paul Crozat et Alessandro Navarrini qui ont accepté d'être les rapporteurs pour ma soutenance de thèse, et dont les commentaires m'ont été très précieux. Je remercie également Aziz Benlarbi-Delaï, Martina Wiedner, Massimiliano Casaletti, Christine Letrou et Julien Sarrazin pour avoir accepté de faire partie du jury. Je remercie aussi l'ensemble des personnes du LERMA pour leur accueil chaleureux, en particulier l'équipe du bâtiment Lallemand qui m'a aidé et supporté durant ces trois années. Merci à Grégory Gay, pour sa disponibilité, son aide précieuse, sa bonne humeur, mais aussi pour ses goûts musicaux qu'il m'a fait partager et pour certaines expériences à base d'azote liquide. Merci à Yan Delorme pour ses nombreux conseils et son soutien, à Alexandre Ferret pour l'esprit de travail si particulier que nous avons réussi à développer dans notre bureau, à Michèle Batrung pour son soutien culinaire, à Maurice Gheudin pour ses idées et ses coups de main, à Jean-Michel Krieg pour sa confiance. Je remercie également les nouveaux arrivants, Anastasia Penkina, Duccio Delfini et François Joint, d'avoir contribué à la création du bureau des doctorants, assurément la plus belle pièce du bâtiment Lallemand. Je remercie également Thibault Vacelet et Roland Lefèvre, dont les compétences en micro-imagerie m'ont été très utiles, ainsi que Faouzi Boussaha, Christine Chaumon et Alain Maestrini pour leurs conseils et les moments passés ensemble lors de conférences. Je tiens aussi à remercier Die Wang pour m'avoir permis de ne pas trop perdre mon chinois et pour son poulet au coca, Jordane Mathieu pour son gateau de l'amitié qui faisait beaucoup de bulles, ainsi que Shanna Li pour son atelier de raviolis chinois. Je tiens à remercier Laurent Pelay et les personnes de l'atelier de mécanique qui m'ont été d'une aide précieuse durant toute la durée de la thèse pour réaliser divers éléments mécaniques et optiques. Je remercie également toutes les autres personnes de l'Observatoire que j'ai côtoyées et qu'il serait trop long de citer. Je tiens à remercier l'équipe du L2E à l'UPMC qui m'a accueilli, et plus particulièrement Julien Sarrazin et Massimiliano Casaletti dont les conseils m'ont été très précieux pour développer des réseaux des phase. Je n'oublie pas non plus toute l'équipe d'Astro-jeunes, dont la réussite tient très certainement à sa grande proportion d'auvergnats, avec qui j'ai participé au festival d'astronomie de Fleurance. Merci à vous Nicolas Laporte, Simon Nicolas, Aurélia Bouchez, Laurianne Palin, Gabriel Foenard, Ilane Schroetter, Philippe Peille, Vincent Heussaff, David Quénard, William Rapin, Nicolas Vilchez, Arnaud Beth, Claire Divoy et Jason Champion. Je remercie aussi Thierry Duhagon

pour son investissement dans le festival, ainsi que Julie Gourdet sans qui je n'en aurais jamais eu connaissance. Je remercie aussi le CNES qui à financé ma thèse, et Gilles Cibiel mon responsable au CNES. Je suis également reconnaissant à Pierre Martin-Cochet et Paul Ho, de l'ASIAA, dont le rôle a été déterminant dans l'obtention de cette thèse. Je remercie aussi Hugh Gibson pour m'avoir beaucoup aidé dans mes simulations électromagnétiques et pour m'avoir fait découvrir qu'il pouvait exister du bon cheddar. Merci à Serena Wong pour son soutien et ses mails à rallonge qui pourraient remplir plusieurs thèses, et merci à Edwige Chapillon pour m'avoir fait découvrir Grenoble depuis les airs. Finalement, je tiens tout particulièrement à remercier mes parents qui m'ont toujours soutenu et encouragé, et qui m'avaient offert, il y a maintenant plus de vingt ans, un livre sur le système solaire. Encore merci. Enfin, je pense à toi mon Schtroumpf qui commence ta thèse, bon courage!

Contents

Abbreviations

Technical terms

2SB	Two Side Bands
CAD	Computer Aided Design
DFTS	Digital Fourier Transform Spectrometer
DG	Dammann Grating
DSB	Double Side Band
FFT	Fast Fourier Transform
HDPE	High Density Polyethylene
HEB	Hot Electron Bolometer
HRFZ Si	High Resistivity Float Zone Silicon
IF	Intermediate Frequency
ISM	Interstellar medium
LO	Local Oscillator
LSB	Lower Side Band
MPI	Martin-Puplett Interferometer
QCL	Quantum Cascade Laser
RF	Radio Frequency
SEM	Scanning Electron Microscope
SSB	Single Side Band
USB	Upper Side Band

Laboratories

IRAM	Institut de RadioAstronomie Millimetrique
LERMA	Laboratory for Studies of Radiation and Matter in Astrophysics
LPN	Laboratory of Photonics and Nanostructures

MPQ	Materials and Quantum Phenomena

Telescopes and instruments

ALMA	Atacama Large Millimeter/sub-millimeter Array
APEX	Atacama Pathfinder Experiment
CCAT	Cerro Chajnantor Atacama Telescope
CHAMP	Carbon Heterodyne Array of the MPIfR
CIDRE	Deuterium Identification Campaign by hEterodyne Reception
COBE	Cosmic Background Explorer
CONDOR	CO N+ Deuterium Observations Receiver
EMIR	Eight MIxer Receiver
GREAT	German REceiver for Astronomy at Terahertz frequencies
GUSSTO	Galactic/Xgalactic Ultra long duration balloon Spectroscopic Stratospheric THz Observatory
HHT	Heinrich Hertz Telescope
HIFI	Heterodyne Instrument for the Far-Infrared
KAO	Kuiper Airborne Observatory
KOSMA	Koelner Observatorium fuer SubMillimeter Astronomie
MPIfR	Max Planck Institute for Radio Astronomy
NOEMA	NOrthern Extended Millimeter Array
RLT	Receiver Lab Telescope
SMART	Sub-Millimeter Array Receiver for Two frequencies
SOFIA	Stratospheric Observatory for Infrared Astronomy
Desert STAR	Submillimeter Telescope Array Receiver
STO	Stratospheric THz Observatory
THEO	Terahertz Heterodyne Observatory
upGREAT	Extension of GREAT receiver

Chapter 1

Introduction

Nearly all astronomical observations rely on electromagnetic waves. Our knowledge of the Universe has long been based on optical observations. However, since the last century, enormous technological advances enabled us to observe nearly the whole frequency spectrum. The emergence of radio transmissions led to the development of astronomical receivers for radio and sub-millimeter waves. At these frequencies, we are especially sensitive to the emission of cold matter, principally located in the interstellar medium (ISM). The ISM contains molecular clouds where stars and planetary systems are created. Therefore, radio and sub-millimeter astronomical receivers are essential to understand the stellar life cycle. They also allow us to study the composition of molecular clouds in the Universe. Until now, technological progress continuously increased the maximum observation frequency of sub-millimeter receivers. Very recently, the first receivers above 1 THz have been built. Such receivers are used to explore the far-infrared gap which is the frequency range located between infrared and THz frequencies (figure 1.1). This frequency range has, so far, been little observed by astronomers and it is one of the last parts of the spectrum remaining mostly unexplored.

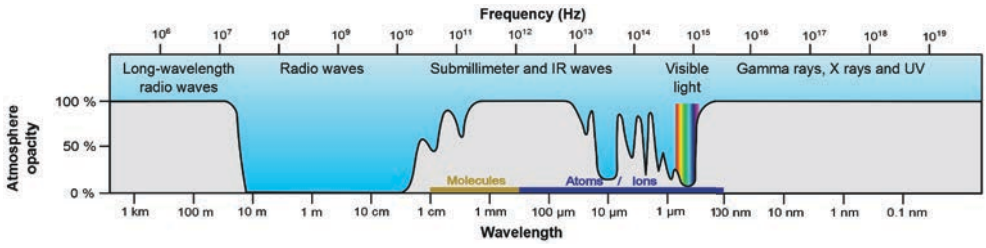

FIGURE 1.1: Transmission of the atmosphere over the spectrum

As shown on figure 1.1, far infrared radiation is mostly absorbed by the Earth atmosphere, due to the presence of water vapor. Thus, all receivers observing at frequencies above 1 THz must operate from very high altitudes (high mountain, plane, stratospheric balloon or satellite).

Two kinds of receivers exist at THz frequencies. Bolometers, which measure the total power received over a large frequency range; and heterodyne receivers, which can generally achieve a very high spectral resolution and are especially used for spectral line observations. At millimeter and sub-millimeter wavelengths, it is possible to detect rotational or vibrational lines of many molecules, as well as fine structure lines of ions. The observation of molecular transitions allows us to determine many physical and chemical characteristics of molecular clouds. The THz spectrum, which remains partly unexplored, contains a few very important lines not observable at lower frequencies (except for OH): N^+ (1.46 THz), C^+ (1.90 THz), OH (2.51 THz), HD (2.68 THz) and OI (4.75 THz).

- The fine structure line of N^+ at 1.46 THz is the third strongest cooling line in our galaxy, as observed by the telescope COBE. N^+ is a marker of the warm ionized medium.
- C^+ has also been observed by COBE. It is the strongest line of our galaxy and the most important ISM cooling line in the frequency range of COBE. C^+ is seen in all the phases of the ISM: the ionized medium, the cold neutral medium and the moderately dense molecular medium.
- Deuterium is one of the primordial elements which has been exclusively created in the Big Bang. In the universe, the D/H (deuterium/hydrogen) ratio decreases, as deuterium is burned by stars but never created. Thus, the D/H ratio is a measure of the history of star formation since the creation of the Universe. Measurements of HD can be used to calculate the D/H ratio, or if the ratio is known, HD can be used as a tracer for H_2.
- The OH molecule is a fundamental tracer for the understanding of the oxygen chemistry and the formation of water. The abundance of OH is linked to that of H_2O and O_2 in the ISM. Thus, OH observations are essential to study the numerous aspects of the interstellar chemistry for oxygen and water.
- Neutral atomic oxygen OI can be used to trace diffuse molecular gas and it is also a major coolant of the dense interstellar medium. Moreover, it is used to study the

physical conditions in the photo-dissociation regions (PDR) around massive young stars.

Therefore, the interest in observing these spectral lines motivates the development of heterodyne receivers above 1 THz.

This PhD thesis was initially dedicated to the CIDRE project, a heterodyne receiver whose goal was to observe HD and OH at 2.68 THz and 2.74 THz. As these frequencies are mostly absorbed by the atmosphere, CIDRE was planned to be carried by a stratospheric balloon, to observe the interstellar medium from an altitude of 40 km. The CIDRE project was suspended for budget reasons in 2014. However, this PhD remained dedicated to the development and improvement of a 2.6 THz multi-pixel prototype heterodyne receiver, because similar receivers will be required for future radio-telescope projects, like Millimetron [1], CCAT [2] and GUSSTO. A satellite project named THEO (THz heterodyne observatory) has been recently proposed by Gerin and Wiedner (Paris Observatory, LERMA). The target lines of this instrument are C^+, N^+ and OI, and its development will directly benefit from this PhD work. The development of a heterodyne receiver at such high frequencies is technically very challenging.

During my PhD, I developed, built and characterized a 2.6 THz prototype receiver that represents the state-of-art of THz heterodyne receivers. In particular, I studied three aspects of my prototype heterodyne receiver:

1. The stability of the receiver and its components.
2. The optics, by designing, building and testing a Martin Puplett interferometer.
3. The distribution of the local oscillator beam, for which I designed and tested two phase grating prototypes.

The next chapter (chapter 2) starts with an introduction of heterodyne receivers, followed by a complete description of our 2.6 THz receiver and a detailed presentation of the other chapters of this thesis. Then, the three main subjects of my thesis, listed above, are developed in detail in chapters 3, 4 and 5. Each of these chapters focuses on a specific aspect of our 2.6 THz heterodyne receiver. Finally, this thesis finishes with a conclusion of my work in chapter 6.

Chapter 2

Terahertz heterodyne receivers

2.1 Motivation

Heterodyne receivers have revolutionized radio astronomy and receivers for higher and higher frequencies have been built. Recently the first heterodyne receivers above 1 THz have been built and tested. For my thesis, I have built characterized and improved a prototype receiver at 2.6 THz for the next generation of space-borne telescopes.

This chapter provides the reader with background information concerning THz heterodyne receivers, useful to understand the other chapters of this thesis. This chapter is divided into different parts. It starts with a brief description of existing heterodyne receivers above 1 THz. Then, I describe the functioning and main characteristics of standard heterodyne receivers, and I detail the different elements constituting THz heterodyne receivers. Finally, the last part of this chapter contains a complete description of our 2.6 THz heterodyne receiver, and a presentation of the different aspects of my thesis.

2.2 THz heterodyne receivers in astronomy

2.2.1 Main characteristics of heterodyne receivers

Heterodyne receivers are an essential part of radio-astronomy and have lead to a wealth of discoveries. In contrast to bolometers, they usually have a very high spectral resolution

and are ideally suited to observe line emissions, from which we can deduce the physical and chemical conditions of the interstellar medium.

2.2.2 Overview of existing THz heterodyne receivers

Several THz heterodyne receivers operating above 1 THz are already working on ground based and space based telescopes, some of them are listed below and are shown in figure 2.1. They are all using HEB mixers (cf. section 2.4.1), except the first one, KAO's receiver, which was using a Schottky diode mixer, less sensitive but covering a larger bandwidth than HEBs.

- The Kuiper Airborne Observatory (KAO) started observing in 1975 and it has been operating during 20 years, before being replaced by SOFIA. It was carrying a 91 cm diameter primary reflector and was operating from a plane. The heterodyne receiver of KAO was able to observe from 700 GHz to 3 THz (cf. Röser [3]).
- The Receiver Lab Telescope (RLT) has been intermittently operating since 2002 from an altitude of 5525 meters, on Cerro Sairecabur, in Chile. It has been the first ground based telescope to observe at frequencies above 1 THz (cf. Marrone et al. [4]).
- CONDOR (CO N+ Deuterium Observations Receiver) was the first ground based heterodyne receiver to be tested on a large telescope, the APEX 12m telescope, in 2006. It observed at frequencies between 1.25 THz and 1.53 THz [5][6]. The APEX telescope is also located in the Chilean Andes (Llano de Chajnantor) at an altitude of 5105 meters.
- The HIFI (Heterodyne Instrument for the Far-Infrared) instrument of Herschel satellite started observing in early 2010, from space [7][8][9]. It covers frequency ranges between 488 GHz and 1272 GHz, and between 1430 GHz and 1902 GHz.
- The GREAT (German REceiver for Astronomy at Terahertz frequencies) [10] and upGREAT [11] instruments are two heterodyne receivers which have been operating on SOFIA airplane observatory [12], since 2012 and 2015 respectively. These two heterodyne receivers cover different frequency windows between 1.25 THz and 4.7 THz.
- The Stratospheric THz Observatory (STO) [13] has an heterodyne receiver embedded below a stratospheric balloon which can observe from an altitude of 38 km. A new version of this balloon, STO-2 [14] will be launched in late 2015 and will be able to observe three frequency bands centered on 1.4 THz, 1.9 THz and 4.7 THz.

(A) KAO

(B) RLT

(C) APEX

(D) Herschel

(E) SOFIA

(F) STO

FIGURE 2.1: Pictures of different heterodyne receivers operating above 1 THz
Credits:
(A): NASA
(B): D. Marrone (https://www.cfa.harvard.edu)
(C): http://www.apex-telescope.org
(D): ESA (Image by AOES Medialab)
(E): http://www.nasa.gov
(F): Christopher Walker/U.S. Antarctic Program

2.3 General principle of heterodyne receivers

2.3.1 The heterodyne principle

Heterodyne receivers mix the sky signal (also called radio frequency (RF) signal) with an artificial monochromatic signal created by the local oscillator (LO). The mixing allows the sky signal to be shifted to a different frequency without losing any amplitude or frequency information (figure 2.2).

This feature is particularly interesting in THz astronomy because it enables us to down-convert a radio frequency (RF) signal observed at a few THz, to a few GHz, and process it more easily and with a better spectral resolution. The down-conversion is produced by the combination of the two main components of the heterodyne receiver, the mixer and the local oscillator (LO):

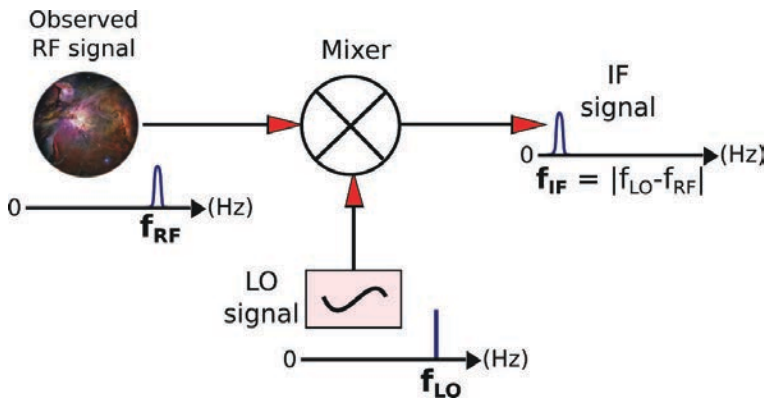

FIGURE 2.2: Principle of the heterodyne detection

- The LO generates a signal at a frequency f_{LO} close to the frequency of the observed RF signal (f_{RF}). The frequency of the signal emitted by the LO must be well known and as monochromatic as possible.
- The mixer is a non-linear device which receives and combines both RF and LO signals. At the output of the mixer, we only select the harmonic corresponding to the frequency difference between the two signals, and call it intermediate frequency (IF) signal ($f_{IF} = |f_{LO} - f_{RF}|$).

If the LO signal is very stable (in frequency and in power) and almost monochromatic, the IF signal will be the same as the RF signal, but at a frequency corresponding to $|f_{LO} - f_{RF}|$, for fundamental mixers (figure 2.2). However, the LO and RF signals need to be superimposed before being sent to an unbalanced fundamental mixer, which is achieved with a coupling element called diplexer. A beam splitter is often used. It reflects a small part of the LO signal (usually around 10 %) and transmits most of the RF signal (usually 90 %).

Finally, the IF signal at the output of the mixer needs to be amplified, filtered, and processed with a spectrometer to obtain a spectrum. Figure 2.3 shows a more detailed schematic of a heterodyne receiver, with a beam splitter diplexer.

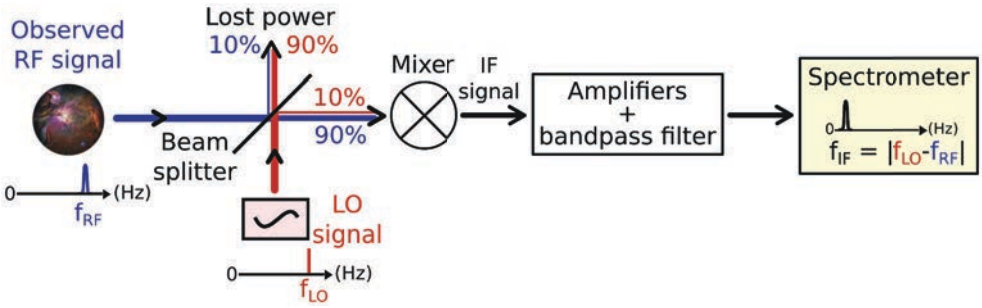

FIGURE 2.3: Schematic of a heterodyne receiver

2.3.2 Sensitivity of heterodyne receivers

2.3.2.1 Noise temperature

The sensitivity of a radio receiver is often measured in terms of noise temperature. The lower the noise temperature, the more sensitive the receiver. The noise temperature of a receiver corresponds to the noise power generated by the receiver in a bandwidth B.

$$T_e = \frac{P}{kB}, \tag{2.1}$$

where P is the noise power at the output of the receiver (in Watts), k the Boltzmann's constant ($k = 1.380 \times 10^{-23}$ J.K^{-1}), T_e the noise temperature in Kelvins, and B the bandwidth in Hertz. For experimental reasons, it is more convenient to express the noise power (P) by its equivalent noise temperature (T_e).

All the components of a heterodyne receiver have a noise temperature which has an influence on the total noise temperature of the receiver. The elements before the first amplifier are the components which noise temperature is the most critical (ie. optics, mixer, cables etc.). Therefore, they mostly determine the total noise temperature of the heterodyne receiver. The noise temperature of the receiver is calculated according to the following formula:

$$T_{noisetot} = T_{noise1} + \frac{T_{noise2}}{G_1} + \frac{T_{noise3}}{G_1 G_2} + ... + \frac{T_{noiseN}}{G_1 ... G_N}, \tag{2.2}$$

where T_{noisei} is the noise temperature and G_i is the available gain of each stage of the receiver. We see from this formula that the first stages before the cryogenic amplifier, which has a

gain $G >> 1$, have the most important effect on the total noise temperature of the receiver $T_{noisetot}$.

2.3.2.2 Measurement of the noise temperature

To measure the noise temperature of a receiver we usually use the Y-factor method, which is described a bit further in this section. We measure the output power of the receiver when the RF signal comes from loads at different temperatures (generally 77 K and 300 K). The output power is directly proportional to the noise temperature of the load plus the noise temperature of the receiver:

$$P = GkB(T_e + T_{load}), \tag{2.3}$$

where P is the measured power at the output of the receiver in Watts, k the Boltzmann's constant, B the bandwidth in Hertz and G the total amplification gain of the receiver. T_e and T_{load} are, respectively, the noise temperature of the receiver and the noise temperature of the observed RF load, in Kelvins. As described in the articles from Callen and Welton [15], Kerr et al. [16] and Kollberg and Yngvesson [17], the noise temperature of a black body is different from the its physical temperature, especially at frequencies above 1 THz. To accurately deduce the noise temperature T_{load} of a load at a physical temperature T, we use the Callen and Welton formula:

$$T_{load} = T\left[\frac{\frac{hf}{kT}}{\exp\left(\frac{hf}{kT}\right)-1}\right] + \frac{hf}{2k}, \tag{2.4}$$

where, h and k are the Planck and Boltzmann constants, and f the frequency at which we observe the load.

As example, we used realistic values of G, B and T_e and plotted the evolution of P as a function of T_{load} (figure 2.4). Two measurement points, $T_{load} = 77$ K and 300 K, allow to draw a line which intersects the abscissa axis at T=-1000 K. At $P = 0$, we easily deduce from equation 2.3 that $T_e = -T_{load}$. So, $T_e = 1000$ K corresponds to the noise temperature of the receiver in this example (with B=1 GHz and G=1E6).

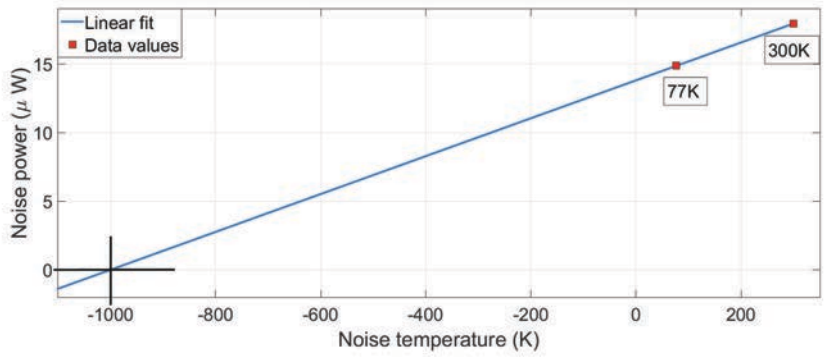

FIGURE 2.4: Measurement of the noise temperature of a heterodyne receiver

The Y factor method

To measure the noise temperature of a receiver, the Y factor method is usually used. The Y factor is calculated with the measured power at the output of the IF chain when the receiver sees a hot load and a cold load as RF signal. The ratio of the two powers defines the Y factor, as shown in the equation:

$$Y = \frac{P_{hot}}{P_{cold}} = \frac{T_{hot} + T_e}{T_{cold} + T_e}, \tag{2.5}$$

where P_{hot} and P_{cold} are the power values measured at the output of the IF chain when the receiver sees a hot load and a cold load, and T_e is the noise temperature of the receiver. T_{hot} and T_{cold} are the noise temperatures of the hot and cold loads, calculated with the Callen and Welton formula (equation 2.4). Then, we can deduce:

$$T_e = \frac{T_{hot} - Y\,T_{cold}}{Y - 1}. \tag{2.6}$$

We usually use liquid nitrogen to cool down a black body to 77 K to make the cold load, and we use a black body at ambient temperature as hot load. At THz frequencies, black bodies are usually made with absorbers, such as those from Eccosorb®. This method is fast and accurate (if the hot and cold temperatures are different enough (like 77 K and 300 K)), and it is not required to know the characteristics of the elements of the receiver. Therefore, it is the most used method to determine the noise temperature of heterodyne receivers.

2.4 Description of the different elements of a THz heterodyne receiver

2.4.1 The mixer

The mixer is a non-linear device which mixes the LO and RF signals to down-convert the observed RF signal to a lower frequency, called intermediate frequency (IF). An antenna, connected to the mixer, is generally used to receive the RF and LO signals. This antenna can have a large frequency bandwidth (like log-spiral antennas), or be frequency selective (like twin-slot antennas or horns). Several non-linear devices are used as mixers. The three most common mixers used in THz heterodyne receivers are Schottky diodes, SIS (Superconductor-Insulator-Superconductor) junctions, and HEBs (Hot Electron Bolometer). These different kinds of mixers are presented below with their characteristics, frequency ranges, and applications.

2.4.1.1 Down-conversion of the two RF side-bands

When the unbalanced standard mixer down-converts the RF spectrum, two side-bands, around the LO frequency, are down-converted. The lower side band (LSB), which is below the LO frequency, and the upper side band (USB), which is above the LO frequency, are both down-converted to the same IF band (figure 2.5).

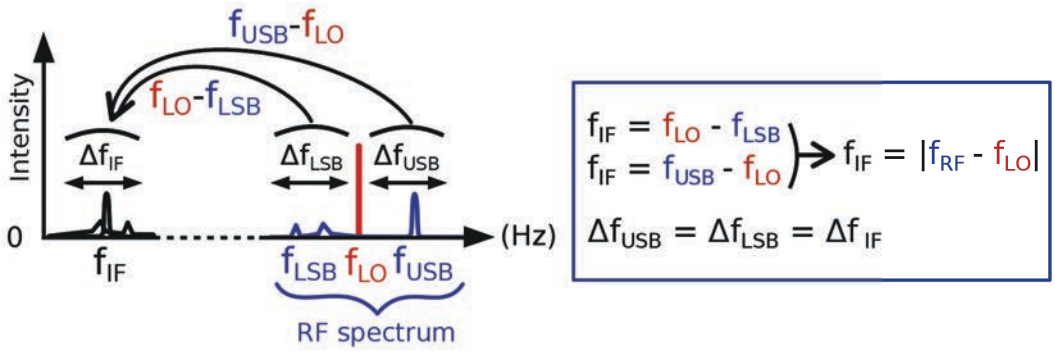

FIGURE 2.5: Down-conversion of the RF side bands

When the two side bands are down-converted, they are superimposed in the IF band. Receivers where both side bands are down-converted are called double-sideband (DSB) receivers.

2.4.1.2 The pumping of mixers

Mixers are non-linear devices, which means that the relation between their current and voltage is non-linear. However, the relation between their input and output power is usually linear (when the input power level is not too high). They must receive enough LO power to be in a very sensitive state and efficiently mix the LO and RF signals to generate the IF signal. When they are in this state, we say that they are pumped. A mixer is correctly pumped when the conversion of the RF electromagnetic signal into the IF electrical signal is the most efficient. The pumping level has an influence on the sensitivity of the mixer. Different mixers, such as Schottky diodes, SIS junctions or HEBs do not require the same amount of LO power to be pumped. Sometimes, it can be problematic to find a LO which generates enough power to correctly pump a mixer, especially at frequencies above 1 THz.

2.4.1.3 The Schottky diode mixer

Schottky diode mixers can be used at frequencies from several GHz up to several THz, and have the huge advantage of being operational at room temperature. However, their sensitivity can be improved by cooling them down, where they reach their optimal performance around 20 K (cf. Chattopadhyay et al. [18]). However, they need to be pumped with a high LO power, in the range of hundreds of µW to a few mW, which is their main limitation. Schottky mixers can also be used as harmonic mixers, which means that they can mix the RF signal with harmonic multiples of the LO signal. The frequency of the IF signal can correspond to $f_{IF} = |k.f_{LO} - l.f_{RF}|$, where $k, l \in \mathbb{N}$. Schottky diode mixers have a large bandwidth of several GHz. The latest results obtained with Schottky diode mixers designed and manufactured at LERMA showed a DSB noise temperature of 870 K at 557 GHz at ambient temperature. By cooling the mixer down to 134 K, this noise temperature was reduced by approximately 200 K (cf. Maestrini et al. [19] and Treuttel et al. [20]). At frequencies around 1 THz, harmonic Schottky diode mixers currently have a DSB noise temperature of 4000 K, at room temperature, as shown by the article from Thomas et al. [21].

A Schottky mixer has been used in the first heterodyne receiver above 1 THz (cf. Röser [3]). However, the next heterodyne receivers used cryogenic mixers, which have a lower noise temperature and require less LO power than Schottky mixers. Today, Schottky diode mixers are mainly used to analyze planets' atmospheres, where we do not need the high

sensitivity of SIS or HEB mixers. For such missions, their higher operating temperature is a big advantage because they do not require to be cooled down by cryogenic liquids, which evaporate with time. Pictures of a Schottky mixer circuit, and of a pair of Schottky diodes are shown in figure 2.6.

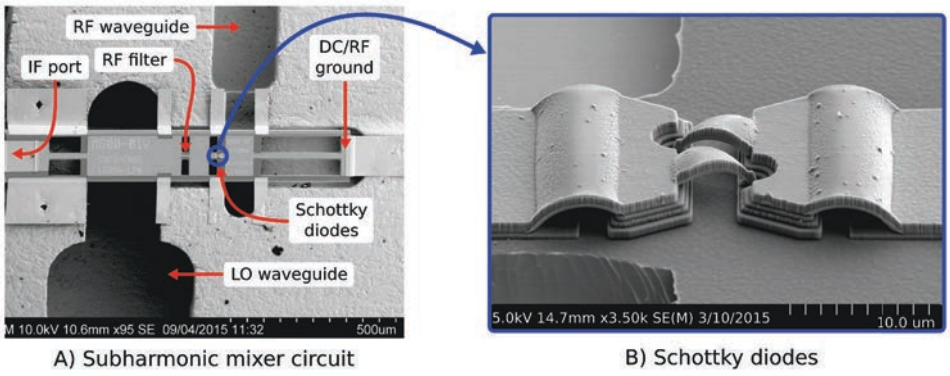

FIGURE 2.6: SEM picture of a LERMA-LPN 600 GHz subharmonic mixer (A), and of an anti-parallel pair of Schottky diodes (B)
(Credits: Alain Maestrini)

2.4.1.4 The SIS mixer

Superconductor-Insulator-Superconductor (SIS) junctions are very sensitive mixers at sub-millimeter wavelengths. However, as most SIS mixers use niobium or niobium nitride as superconducting material, they only work up to approximately 1.3 THz, twice the voltage gap of niobium. Practically, they are used as mixers for frequencies below 1 THz, where they are the most sensitive mixers. They have an excellent noise temperature (ie. 30 K at 100 GHz and 85 K at 500 GHz, cf. Carter et al. [22] and Chattopadhyay et al. [18]), and must be cooled down to approximately 4 K with liquid helium. Their bandwidth can be greater than 4 GHz and they need to be used with an LO which emits around 40 μW to 100 μW. As they offer the best sensitivity below 1 THz, they are used in nearly all sub-millimeter telescopes, such as ALMA [23] and NOEMA [24].

2.4.1.5 The HEB mixer

Hot Electron Bolometer (HEB) mixers are currently the most sensitive mixers for frequencies above 1.3 THz. They need to be cooled down to approximately 4 K and can reach a

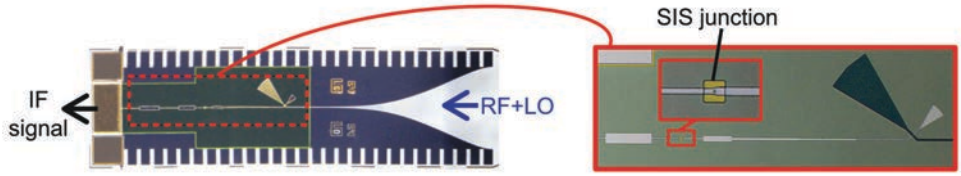

FIGURE 2.7: Picture of a SIS mixer
(Credits: Faouzi Boussaha)

bandwidth of 3 or 4 GHz. They have a noise temperature better than Schottky mixers (approximately 1200 K between 1.4 THz and 1.9 THz for HIFI [8]). They only require 1 or 2 μW of LO power to be pumped, a lot less than Schottky and SIS mixers. It enables them to be used with high frequency LO which only emit a few μW. They are a good alternative to Schottky diode mixers for high THz frequencies, when a high sensitivity is needed, or when there is not a lot of LO power available. All actual heterodyne receivers for astronomy above 1 THz use HEB mixers. HEB mixers have been used in HIFI [8] on the Herschel satellite, and are used on GREAT [10] and upGREAT [11], which operate from SOFIA airplane.

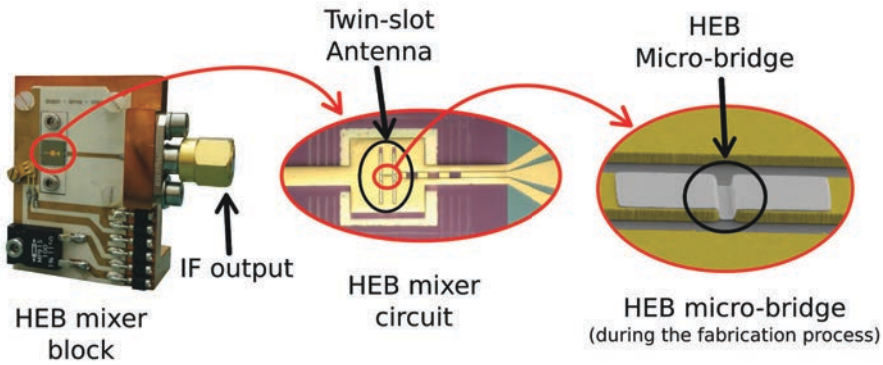

FIGURE 2.8: Pictures of a HEB
(Credits: Gregory Gay)

2.4.2 The local oscillator

The local oscillator (LO) is one of the main components of a heterodyne receiver. It has to generate a very stable quasi-monochromatic signal to pump the mixer and to be mixed with the RF signal to produce the IF signal. Moreover, to pump the mixer, it has to emit enough power, which is sometimes difficult above 1 THz. There are several kinds of LO, with different characteristics. The most widely used is the frequency multiplier chain, and the

most promising at high THz frequencies is the quantum laser cascade. These two different LOs are described below.

2.4.2.1 The frequency multiplier chain

Frequency multiplier chains are the most widely used LOs in THz heterodyne receivers (figure 2.9 shows a frequency multiplier chain from Virginia Diodes Inc. (VDI)). An input low frequency signal (a few tens of GHz) is multiplied and amplified by the multipliers and amplifiers of the chain to generate the final LO signal. The input signal can be generated by a Gunn diode or a frequency synthesizer. However, each multiplier of the chain loses some power. As a result, at frequencies higher than 2 THz, multiplier chain LOs do not generate more than a few μW.

FIGURE 2.9: Example of a frequency multiplier chain LO from VDI
(Picture from Hesler et al. [25])

The article from Hesler et al. [25] describes the latest performances of frequency multiplier chain LOs, up to 3 THz (figure 2.11 shows the output power achieved with frequency multiplier chains and QCLs). Frequency multiplier chains can operate at room temperature and are usually very stable and monochromatic. As multiplier chains use waveguides, the output is usually radiated by a horn, which gives a linearly polarized Gaussian beam. Moreover, it is possible to tune the output frequency of multiplier chains by approximately 10 % to 20 %, allowing the observation of several frequency lines with the same heterodyne receiver. So, frequency multiplier chains are very reliable, flexible and are used in most heterodyne receivers for frequencies below 3 THz.

2.4.2.2 The quantum cascade laser

Quantum Cascade Lasers (QCLs) are mostly aimed to replace frequency multiplier chains as LOs at frequencies higher than 3 THz. Figure 2.10 shows a zoomed picture of a QCL made by the MPQ (Materials and Quantum Phenomena) laboratory.

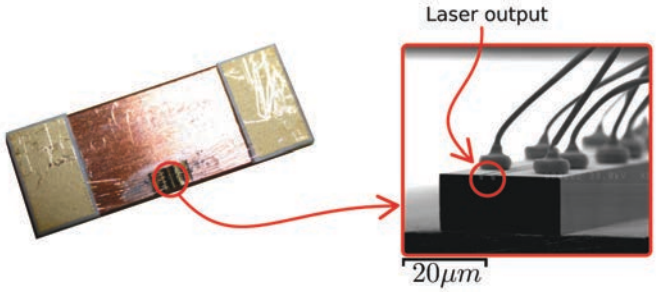

FIGURE 2.10: Picture of a QCL
(Courtesy of Carlo Sirtori, MPQ laboratory)

THz QCLs need to operate at cryogenic temperatures, usually between 10 K and 70 K (cf. Ren et al. [26]) which is less convenient than frequency multiplier chains. Moreover, QCL are not very frequency stable, are difficult to phase lock and are usually not continuously tunable (cf. Ren et al. [27]). As QCLs' beam is not very Gaussian, the coupling with the mixer is not perfect and has losses. Figure 2.11 shows the output power of QCL and frequency multiplier chains as a function of frequency.

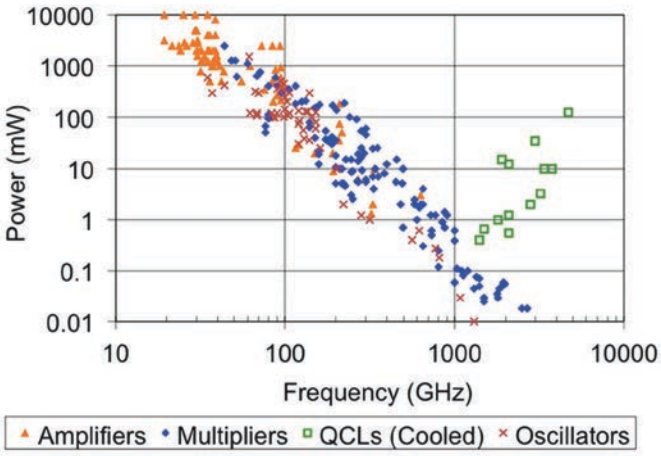

FIGURE 2.11: Output power of different kinds of LOs as a function of frequency
(Picture from Hesler et al. [25])

Today, QCLs are only used as LOs for frequencies above 2.5 THz, where frequency multiplier chains do not emit enough power to pump the mixer. However, as the technology of QCLs evolve, it should be possible, in a near future, to have more stable QCLs with an operating temperature above 77 K, which would make them more convenient to use as LOs.

2.4.3 The diplexer

Most SIS and HEB mixers have only one input antenna for both LO and RF signals In this case, a diplexer is used to superimpose the RF and LO signals before they reach the mixer. This element is very important because its losses have a direct impact on the sensitivity of the whole receiver. It must efficiently superimpose the two signals and lose as little RF power as possible, while the LO power transmitted to the mixer must still be high enough to pump it. Two major diplexers are used in THz heterodyne receivers, the beam splitter and the Martin Puplett interferometer (MPI). The beam splitter is more convenient to use, but it loses a lot of LO power, while the MPI is more complicated to align but has less LO losses. These two diplexers are presented below, and the MPI is described in detail in Chapter 4, as it is an important part of our 2.6 THz heterodyne receiver.

2.4.3.1 The beam splitter

The most commonly used diplexer in heterodyne receivers is a beam splitter. It can split an incoming beam into a reflected beam and a transmitted beam. In the case of a heterodyne receiver, it receives both LO and RF beams, and reflects the LO beam while it transmits the RF beam. Beam splitters for THz frequencies are often made of Mylar. Depending on the thickness of the Mylar, the power reflection and transmission coefficients vary with frequency. Usually, the beam splitter is chosen to have a power reflection of the LO beam around 5 % or 10 %, while the RF beam is transmitted at 90 % or 95 %. This method is very convenient because the beam splitter is easy to align, and transmits most of the RF signal, which is what we are interested in for astronomical observations. However, at high frequencies, multiplier chain LOs do not emit a lot of power and it is difficult to pump the mixer. So, losing 90 % or 95 % of the LO power becomes a problem. Other more complex diplexers with a better efficiency exist, like the Martin Puplett interferometer (MPI), presented below.

2.4.3.2 The Martin Puplett Interferometer

The Martin Puplett interferometer (MPI) is a diplexer which can superimpose the LO and RF signals with very little losses, for both signals. The functioning of the MPI is extensively described in chapter 4, because it is an important part of our 2.6 THz heterodyne receiver. The MPI is composed of two wire grids, G1 and G2, and two roof-top mirrors T1 and T2, as shown in figure 2.12. An ellipsoidal mirror (MLO) is added to focus the LO signal.

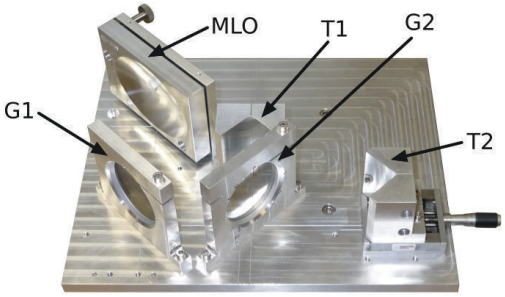

FIGURE 2.12: Picture of a MPI designed at the Observatory of Paris

The MPI has already been used as diplexer in several major heterodyne receivers, such as GREAT [10] and CONDOR [5]. However, as it is a lot more difficult to align than a simple beam splitter, it is only used in THz heterodyne receivers for high frequencies, where there is little LO power available.

2.4.4 The IF chain and the spectrometer

At the output of the mixer, the intermediate frequency (IF) signal needs to be amplified and filtered before being processed by a spectrometer. The first amplifier, just after the mixer, is usually a low noise cryogenic amplifier because it is important to add as little noise to the IF signal as possible. Then, ambient temperature low noise amplifiers (LNA) and a bandpass filter are often used to amplify further the IF signal and filter it. Finally, a spectrometer is used to analyze the down-converted spectrum of the IF signal. Because of recent technological developments, digital Fourier transform spectrometers (DFTS) have become the standard spectrometers for heterodyne receivers. A DFTS uses an analog to digital converter (ADC) card to digitize the input signal, and a FPGA to perform a fast Fourier transform (FFT) of the data, in real time. The spectral data can be directly transmitted to a computer. With the increasing speed of the FPGAs and ADC cards, DFTS are improving fast and some 5 GHz

bandwidth DFTS are currently available (ie. the second generation of DFTS from Omnisys company).

FIGURE 2.13: Picture of a DFTS, from Radiometer Physics company

2.5 Our 2.6 THz heterodyne receiver

2.5.1 Description of our 2.6 THz heterodyne receiver

During this PhD, I built, tested and improved a 2.6 THz heterodyne prototype receiver (figure 2.14), whose elements are described below.

- The LO: I use a 2.6 THz frequency multiplier chain from VDI (Virginia diodes Inc.) which emits a maximum of 2 μW.
- The mixer: For our tests, we used a HEB using a log spiral antenna which was designed and produced at LERMA and LPN laboratories and works well for frequencies up to several THz (cf. Delorme et al. [28] and Lefèvre et al. [29]). It uses a NbN (niobium nitride) bridge on a silicon substrate and is phonon cooled. However, the final mixer will be a HEB with a twin-slot antenna optimized for 2.5 to 2.7 THz. In both cases, we add a silicon lens in front of the HEB to focus the signal.
- The mixer bias supply: The bias supply for the HEB has been manufactured at LERMA, according to the plans elaborated at SRON to build the bias supply for the HIFI instrument of the Herschel satellite.
- The diplexer: A Martin Puplett interferometer (MPI) is used as diplexer. I have specifically designed it for our 2.6 THz receiver and it is extensively described in chapter 4.

- The intermediate frequency (IF) chain: The IF chain is composed of a cryogenic amplifier, two warm amplifiers a bandpass filter and some attenuators to avoid saturating the last amplifier and reduce possible standing waves. The low noise cryogenic amplifier was bought from Caltech university. Between 300 MHz and 4 GHz, and at a temperature of 21K, it has a gain of 35 dB to 43 dB and a noise temperature below 4 K. The warm amplifiers were bought from Miteq (model: AFS3-00100600 13-10P-4) and have a gain of 33dB to 33.5dB in our frequency range at ambient temperature. The [0.5 - 1.5] GHz bandpass filter selects the range where our receiver is the most sensitive.

- The spectrometer: I use a DFTS bought from RPG which has 8192 channels and a bandwidth of 1.5 GHz.

- The cryostat: I use a wet cryostat filled with liquid Helium.

- Windows and IR filters: I use a 1mm thick HDPE (High density polyethylene) window for the cryostat followed by two sheets of Zitex® G104 as infra-red filter (The transmission properties of Zitex® were studied by Benford et al. [30]).

This configuration has been used for most of the experiments described in this thesis, with two occasional changes: The 2.6 THz LO has been sometimes replaced by a 1.4 THz or a 600 GHz LO, and a beam splitter diplexer was used with these lower frequency LO.

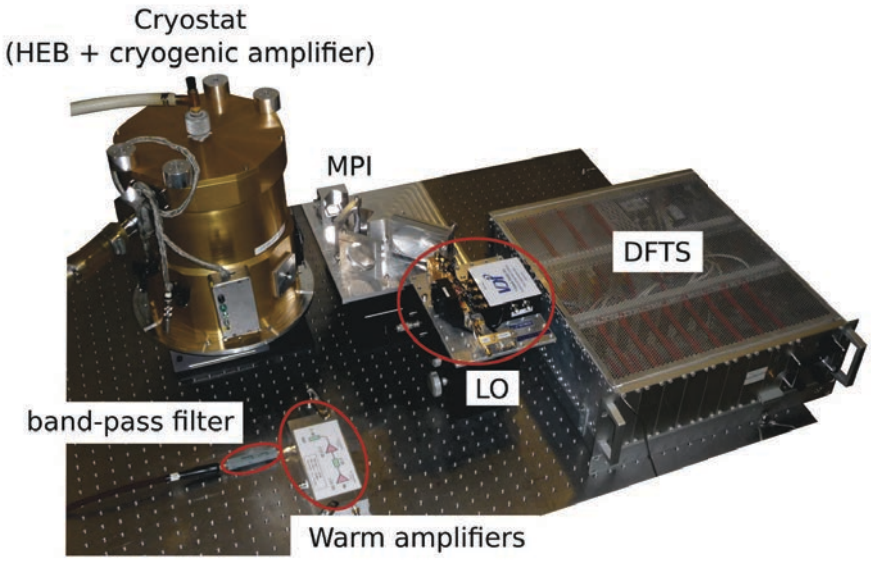

FIGURE 2.14: Picture of our heterodyne receiver

2.5.2 Main aspects of this PhD

During this PhD, I built this prototype THz heterodyne receiver and I focused on 3 crucial and very challenging aspects.

- **The stability of the receiver**: As this parameter is one of the most important characteristics of heterodyne receivers, I developed a specific program and made multiple experiments in order to accurately characterize the stability of the different parts of our receiver. This study will enable me to correct and replace the least stable elements and greatly increase the stability of our heterodyne receiver (cf. chapter 3).

- **The LO-RF coupling**: To be able to superimpose the LO and RF signals with very little losses, I designed, built and tested a MPI diplexer optimized for our 2.6 THz LO. In chapter 4, I describe the design and tests of our MPI and the characterization of all its components.

- **The beam splitting**: Usually, heterodyne receivers have a single pixel and only measure the spectrum in one region of the sky. To prepare for the future of powerful multi-pixel receivers, I dedicated the last part of my PhD to this challenging aspect. A multi-pixel receiver requires the LO signal to be split into several beams, in order to feed several mixers. To achieve this goal, I designed, simulated and built two phase grating prototypes to split the LO signal into 4 beams at 600 GHz (cf. chapter 5). This is a major step toward the achievement of a fully operational multi-pixel 2.6 THz heterodyne receiver.

Chapter 3

Stability of the heterodyne receiver

3.1 Introduction

3.1.1 Motivation

Astronomical receivers are characterized by their observing frequency range, their bandwidth, their spectral resolution, etc. Their performance is described by their sensitivity, but their stability is not always mentioned even though it is a very important characteristic. A stable receiver can integrate observation data over a long time while the noise contained in the observations is reduced. An unstable receiver, in contrast, often needs to be re-calibrated. The stability, that can be expressed in terms of Allan minimum time, as we shall see below, is therefore a very important parameter. The stability determines the optimum integration time for a particular instrument.

In this chapter, I will explain why it is important to know the optimal integration time of a receiver for radio-astronomical observations. Then, we will look at the relation between the noise and the optimal integration time, and how we can determinate both by using the Allan variance. The second section of the chapter describes the Allan variance theory and presents the two kinds of Allan variances used in this thesis: the total power Allan variance and the spectral Allan variance. Then, in the third section, I measure the Allan variance of our heterodyne receiver to deduce its optimal integration time.

3.1.2 Influence of the noise on the optimal integration time

3.1.2.1 The radiometer formula

All measurements have random noise (or white noise) which is usually produced by the measuring instrument and by the measured phenomenon. By repeating the same measurement and averaging the results, the random noise can be reduced. The radiometer formula 3.1 describes how the white noise of a measurement decreases with the integration time and the bandwidth of the measurement.

$$\sigma \propto \frac{1}{\sqrt{B \times T}}, \tag{3.1}$$

where σ, B and T are, respectively, the standard deviation (or rms noise), the bandwidth and the integration time of the measurement. However, this formula is only valid if the instrument only produces white noise.

3.1.2.2 Different kinds of instrumental noise

The noise level of a data set is described by its deviation (σ) or its variance (σ^2). The bigger the deviation (or the variance), the higher the noise level. The radiometer formula (equation. 3.1) states that when the integration time increases, the standard deviation of the data decreases, so does the white noise level. Most instruments do not only produce white noise, but also low frequency noise. The power spectrum $S(f)$ of a signal is proportional to the squared Fourier transform of the measured signal along time:

$$S(f) \propto |\mathscr{F}[x(t)]|^2 \tag{3.2}$$

Where $\mathscr{F}$ is the Fourier transform, x(t) the data values along time, and f the frequency. The noise generated by an instrument can be divided into three classes, the white noise, the Flicker noise and the drift noise. They are characterized by their power spectrum, $S(f)$, which is proportional to $f^{-\alpha}$, as ilustrated by figure 3.2. Where $\alpha \in [0\ ,\ 3]$. These noises are represented in figure 3.1 and described below:

- The white (or random) noise: $S(f) = f^0$. It has the same amplitude at all frequencies and is random. It can be reduced by increasing the integration time of the receiver, as described by the radiometer formula (equation. 3.1).
- The Flicker noise: $S(f) = f^{-1}$. Its amplitude decreases with frequency. It is usually produced by electronic devices and it is independent of the integration time (it does not increase nor decrease).
- The drift noise: $S(f) = f^{-\alpha}$, where $2 \leq \alpha < 3$. Its amplitude is high at low frequencies and quickly decreases at higher frequencies. It is produced by slow variations (ie. mechanical, thermal, gain fluctuations etc.), and it increases with integration time.

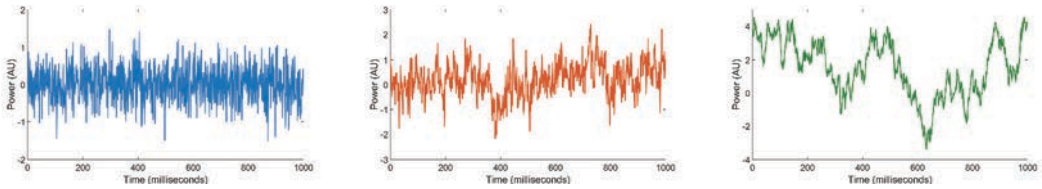

(A) White noise (B) Flicker noise (C) Drift noise

FIGURE 3.1: Examples of white, Flicker and drift noises along time

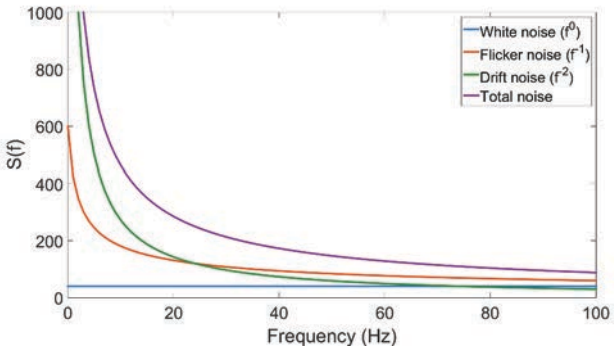

FIGURE 3.2: Power spectrum $S(f)$ of the different noise signals and of their sum

3.1.2.3 Summary

Generally, increasing the integration time of the data samples reduces the white noise but increases the drift noise, while it does not affect the Flicker noise level. The optimal integration time corresponds to a trade off between drift and white noises. Evaluating the total noise level and the contribution from each of these three noises over time can enable us to

determine the optimal integration time. To achieve this goal, the Allan variance is a very useful parameter.

3.2 The Allan variance

3.2.1 Background and theory

The Allan variance was first developed by D. W. Allan [31] in 1966. During the following years, it has become a widely used tool in radio-astronomy to evaluate the stability of instruments. The Allan variance (σ_A^2) is directly related to the total noise level present in the data set measured by the instrument. So, when plotting the Allan variance as a function of the integration time, the lowest noise level is reached for the integration time corresponding to the smallest value of Allan variance. In figure 3.3, we plotted the evolution of the Allan variance depending on the integration time of the three noises (white, Flicker and drift) listed in the previous section (figure 3.1).

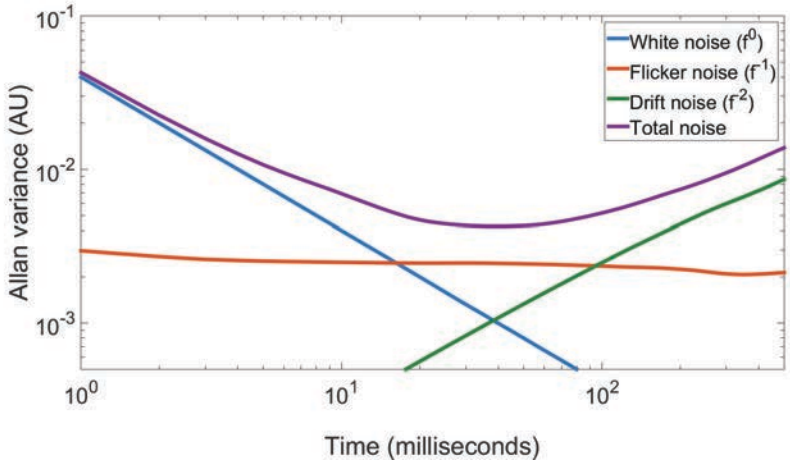

FIGURE 3.3: Allan variance of the 3 noises signals (logarithmic scale)

When using a log-log plot, the Allan variance of each type of noise has a specific slope. The coefficient of this slope, β, is equal to $\alpha - 1$. Where α is the exponent of the power spectrum of the considered noise. The values of α corresponding to the white, Flicker and drift noises are, respectively, 0, 1 and $2 \leq \alpha < 3$. That is why the Allan variance curves of these noises have the following slope coefficients: $\beta = -1$, $\beta = 0$ and $1 \leq \beta < 2$. In the case of white noise alone, the Allan variance (σ_A^2) is proportional to the square of the deviation given by the radiometer formula (equation 3.1).

The Allan variance of the total signal, composed of the three noises, is the purple curve (figure 3.3). For short integration times, the Allan variance mostly follows the white noise curve, because it is the dominant noise. At longer integration times, the white noise becomes negligible compared to the Flicker and drift noises, and the Allan variance increases due to the effect of the drift noise. The lowest noise level is obtained for an integration time corresponding to the minimum of the curve (where the Allan variance is the lowest), around 30 ms in our example. We call this optimal integration time or Allan time (T_A). However, when the minimum is not clearly visible on the curve, a good estimation of the Allan time is when the Allan variance deviates from the radiometric line (White noise Allan variance) by a factor $\sqrt{2}$. Curves without distinct minimum can occur when the Flicker noise is important and the flat zone around the minimum of the Allan variance curve is quite large. The Allan variance is very useful to analyze the stability of an instrument because it enables us to clearly identify the 3 noises, and to exactly determine the optimum integration time.

3.2.2 Allan variance theory

The Allan variance theory is well described by Allan [31], Barnes [32], Schieder and Kramer [33] and Kooi [34]. The Allan variance of an instrument is defined by the Allan variance of data samples taken by this instrument when measuring a constant input signal (a load at constant temperature for example).

We consider a continuous data set composed of N contiguous data samples x_i ($i \in [1\ ,\ N]$)), where the pauses between the measurements are negligible. The integration time of each data sample is τ. We look at subsets of K samples, each with an integration time of $T = K\tau$, where K is the number of x_i samples considered. The N samples are split into M adjacent groups of K samples each ($M = \lfloor N/K \rfloor$, where $\lfloor\ \rfloor$ represents the $floor$ function). Each group is averaged and the calculated mean ($X_n(K)$) corresponds to the data measured by the instrument during an integration time $T = K\tau$.

$$X_n(K) = \frac{1}{K}\sum_{i=1}^{K} x_{(nK+i)}. \tag{3.3}$$

And finally, the Allan variance (σ_A^2) is calculated as:

$$\sigma_A^2(T) = \frac{\langle (X_{n+1}(K) - X_n(K))^2 \rangle}{2}, \tag{3.4}$$

$$\sigma_A^2(T) = \frac{1}{2(M-1)} \sum_{n=1}^{M-1} (X_{n+1}(K) - X_n(K))^2 . \tag{3.5}$$

To plot the Allan variance as a function of the integration time, we need to calculate σ_A^2 for different values of K (the number of samples averaged in one group). We iterate K from 1 to N/2 to calculate the Allan variance for integration times from τ to $N\tau/2$. The successive Allan variance values calculated for different integration times ($T = K\tau$) constitute the Allan variance plot, as shown in figure 3.4

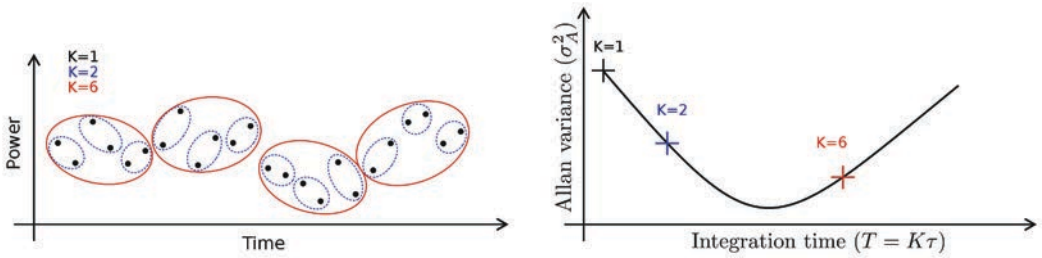

FIGURE 3.4: Schematic showing how the Allan variance is calculated by considering different groups of data samples. The Allan variance plot uses a log-log scale

3.2.2.1 Bandwidth influence on the Allan variance

The Allan variance also depends on the frequency bandwidth B of the measurement. As the bandwidth is increased (by averaging the signal of several channels of a spectrometer for example), the white noise is reduced. As a result, the Allan time (T_A) becomes smaller because the intersection between the white noise and drift noise curves occurs at a shorter integration time. This relation is expressed by the following formula:

$$\frac{T_A'}{T_A} = \left(\frac{B}{B'}\right)^{\frac{1}{\beta+1}}, \tag{3.6}$$

where β is the slope of the drift noise on the Allan variance plot, B and B' are two different bandwidths used to measure the same device, T_A and T_A' are the two corresponding Allan times.

3.2.3 Total power and spectral Allan variance

Two kinds of stabilities have been investigated with the Allan variance, the total power and the spectral ones. The total power Allan variance estimates the noise level of a power measurement over the instrument's bandwidth. The spectral Allan variance considers the variations between different frequency channels. It corresponds to the Allan variance of the difference between two frequency channels separated by a spectral distance B. As our heterodyne receiver is designed to observe spectral lines, we are mostly interested in its spectral stability.

3.2.3.1 Total power Allan variance

The total power Allan variance describes the noise of a total power measurement over a given frequency range. For astronomical observations, this stability is mostly needed when we observe *continuum* emission, such as black body radiation, which emits over a frequency range larger than the instrument's bandwidth. Our heterodyne receiver will be mostly used to observe spectral lines, so the spectral Allan variance is more important. However, we need to calibrate our receiver with a calibration load. So, we must be sure that its total power Allan time is long enough to have good enough gain stability between two calibrations.

3.2.3.2 Spectral Allan variance

The spectral Allan variance evaluates the variation of the difference between distinct frequency channels. It tells us if the power of each frequency channels is stable compared to that of another frequency channel (ie. it measures the deformation of the spectrum along time). To measure the spectral Allan variance we need a spectrometer. Then, the Allan variance calculation uses the power difference between two channels. If the power of all channels varies by the same amount, it affects the total power stability but not the spectral stability. However, if the power measured by the channels varies independently of its neighbours, the spectral stability will be affected. The spectral stability is important for spectral line measurements. When we observe a spectral line, we need to compare the power of this spectral line to the adjacent frequency channels which do not receive any signal. The power difference between the channels which receive the signal of interest and the adjacent channels which receive a background signal determines the power amplitude of the

observed frequency line. So, we need a good spectral stability to integrate the spectrum and to determine the difference between these channels accurately (with little noise).

3.2.4 The calculation algorithm

To calculate the Allan variance, different software exist, such as Alavar, which is a freeware, created by Alaa Makdissi [35]. However, for the data produced by our DFTS, I needed to calculate thousands of Allan variances (one for each frequency channel). This is not possible with Alavar, so I wrote a Matlab program that uses our DFTS data as input, and calculates its total power and spectral Allan variances. This Matlab program is based on the Allan variance equations presented in section 3.2.2. Moreover, it takes advantage of Matlab matrix manipulation and parallel computing to calculate many variances in a reasonable amount of time. To check its validity, I compared the Allan variance curve calculated by Alavar with the curve calculated by my program, for identical sets of data. Two examples are shown in figure 3.5.

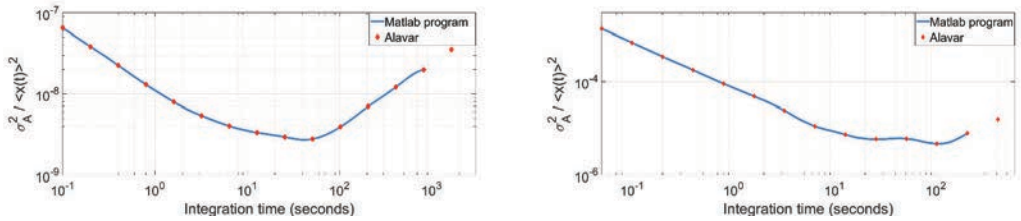

(A) Allan variance of signal 1 (B) Allan variance of signal 2

FIGURE 3.5: Allan variance of two signals, calculated with Alavar and with my Matlab program

In both programs, the calculated Allan variance is the normalized Allan variance:

$$\frac{\sigma_A^2}{< x(t) >^2}. \tag{3.7}$$

This normalization allows us to only consider the relative variations of the signal and not its absolute level, when calculating the Allan variance. Therefore, we can compare the noise level of different signals by comparing their normalized Allan variance plots. We see that the Allan variance calculated by my program is exactly the same as the Allan variance given by Alavar. We can conclude that my Allan variance program is reliable to calculate the Allan variance of our measurements.

3.3 Stability of our heterodyne receiver

Our heterodyne receiver is composed of a local oscillator (LO), a coupling element (beam splitter or Martin Puplett interferometer), a Hot Electron Bolometer (HEB) mixer, an intermediate frequency (IF) chain and a digital Fourier transform spectrometer (DFTS) (figure 3.6). Our heterodyne receiver and its components are described in detail in section 2.5.

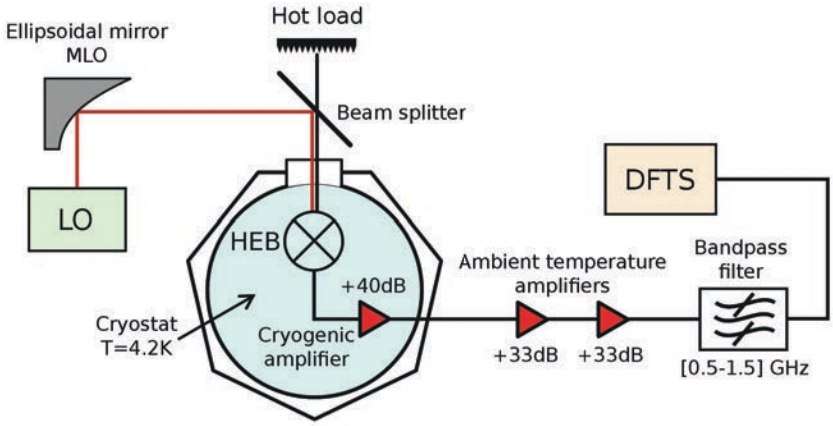

FIGURE 3.6: Schematic of our heterodyne receiver set-up

I added the components of our receiver successively and measured the stability of the set-up at different stages. It enabled me to measure the stability of different groups of elements and identify the least stable ones. It can allow us to increase the stability of the whole receiver by improving or changing these elements. I also measured the Allan variance (total and spectral) of the whole receiver to know its optimal integration time.

3.3.1 Warm intermediate frequency chain and DFTS

The warm intermediate frequency (IF) chain is composed of two warm amplifiers operating at ambient temperature and a bandpass filter (figure 3.6). Some attenuators (not shown on the figure) were put between the amplifiers to avoid standing waves. The warm amplifiers have a gain of 33 dB to 33.5 dB. Some attenuators were put before and between the amplifiers in order to avoid saturating the last amplifier. The IF signal generated by the heterodyne receiver was read by a digital Fourier transform spectrometer (DFTS) and a power meter. I first measured the temperature influence on the gain of the warm amplifiers. Then, I measured the total power and spectral Allan variances of the set-up composed of the warm IF chain plus the DFTS and the power meter.

3.3.1.1 Temperature influence on the gain of the warm amplifiers

I used a commercial noise source with an ENR (Excess Noise Ratio) of approximately 15 dB to generate the input signal. It was amplified by the two warm amplifiers and I measured the output power with a power meter, through a 0.5 GHz - 1.5 GHz bandpass filter. It enabled me to measure the dependence of the amplifiers' gain on temperature, between 0.5 GHz and 1.5 GHz, as shown in figure 3.7.

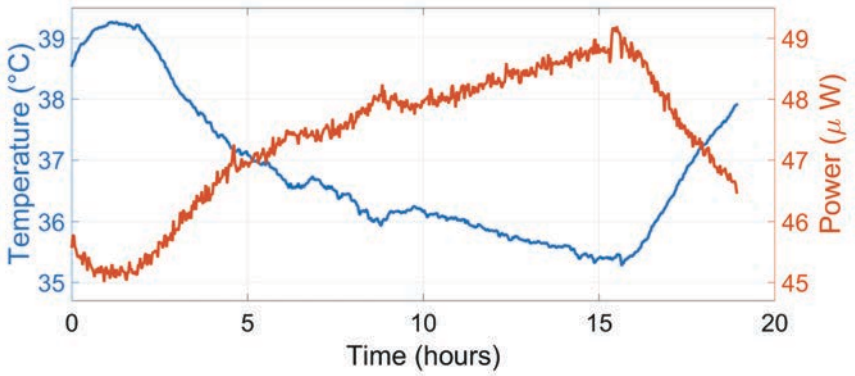

FIGURE 3.7: Evolution of the gain of the 2 amplifiers as a function of temperature

We clearly see that the temperature has a huge influence on the amplifiers' gain. The gain decreases by 0.045 dB (or 1.0 %) per amplifier and per degree. I tested separately the noise source and the power meter to make sure they were not the cause of the changes. This result tells us that we need to make sure that the temperature of the amplifiers is very stable in order to have a good total power stability at the output of the IF chain.

3.3.1.2 Stability of the warm amplifiers

I connected a 50 Ω load at the input of the warm amplifiers and measured the output power, after the bandpass filter, with the DFTS and a power meter (figure 3.8).

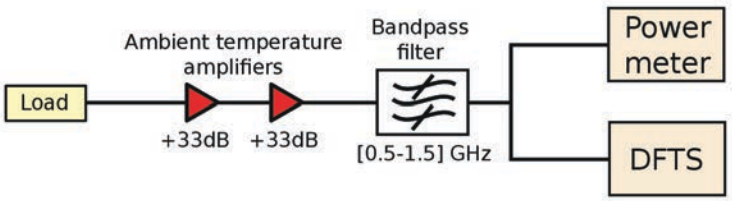

FIGURE 3.8: Set up of the experiment to measure the stability of the warm IF chain

Total power Allan variance

I compared the power measured by the power meter and the sum of the powers measured by all the channels of the DFTS, from 0.5 GHz to 1.5 GHz. On figure 3.9, we see the total power measured by the two devices as a function of time. The maximum power change measured by the power meter over the 6h20 min of the experiment is 0.9 μW. According to the previous section, this gain variation of 1.2 % for the two amplifiers, corresponds to a temperature variation of 0.6 °C. This temperature shift is very small but still clearly visible on the plot. Morevover, it is consistent with the evolution of the outside temperature. The measurement started in the morning, the temperature had reached its minimum and started to increase (so the gain of the amplifiers started to decrease).

The power measurements of the DFTS and the power meter are very similar, so, we can consider that both devices are reliable and perform accurate measurements.

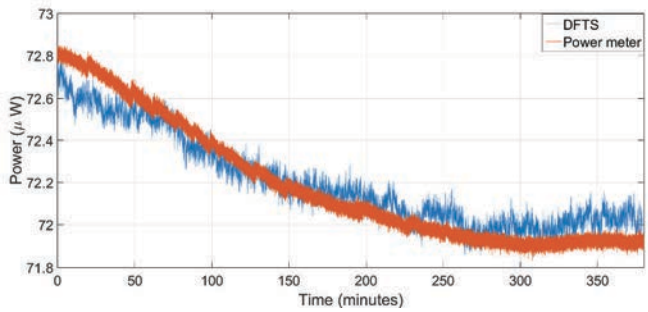

FIGURE 3.9: Total power read by the DFTS and the power meter along time

To know the stability of the warm IF chain, I calculated the Allan variance of the signals measured by the power meter and the DFTS. In the case of the power meter, I calculated the Allan variance of the power signal measured after the [0.5 1.5] GHz bandpass filter. In the case of the DFTS, I calculated the Allan variances of the power signals measured by all the frequency channels, which are 0.18 MHz wide. Then, I grouped and averaged these Allan variances in order to get nine curves representing the means of the Allan variances of all the frequency channels belonging to nine 100 MHz wide intervals, from 495 MHz to 1394 MHz. We see in figure 3.10 the total power Allan variance measured by the power meter (fig. 3.10a) and the total power Allan variances measured by the DFTS and averaged (fig. 3.10b). The mean Allan time for the spectral channels is close to 270 s, while the Allan time measured by the power meter for the complete bandwidth (from 0.5 to 1.5 GHz) is 10 s.

The different Allan times of the spectral channels and the power meter are due to the different bandwidth considered for each instrument (0.18 MHz for each DFTS channel against 1 GHz for the total bandwidth seen by the power meter). According to the equation 3.6, a smaller bandwidth results in a greater Allan time, for a given instrument or set-up.

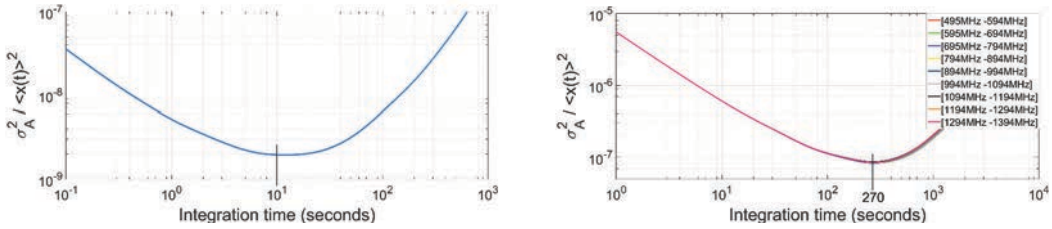

(A) Total power Allan variance measured by the power meter

(B) Total power Allan variance of each channel of the DFTS

FIGURE 3.10: Total power Allan variance measured by the power meter and the DFTS

In their article, Berg et al. [36] describe some interesting total power Allan variance measurements of HEB mixers between 0.6 THz and 1.9 THz. The Allan times they measured for different HEBs vary from 100 ms to 3 s, for a bandwidth of 30 MHz. By using equation 3.6 we calculate that, for our DFTS' channels of 0.18 MHz, it corresponds to an Allan time of 8 to 250 seconds. As the total power Allan time of the warm IF chain and the DFTS is greater than 250 seconds (for 0.18 MHz wide channels), we conclude that the warm IF chain and the DFTS should not limit the stability of our receiver.

Spectral Allan variance

The spectral Allan variance was calculated for all the channels of the DFTS comprised between 0.5 and 1.5 GHz. I performed the subtraction of two channels separated by a spectral distance $\Delta\nu$ and calculated the Allan variance of this difference. Then, for each value of $\Delta\nu$ I calculated the mean of the Allan variances of all the channel subtractions.

Figure 3.11 shows the spectral Allan variance of the warm IF chain and the DFTS. The spectral Allan variance was calculated for different spectral distances, from 1 MHz to 500 MHz. For spectral distances smaller than 50 MHz, the Allan time is greater than 4000 seconds. But for $\Delta\nu = 100$ MHz and $\Delta\nu = 500$ MHz, the Allan time is approximatively 4000 seconds. Frequency channels separated by a larger spectral distance evolve more differently than channels near to each other. That is why the Allan time is shorter for a spectral distance of 500 MHz than for smaller values of $\Delta\nu$. These results are consistent with the Allan

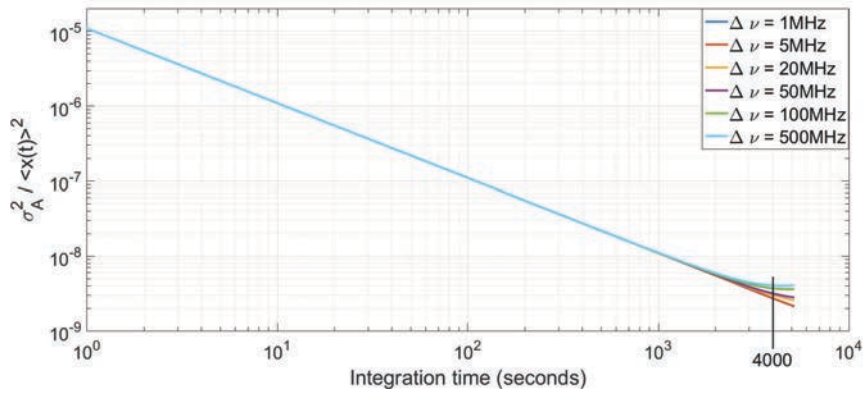

FIGURE 3.11: Spectral Allan variance for different spectral distances

time given by RPG, the company which sold us the DFTS. They measured an Allan time of 3000 s for a spectral distance $\Delta\nu = 1$ GHz, between 1 MHz wide channels.

GREAT [10] is a heterodyne instrument of the SOFIA telescope. GREAT also uses a HEB mixer to observe between 1200 GHz and 1900 GHz, and the spectral Allan time of the whole instrument is between 100 and 200 seconds. To obtain these results, they considered 0.85 MHz wide frequency channels separated by 750 MHz. Our heterodyne receiver is similar to GREAT and I measured a spectral Allan time of 4000 s, for slightly smaller frequency channels. Therefore, we can expect that the spectral Allan time of the receiver will not be limited by the warm IF chain and the DFTS.

3.3.1.3 Conclusion

I measured the total power and spectral Allan variances of a set-up composed of the warm IF chain plus the DFTS and the power meter (figure 3.8). I noticed that the temperature variations were influencing a lot the warm amplifiers' gain, and could reduce the stability of the set-up. The power meter measured a total power Allan time of 10 seconds for a bandwidth of 1 GHz, while the DFTS measured an average total power Allan time of 270 seconds for each of its 0.18 MHz wide frequency channels. I also measured the spectral Allan variance of the set-up. For a spectral distance between two frequency channels of 1 MHz to 500 MHz, the spectral Allan time was equal to 4000 seconds or more.

According to the total power Allan time of HEB mixers measured by Berg et al. [36] and the spectral Allan time of the GREAT instrument [10], the spectral and total power Allan times of our receiver should not be limited by the warm IF chain and the DFTS.

3.3.2 Stability of the bias circuit and the cryogenic amplifier

I completed the previous set-up by adding the cryostat containing the cryogenic amplifier and the HEB mixer, as shown in figure 3.12. The cryogenic amplifier has a gain comprised between 36 dB and 43 dB in the bandwidth [0.5 - 1.5] GHz. The bias supply for the HEB has been manufactured at LERMA. See section 2.5 for a more detailed description of the components of our receiver.

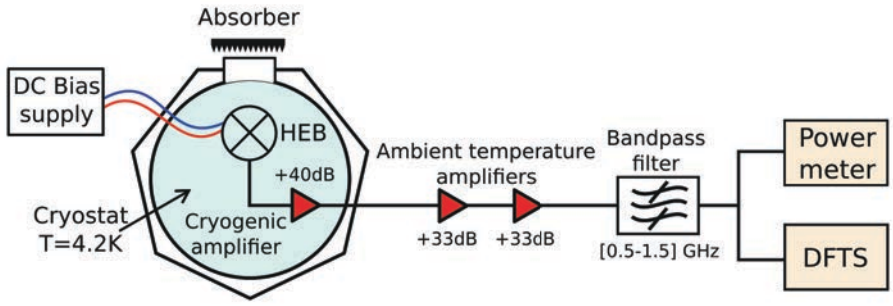

FIGURE 3.12: Set-up of the experiment to measure the stability of the cryogenic amplifier and the HEB bias supply

At first, I only turned on the cryogenic amplifier and biased the HEB with the bias supply. To operate as a mixer, the HEB needs to be biased with a voltage usually between 0.6 mV and 1 mV. When the bias voltage is above 5 mV, the HEB is in a resistive state and starts to behave like any other resistor. To measure the stability of the bias supply, I put the HEB in a resistive state by biasing it with a voltage of 8 mV. Therefore, the only additional noise sources, compared to the previous measurement, are the cryogenic amplifier and the bias supply.

3.3.2.1 Total power Allan variance

We see in figure 3.13 that the total power Allan time of the set-up (IF chain + HEB bias supply), measured by the DFTS is 7 s. The Allan time is calculated as the integration time where the Allan variance diverges of a factor $\sqrt{2}$ from the radiometric line (dashed line), as explained in section 3.2.1.

By comparing the Allan time of 7 seconds obtained here and the 270 seconds obtained with the warm amplifiers and the DFTS, we can conclude that a huge instability appeared, probably because of the cryogenic amplifier or the HEB bias supply. The cryogenic amplifier

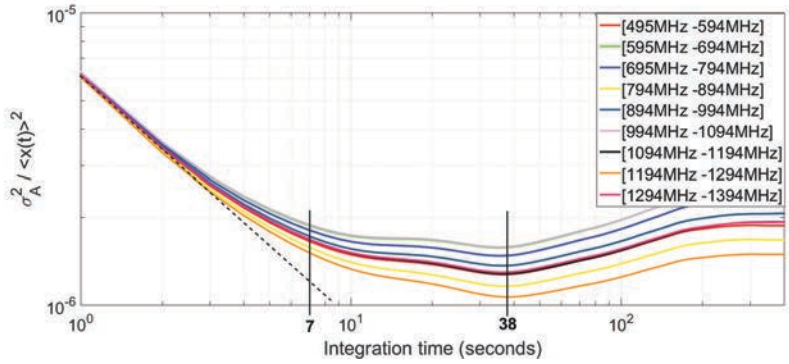

FIGURE 3.13: Total power Allan variance of the IF chain + HEB bias supply

was measured separately and its Allan time was very long (hundreds of seconds). So, I suspect the bias supply to be the cause of the instabilities reducing the total power Allan time of the set-up.

3.3.2.2 Spectral Allan variance

I used the DFTS to measure the spectral Allan variance of the set-up for spectral distances of 1 MHz to 500 MHz between frequency channels (figure 3.14). The measured Allan time is greater than 700 s for channel distances lower than 50 MHz and it is equal to about 153 seconds for channel distances of 100 MHz and 500 MHz. This result shows that the addition of the cryogenic amplifier and the bias supply also reduced the spectral Allan time.

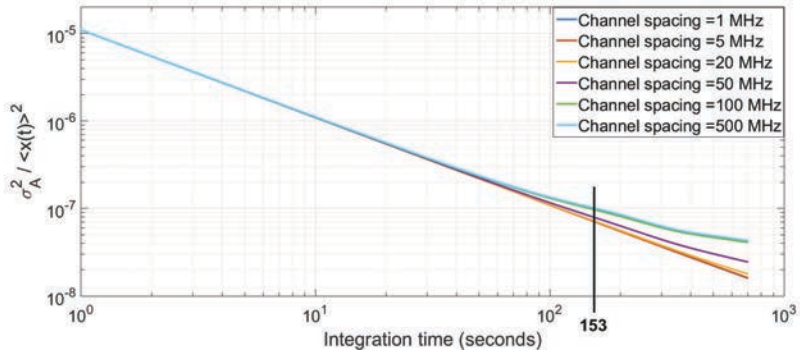

FIGURE 3.14: Spectral Allan variance of the IF chain + HEB bias supply

3.3.2.3 Conclusion

The addition of the cryogenic amplifier and the HEB bias supply greatly increased the instability of the set-up. The total power Allan time has been divided by 39 while the spectral Allan time has been divided by a factor 26. As the cryogenic amplifier has already been tested and showed a really good stability, we are suspecting the bias supply to be the cause of this instability.

3.3.3 Stability of the local oscillator and the HEB mixer

I added a local oscillator (LO) to pump the HEB, and a beam splitter so the HEB can mix the LO signal with the hot load signal (figure 3.15). For this set-up, different LO at different frequencies were used, with the same HEB. It enabled us to compare the stability of the different LOs. Figure 3.16 is a picture of the experiment.

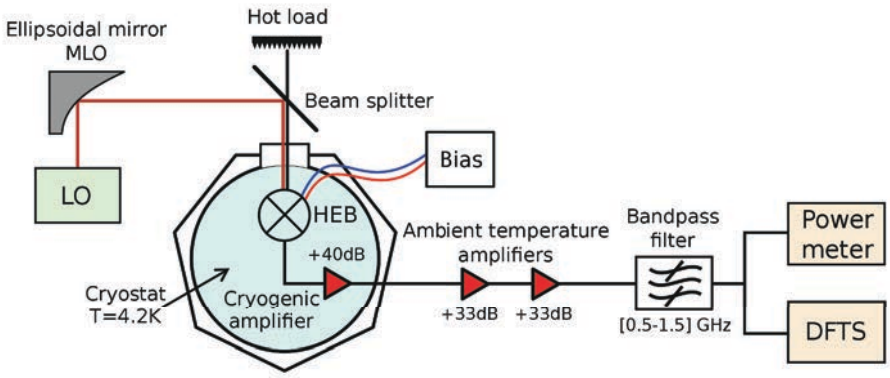

FIGURE 3.15: Set-up of the experiment to measure the stability of the LO and HEB mixer

3.3.3.1 600 GHz LO with a frequency synthesizer

I pumped the HEB with a 600 GHz frequency multiplier chain LO. The initial signal was produced by a frequency synthesizer, then multiplied and amplified by the multiplier chain. The HEB was polarized with the bias supply to 0.8 mV, which is in the range where the HEB is the most sensitive. It is a usual operating bias point for our HEB.

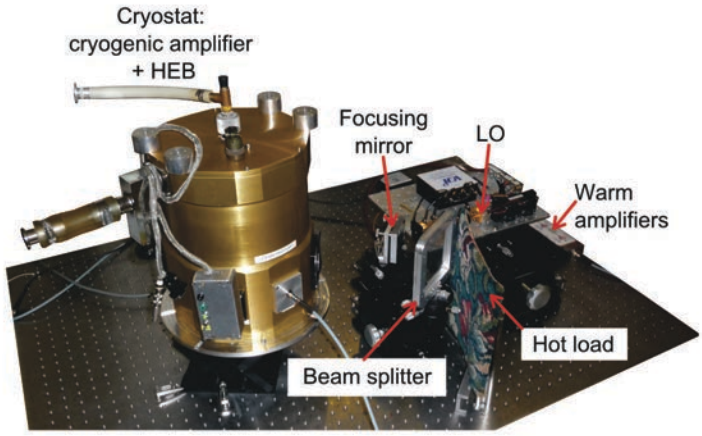

FIGURE 3.16: Picture of the experiment to measure the stability of the LO and HEB mixer

3.3.3.1.1 Total power Allan variance

As shown in figure 3.17, the total power Allan time of the receiver with the 600 GHz LO is between 10 and 15 seconds for 0.18 MHz channels in the range [0.5 - 1.5] GHz.

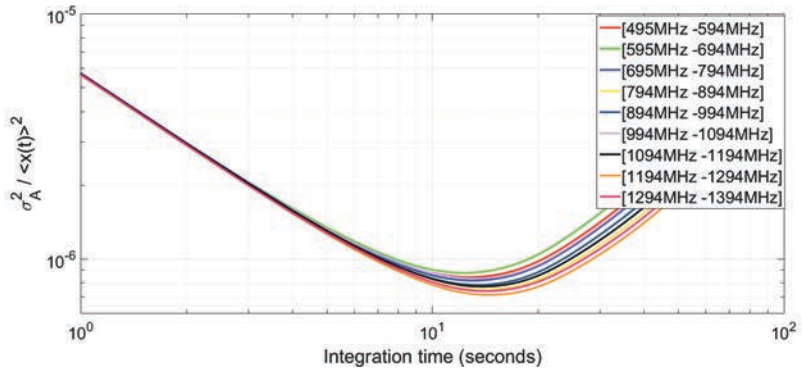

FIGURE 3.17: Total power Allan variance of the receiver with a 600 GHz multiplier chain LO

This Allan time is close and even slightly longer than the Allan time measured previously without the LO. It means that The 600 GHz LO is not limiting the total power stability of the receiver.

3.3.3.1.2 Spectral Allan variance

The spectral Allan time (figure 3.18) measured for the whole receiver with the 600 GHz LO is about 80 seconds for 0.18 MHz channels separated by 500 MHz. However, for different

pumping levels and at different polarization bias voltages, we obtained different Allan times, from 50 to 200 seconds approximately (still for a spectral distance of 500 MHz). This spectral Allan time is slightly shorter, but still comparable, to what we found without the LO. It suggests that the LO could reduce the stability of the receiver but it is not certain.

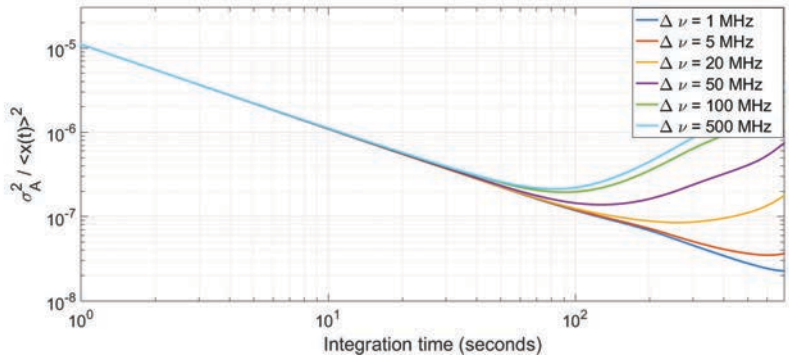

FIGURE 3.18: Spectral Allan variance of the receiver with a 600 GHz multiplier chain LO

3.3.3.1.3 Conclusion

The 600 GHz multiplier chain LO with the frequency synthesizer do not significantly reduce the total power and spectral Allan time of the receiver. This set-up corresponds to a complete heterodyne receiver operating at 600 GHz. The total power Allan time is between 10 and 15 seconds for 0.18 MHz channels, and the spectral Allan variance is about 80 seconds for 0.18 MHz channels separated by 500 MHz. These Allan times are comparable to those of other THz heterodyne receivers such as GREAT [10] and HIFI [37]. At 1200 GHz, GREAT as a spectral Allan time of 100 seconds for 0.85 MHz wide frequency channels separated by 750 MHz, and at 640 GHz, HIFI as a total power Allan time between 7 and 14 seconds for 1.6 MHz channels.

3.3.3.2 1.4 THz LO with a frequency synthesizer

I used the same HEB, at the same polarizing bias voltage (0.8 mV) as before, with a multiplier chain LO operating at 1.4 THz. I tuned the output power of the LO in order to pump the HEB at the same level as with the 600 GHz LO chain. On figure 3.19, each curve corresponds to the normalized power measured by different DFTS channel along time. Surprisingly, we

notice that the power received by the different channels evolve differently along time. For some channels, this variation can even reach tens of % in less than 1 hour.

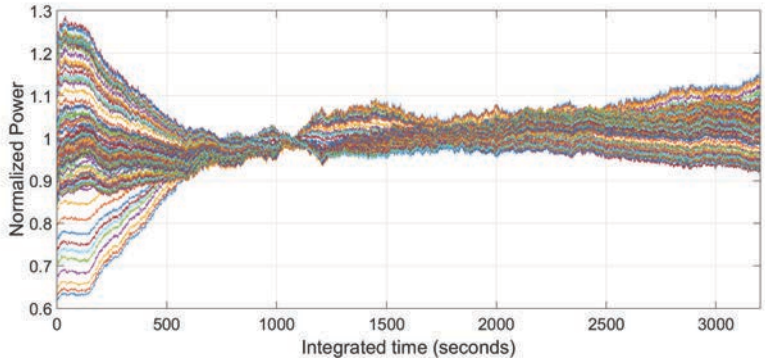

FIGURE 3.19: Normalized IF power of the receiver with a 1400 GHz multiplier chain LO

3.3.3.2.1 Total power Allan variance

The total power Allan time measured with the DFTS channels is comprised between 3 and 5 seconds, depending on the channels' frequency, as shown on picture 3.20.

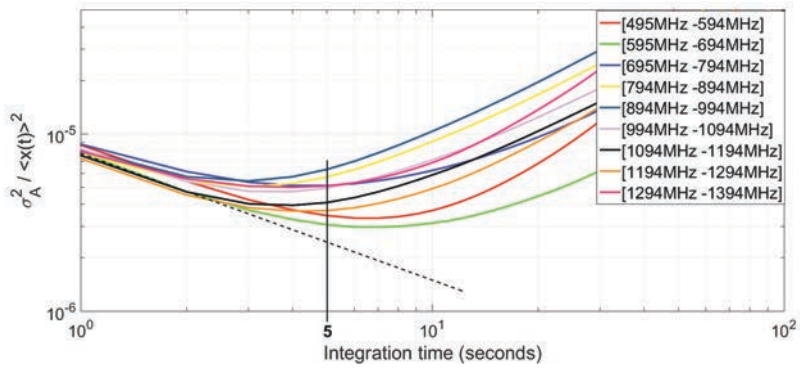

FIGURE 3.20: Total power Allan variance of the receiver with a 1400 GHz multiplier chain LO

3.3.3.2.2 Spectral Allan variance

The spectral Allan time is really short, around 6 seconds for a spectral distance of 500 MHz between the considered channels. It corresponds to a very important stability reduction, compared to the measurements at 600 GHz. The 1400 GHz LO seems to have an important spectral stability problem.

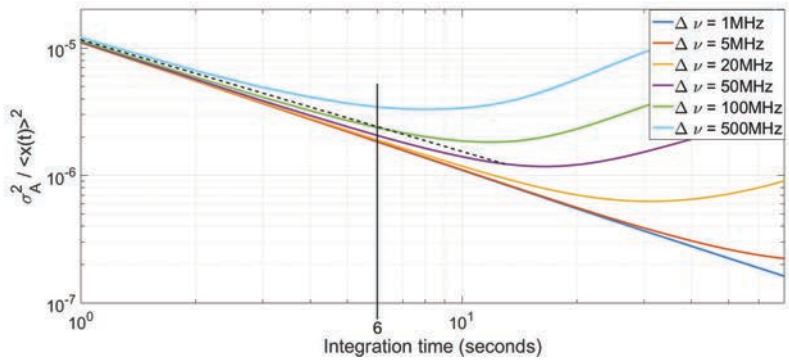

FIGURE 3.21: Spectral Allan variance of the receiver with a 1400 GHz multiplier chain LO

3.3.3.2.3 Conclusion

With the 1400 GHz LO, the receiver has a slightly lower total power Allan time than with the 600 GHz LO, but a really lower spectral Allan time. As shown in figure 3.19, the power variation shown by the channels of the DFTS indicates an important spectrum instability of the LO. This instability could come from the 1.4 THz multiplier chain itself, or from the frequency synthesizer. The same frequency synthesizer has been used with the 600 GHz LO, and we did not see such problem. However, if the synthesizer has a high noise level, some unwanted harmonics and unstable could be multiplied and amplified by the 1.4 THz chain, and not by the 600 GHz.

3.4 Conclusion

I wrote an Allan variance calculation program, optimized for our DFTS spectral data, and I developed a specific measurement process to accurately measure the stability of the different components of a heterodyne receiver. It enabled me to measure the stability of our receiver and its components at 600 GHz and 1.4 THz. I added the different elements of the receiver one by one and measured the stability of the set-up at different stages, in order to determine the stability of the different components. The total power Allan variance was used to measure the stability of the total power of the IF signal, while the spectral Allan variance was used to measure the spectral stability of the IF signal.

In conclusion, with the 600 GHz LO, the total power and spectral stability results were comparable to those of other heterodyne receivers, such as GREAT and HIFI. Moreover, by measuring the total power and spectral Allan variances of all the components I have been able to identify the HEB bias supply as the component that limits the total power stability, and the 1.4 THz LO as the limiting element for the spectral Allan variance. These results will enable us to improve or change the unstable elements we have identified and to improve the stability of our whole heterodyne receiver.

Chapter 4

The Martin Puplett Interferometer (MPI)

4.1 Motivation

In a heterodyne receiver, the radio-frequency (RF) signal from the sky is mixed with the local oscillator (LO) signal in a mixer. This mixing creates an intermediate frequency (IF) signal, which corresponds to the RF signal whose frequency has been down-converted. This down-conversion enables the IF signal to be amplified and processed, and provides heterodyne receivers with a very good spectral resolution, which is very important for radio-astronomy observations. The heterodyne detection principle is illustrated by figure 4.1, and explained in detail in section 2.3. Fundamental unbalanced mixers are the most frequently used in astronomy. They have only one input port, so the RF and LO signals need to be optically superimposed before they reach the mixer input. This superposition is usually achieved with a beam splitter. At frequencies above 1 THz, a typical beam splitter transmits about 90 % of the power and reflects 10 %. It produces a good superposition of the two signals, but loses a lot of LO power (figure 4.1). However, the mixer needs to receive enough LO power to efficiently generate the IF signal.

At frequencies lower than 1.5 THz, LOs emit enough power to be used with a beam splitter, as we can afford to lose 90 % of the LO power. However, at higher frequencies, most LOs emit very little power (a few μW) and we need to couple the LO more efficiently to the mixer. An interesting solution to superimpose the RF and LO signals without losing much

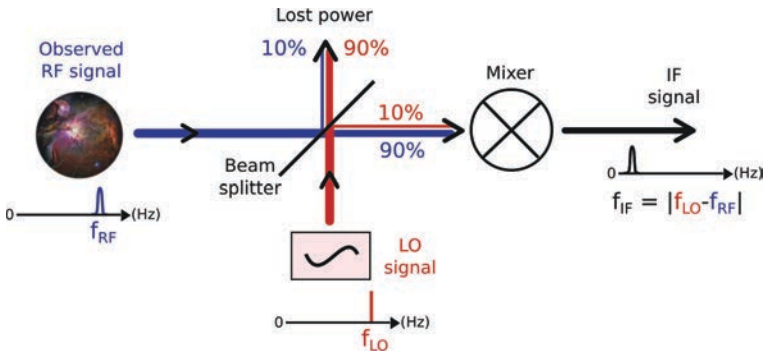

FIGURE 4.1: Schematic showing the down-conversion of the RF signal's frequency and the use of a beam splitter

power is to use a Martin Puplett interferometer. This solution has already been used in several major heterodyne receivers, such as CONDOR [5] and GREAT [10]. As we have a 2.6 THz LO which emits 2 μW and we want to build a heterodyne receiver at this frequency, we decided to design a Martin Puplett interferometer (MPI) for our prototype receiver. To design the different elements of the MPI, we used Gaussian beam optics, which describe well the propagation and different characteristics of Gaussian beams at THz frequencies. The first part of this chapter is dedicated to Gaussian beam optics and provides the necessary background to understand the design of the MPI elements. In the other parts of the chapter, I explain how a MPI works and how our MPI was designed, built and tested. The different parts of this chapter are listed below:

- Presentation of Gaussian beam optics.
- Principle of the Martin Puplett interferometer (MPI).
- Design of of the different elements of our MPI.
- Test of our MPI (for each component and the for whole interferometer).

4.2 Gaussian beam optics

4.2.1 Context and motivation

In geometrical optics, the radiation's wavelength is considered as negligible compared to the dimensions of the system's components (lenses, mirrors, apertures etc.). This approximation usually works well for optics and for frequencies down to the mid-infrared. However, in

the far-infrared, at frequencies between tens of GHz and several THz, the radiation's wavelength becomes closer to the dimensions of the system's elements. The considered system is then called quasioptical. In this frequency domain the diffraction of the beam by the system's elements become more important, and the geometrical optics approximation cannot be used anymore. Instead, we use the Gaussian beam optics equations, which are based on the paraxial wave equation, and accurately describe the propagation of Gaussian beams. Gaussian optics for quasioptics are extensively described in the book *Quasioptical Systems* from Goldsmith [38], and also in the PhD thesis of Golish [39]. At THz frequencies, most laboratory sources use feedhorns and emit beams with a nearly Gaussian amplitude distribution. That is why we can consider our beams as Gaussian and use the Gaussian beam optics to design and simulate our quasioptical systems. Gaussian optics is also widely used to describe laser beams propagation because their radial dimension can be quite small (tens or hundreds of times the wavelength). In this section I introduce the basic concepts and formulas of Gaussian beam optics, which I used to design some elements of the MPI.

4.2.2 Electric field distribution of a Gaussian beam

This section presents the basis of Gaussian beam optics. A more detailed description is given in Appendix A. For a complete demonstration, see Goldsmith [38] and Davis [40]. The distribution of the electric and magnetic field vectors in vacuum and inside materials is accurately described by the Maxwell's equations. We consider a monochromatic paraxial electromagnetic radiation field (paraxial means that the beam propagates close to the optical axis of the system, and makes a small angle with this optical axis). Under these conditions, the electric field of the radiation satisfies the Helmholtz equation.

$$\nabla^2 E(x,y,z) + k^2 E(x,y,z) = 0, \tag{4.1}$$

where ∇^2 is the Laplacian operator, E is the electric field, μ and ϵ are respectively the permeability and permittivity. k is the wave number ($k = 2\pi\nu\sqrt{\epsilon\mu}$) and ν is the frequency of the radiation. After some mathematical transformations described in appendix A, we finally obtain the expression of the normalized electric field distribution for the fundamental Gaussian mode:

$$E(r,z) = \sqrt{\frac{2}{\pi\omega^2}} \exp\left(\frac{-r^2}{\omega^2} - jkz - \frac{j\pi r^2}{\lambda R} + j\phi_0\right), \tag{4.2}$$

where r is the radial distance to the propagation axis ($r = \sqrt{x^2+y^2}$), ω is the radius of the beam and R its radius of curvature (figure 4.2). The radius ω of the beam corresponds to the radial distance at which the electric field is divided by e compared to its value on the axis of propagation. Both ω and R vary with z, the position on the propagation axis. λ is the wavelength of the radiation and ϕ_0 is the Gaussian beam phase shift, also called Gouy phase shift. It corresponds to the phase shift between the considered Gaussian beam and a plane wave at the same frequency. Equation 4.2 describes the propagation of Gaussian beams along the propagation axis (z) at any radial distance distance r from the axis. The expression of the electric field is normalized so $\int_0^\infty |E|^2 2\pi r.dr = 1$. The different physical parameters characterizing Gaussian beams can be deduced from this equation, as shown in appendix A. The most important equations are listed in the following section.

4.2.3 Gaussian beam characteristics

4.2.3.1 Beam waist and radius

Gaussian beams described by the Gaussian beam optics' equations never converge to a point with an infinitely small radius, as in geometrical optics. Gaussian beams converge until their radius, ω, reaches a minimum radius called beam waist (ω_0), then they start to diverge (figure 4.2).

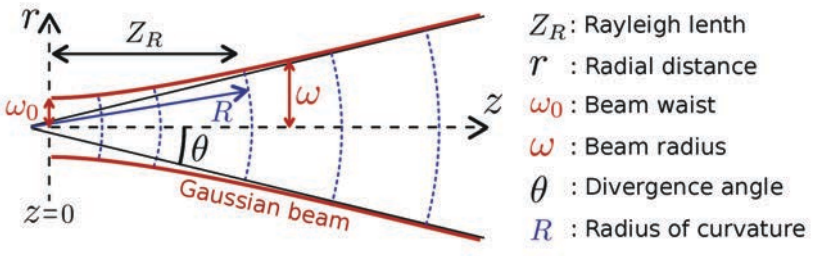

FIGURE 4.2: Characteristics of a Gaussian beam

By knowing the beam waist, we can calculate the beam radius of the beam along the propagation axis with the equation:

$$\omega = \omega_0 \sqrt{1 + \left(\frac{\lambda z}{\pi \omega_0^2}\right)^2}, \tag{4.3}$$

where z is the position on the propagation axis and λ the wavelength of the beam. The position z=0 is located at the beam waist.

4.2.3.2 Amplitude and power repartition

The amplitude of Gaussian beams is maximum on the axis of propagation and decreases when the radial distance r to this axis increases, as shown in figure 4.3. This radial amplitude distribution is Gaussian, and is described by the following equations:

$$\frac{|E(r,z)|}{|E(0,z)|} = \exp\left[-\left(\frac{r}{\omega}\right)^2\right], \tag{4.4}$$

$$\frac{P(r,z)}{P(0,z)} = \exp\left[-2\left(\frac{r}{\omega}\right)^2\right], \tag{4.5}$$

where E is the electric field amplitude and P the power of the beam. We also see in figure 4.3 that, at a distance $r = \omega$ from the propagation axis, the power of the Gaussian beam corresponds to $e^{-2} = 0.135$ times the power on the propagation axis.

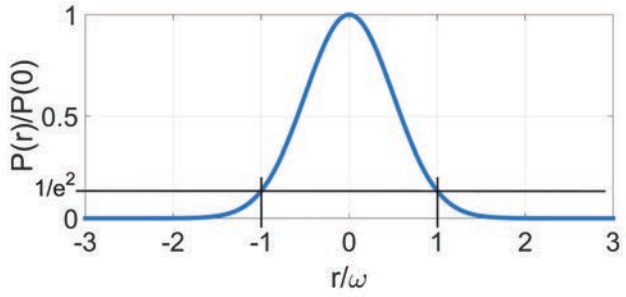

FIGURE 4.3: Relative power of the beam along the radius r

To design the elements of a quasioptical system (mirrors, lenses, gratings etc.), we need to know what fraction of the total Gaussian beam power (FP) will reach the element. For example, we want to make sure that a mirror is large enough to reflect more than 99.9 % of the incoming beam. Equation 4.6 is used to calculate the fractional power ($FP(r)$) included in a circular aperture with a radius r:

$$FP(r) = \frac{\int_0^r P(r)2\pi r.dr}{\int_0^\infty P(r)2\pi r.dr} = 1 - \exp\left[-2\left(\frac{r}{\omega}\right)^2\right]. \tag{4.6}$$

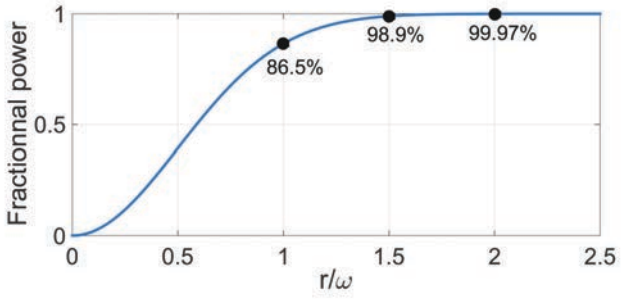

FIGURE 4.4: Fractional power included in a disk of radius r

We see in figure 4.4 that when a beam is truncated by a circular aperture with a radius of 2ω (diameter of 4ω), 99.97 % of the Gaussian beam power is transmitted. That is why, when designing quasioptical systems, the minimum length or diameter of the elements is often 4ω, to be sure that they will receive almost all the initial Gaussian beam power, even if they are not perfectly aligned. In equation 4.6, only the truncated power of the fundamental order Gaussian beam is considered. The truncated power of all the Gaussian beam modes could be higher.

4.2.3.3 The radius of curvature

At the beam waist position, the radius of curvature of the beam is infinite, because the wavefront is plane. At other positions on the propagation axis, the radius of curvature R becomes smaller because the wavefront is curved (cf figure 4.2). The radius of curvature of the Gaussian beam can be calculated for every position z on the propagation axis with the equation:

$$R = z + \frac{1}{z}\left(\frac{\pi\omega_0^2}{\lambda}\right)^2. \tag{4.7}$$

4.2.3.4 The farfield divergence angle

After the beam waist, the Gaussian beam diverges and its radius increases. We define the farfield divergence angle θ as the asymptotic growth angle of the beam radius ω as a function

of the distance z from the beam waist (see figure 4.2). This divergence angle is calculated with the equation below:

$$\theta = \lim_{z\to\infty} tan^{-1}\left(\frac{\omega}{z}\right) = tan^{-1}\left(\frac{\lambda}{\pi\omega_0}\right). \tag{4.8}$$

4.2.3.5 The Rayleigh length

The Rayleigh length (Z_R) corresponds to the distance from the beam waist at which the beam radius is $\omega = \omega_0\sqrt{2}$. At distances $z < Z_R$ from the beam waist, the beam's growth is slow and the Gaussian beam is considered as collimated.

$$Z_R = \frac{\pi\omega_0^2}{\lambda}. \tag{4.9}$$

4.2.3.6 Other useful equations

Other useful equations can be deduced from equations 4.3 and 4.7:

$$\omega_0 = \frac{\omega}{\sqrt{1+\left(\frac{\pi\omega^2}{\lambda R}\right)^2}} \quad \text{and,} \quad z = \frac{R}{1+\left(\frac{\lambda R}{\pi\omega^2}\right)^2}. \tag{4.10}$$

4.2.4 Conclusion

At sub-millimeter wavelengths, laboratory sources often use feedhorns and emit beams whose shape is very close to Gaussian beams. Gaussian beam optics provide useful equations to accurately describe the propagation of quasioptical beams along the propagation axis. I used some of the Gaussian beam equations to design the Martin Puplett interferometer for our 2.6 THz prototype heterodyne receiver.

4.3 Description of the MPI

4.3.1 Input of the MPI

Most mixers need to receive the LO and RF signals superimposed and with the same polarization, in order to efficiently produce the IF signal. When using a Martin Puplett interferometer (MPI), the superposition of the LO and RF signals is done by the first wire grid G1. However, after G1, the LO and RF signals have orthogonal polarizations. The purpose of the MPI is to rotate one of the polarizations by 90° without much losses, so both LO and RF signals have the same polarization at the output of the MPI. The MPI is composed of a second wire grid, G2, and two roof-top mirrors, T1 and T2, (figure 4.5).

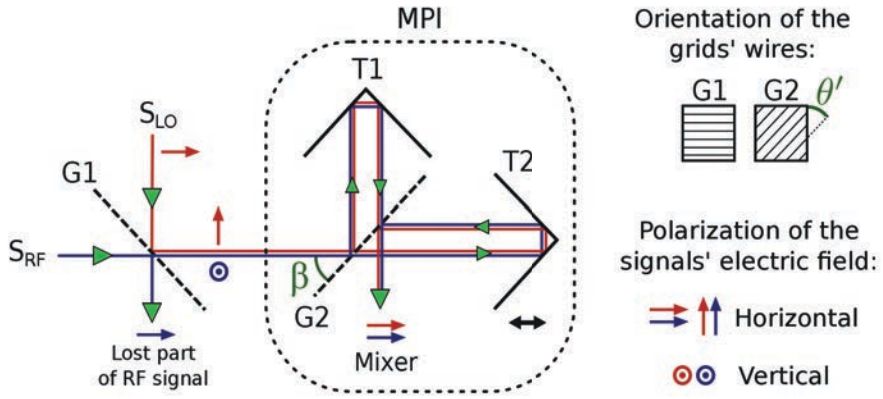

FIGURE 4.5: MPI with two grids, to be used as diplexer in a heterodyne receiver

Wire grids have the particularity of polarizing electromagnetic waves. A correctly dimensioned wire grid reflects the $\vec{E}$ field parallel to its wires and transmits the $\vec{E}$ field perpendicular to its wires. As the LO signal is already polarized (vertically or horizontally), we set the grid G1 in order to completely reflect it. The RF signal is usually not polarized, so half of it is transmitted by G1, and the other half is reflected and lost (most mixers only detect one polarization anyhow). As shown in figure 4.5, the grid G1 is able to superimpose the LO signal with half of the RF signal, but their polarizations are orthogonal. As the mixer needs the two input signals to have the same polarization, a MPI is used to rotate the polarization of one of them by 90°.

4.3.2 Detailed description of the elements of the MPI

The rotation of the polarization of one of the MPI's input signals is achieved by the association of two roof-top mirrors and a wire grid. In order to understand this polarization rotation, it is necessary to describe the functioning of the roof-top mirrors and of the free standing wire grids. A good description of the MPI and its elements can be found in the book *Millimetre-Wave Optics, Devices and Systems*, from Lesurf [41] and in the book *Quasioptical Systems : Gaussian Beam Quasioptical Propogation and Applications* from Goldsmith [38].

4.3.2.1 The free standing wire grid

A polarizing grid is composed of parallel metal wires, whose diameter and spacing must be small compared to the wavelength of the signal. If this requirement is respected, the grid polarizes the incoming signal by efficiently reflecting the $\vec{E}$ field parallel to its wires and transmiting the $\vec{E}$ field perpendicular to its wires. As a result, the polarizations of the transmitted and reflected signals are orthogonal. In the MPI, the grid G2 is used as a beam splitter to divide the incoming RF and LO signals (figure 4.5). The reflected and transmitted signals must be equally powerful, which requires the wires of G2 to be 45° inclined, with respect to the linear polarization of the incoming beams. However, the MPI grid G2 is not perpendicular to the input signals, but makes an angle $\beta = 45°$ (figure. 4.5). So, we have to take into account the projected angle of the grid's wires on the input signal's plane. Figure 4.6 shows this projection and we can deduce the relation between the polarizing angle θ and the real inclination angle of the MPI grid's wires, θ'.

$$\theta' = tan^{-1}(tan(\theta)cos(\beta)) \tag{4.11}$$

$$\text{And, with } \beta = 45°, \quad \theta' = tan^{-1}(tan(\theta)/\sqrt{2}) \tag{4.12}$$

As we want G2 to have a polarization angle $\theta = 45°$, the wires of G2 must have an inclination angle $\theta' = 35.26°$.

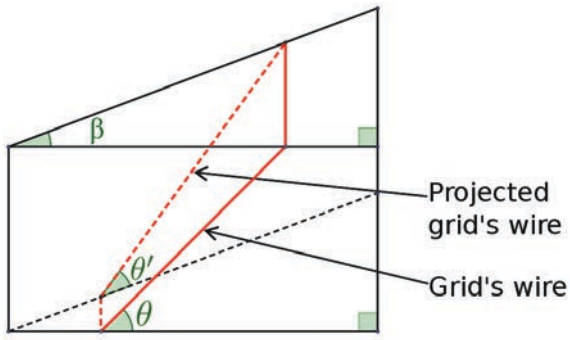

FIGURE 4.6: Projected inclination angle of the MPI grid's wires

4.3.2.2 The roof top mirrors

The roof-top mirrors T1 and T2 are composed of two orthogonal flat faces. In the MPI, the roof-top mirrors are used to reflect the signals reflected or transmitted by the grid G2, back to G2 (figure 4.5). Each input signal reaching a roof-top mirror is reflected twice (once on each face). Its polarization stays unchanged but the direction of the signal is inverted (because it is reflected), as illustrated in figure 4.7. As a result, in the referential of the beam, its polarization is unchanged, but in the referential of the MPI the polarization is rotated by 2θ. The signals reaching T1 and T2 have a polarization angle of $\theta = \pm 45°$. After being reflected by the roof-top mirrors, their polarization is rotated by 90°. Therefore, the signals which have initially been transmitted by G2 are reflected by G2 and the signals initially reflected by G2 are transmitted by G2.

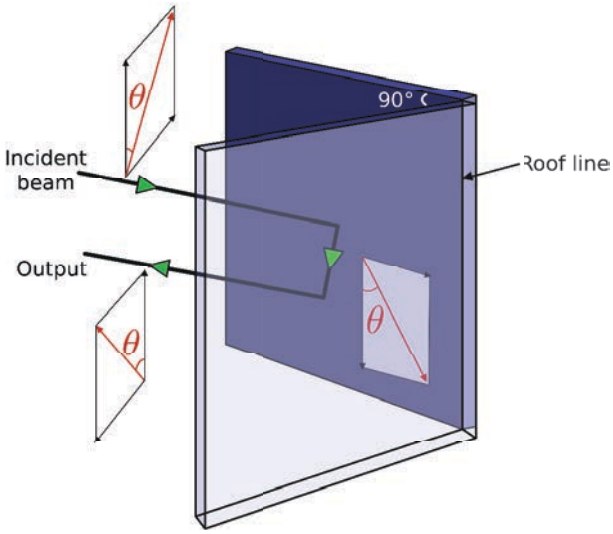

FIGURE 4.7: Change of the polarization produced by a roof-top mirror

Finally, the LO and RF signals which have been transmitted from G1 to G2, integrally reach the output of the MPI after having been split by G2, reflected by T1 and T2, and recombined by G2.

4.3.3 The rotation of the polarization in the MPI

The description of the roof-top mirrors and the polarizing grids explains why the totality of the RF and LO signals sent to G2, at the input of the MPI, is present at the output of the MPI and reaches the mixer. The rotation of the polarization of one of the input signals of the MPI is achieved by translating the roof-top mirror T2. The translation changes the path difference ΔZ between the two arms of the MPI ($\Delta Z = ||G2 - T1| - |G2 - T2||$) and can modify the polarization of any signal going through the MPI:

- If $\Delta Z = n\lambda$, the polarization of the signal going through the MPI is not changed.
- If $\Delta Z = (n + \frac{1}{2})\lambda$, the polarization of the signal going through the MPI is rotated by 90° at the output of the MPI.
- For other values of the ΔZ, the polarization of the signal going through the MPI is elliptic at the output of the MPI.

where $n \in \mathbb{N}$ and λ is the wavelength of the signal.

As the LO and RF signals have slightly different frequencies, there are path differences ΔZ which are equal, at the same time, to $n_1\lambda_{LO}$ and to $(n_2 + \frac{1}{2})\lambda_{RF}$, (with $n_1, n_2 \in \mathbb{N}$). As a result, these path differences ΔZ do not rotate the polarization of the LO signal but rotate the polarization of the RF signal by 90°. For the detail of the calculation of the polarization rotation by the MPI, see appendix B.

4.3.4 The bandwidth of the MPI

The LO signal has a very narrow bandwidth, so we can almost consider it as a monochromatic signal. The RF signal we receive from the sky, on the contrary, covers all the spectrum. However, the MPI cannot rotate the polarization of the totality of the RF spectrum by 90°. As explained in section 4.3.3, the path difference between the 2 arms of the MPI, ΔZ, is

optimized to only rotate by 90° the polarization at one frequency (f_{RF}) of the RF signal. The polarization of the rest of the RF spectrum, covering different frequencies (f_{rf}), is differently rotated. The polarization of the RF signal determines the efficiency of the mixer, so it is important to know the response of the MPI over the RF spectrum.

The grid G2 divides the RF signal into two equal power signals, s_1 and s_2, whose polarizations are $p_1 = 45°$ and $p_2 = -45°$. At the output of the MPI, s_1 and s_2 are superimposed, and the amplitude A of the output signal is:

$$A = \frac{A_0}{2}\left[1 + cos\left(\frac{2\pi(\delta n - \frac{1}{2})\delta f}{\Delta f}\right)\right]||\vec{e_v}|| + \frac{A_0}{2}\left[1 - cos\left(\frac{2\pi(\delta n - \frac{1}{2})\delta f}{\Delta f}\right)\right]||\vec{e_h}||, \quad (4.13)$$

where $\delta f = f_{LO} - f_{rf}$, and f_{rf} is a frequency of the RF spectrum. $\delta n \in \mathbb{N}$, $\Delta f = f_{LO} - f_{RF}$, with f_{RF} the frequency for which the MPI was optimized, and f_{LO} the LO frequency. A_0 is the amplitude of the RF signal at the input of the MPI. The vectors corresponding to the vertical and horizontal polarizations are $\vec{e_v}$ and $\vec{e_h}$. We are only interested in the horizontal polarization of the RF signal because, in this example, it is the polarization of the LO signal. So we can plot the power transmission (transmittance) of the horizontal component of the output signal:

$$T = \frac{1}{2}\left[1 - cos\left(\frac{2\pi(\delta n - \frac{1}{2})\delta f}{\Delta f}\right)\right]. \quad (4.14)$$

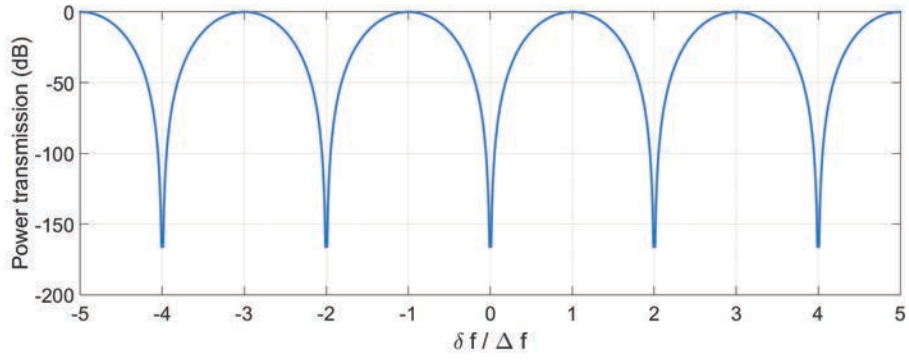

FIGURE 4.8: Bandwidth of the MPI for the horizontal component of the RF signal

Figure 4.8 shows the transmittance of the horizontal component of the RF signal when varying $\delta f/\Delta f = (f_{LO} - f_{rf})/(f_{LO} - f_{RF})$, for $\delta n = 1$. We see on this plot that the transmitted power is maximum for $\delta f/\Delta f = 1 + 2k$, $(k \in \mathbb{Z})$. We can verify that, for $f_{rf} = f_{RF}$, $\delta f/\Delta f = 1$. So, the transmittance of the MPI is maximum at the RF frequency for which the path difference ΔZ was optimized, which is consistent with our previous calculations. The -3 dB bandwidth of the MPI corresponds to the range where the transmittance is better than -3 dB:

$\delta f/\Delta f \in [0.637, 1.363] + 2k$, $(k \in \mathbb{Z})$.

For example, if $\Delta f = 1.5\ GHz$, we will have $f_{LO} - f_{rf} \in [0.96, 2.04] + 3k$ GHz. So, in this case, the part of the RF spectrum transmitted by the MPI with less than 3 dB losses is between 0.96 GHz and 2.04 GHz, with a period of 3 GHz.

4.4 Design of our MPI

Our MPI has been designed to work with our 2.6 THz LO. Because of its very low output power (2 μW), a usual beam splitter induces too many losses and a MPI is a good solution to superimpose the LO and RF signals without losing too much LO power. The intermediate frequency (IF) of the MPI ($f_{LO} - f_{RF}$) was chosen to be centered on 1.5 GHz, as it corresponds to the middle of our mixer's bandwidth. This value of IF requires a path difference Δ Z = 10 cm between the two arms of the MPI, and the -3 dB bandwidth of the MPI corresponds to the range [0.96 GHz , 2.04 GHz]. Our MPI is composed of the two roof-top mirrors (T1 and T2) and the polarizing grid (G2), which are the main components of the MPI. In addition, we also have another polarizing grid (G1) which superimposes the RF and LO signals at the input of the MPI, and an ellipsoidal mirror (MLO) to focus the LO beam before G1. The schematic of this MPI is shown in figure 4.9, where a cold load is used to generate the RF signal. A picture of our MPI is shown in figure 4.10.

4.4.1 Calculation of the ellipsoidal mirror (MLO)

Our 2.6 THz LO emits a Gaussian beam with a waist of 0.21 mm and we need to feed our mixer with a beam whose waist is 1.5 mm. As the signal emitted by the LO is very diverging, we decided to focus it with an ellipsoidal mirror before it reaches the MPI. The ellipsoidal

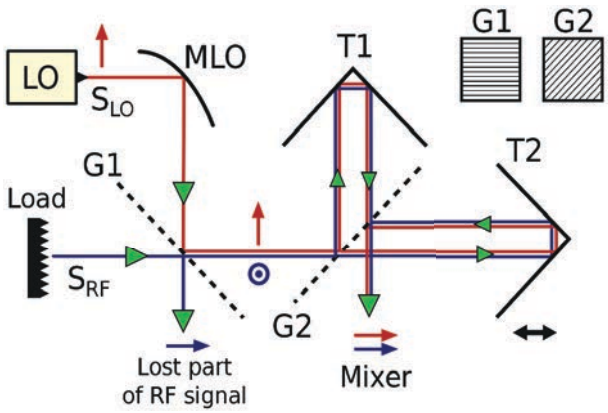

FIGURE 4.9: Schematic of our MPI setup

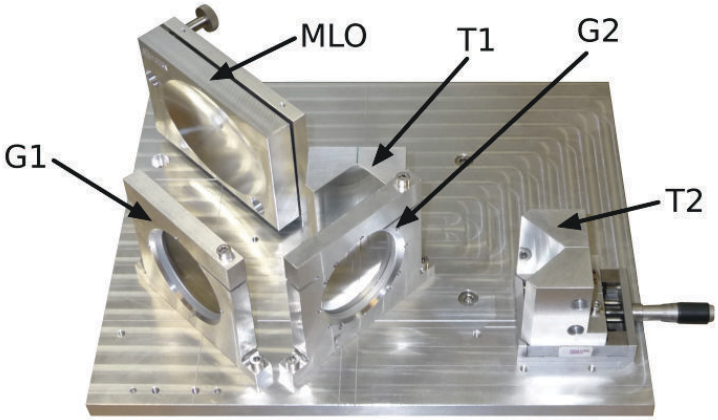

FIGURE 4.10: Picture of our Martin Puplett Interferometer

mirror (MLO) was specifically designed to match the (simulated) beam pattern of the HEB at 2.6 THz. The optical path from the MLO to the mixer (located at the output of the MPI) is z = 490 mm. According to the quasioptical formula 4.15, we know that our beam needs to have a radius $\omega = 12.1$ mm on the ellipsoidal mirror MLO to generate a beam waist of 1.5 mm 49 cm further, at the input of the mixer.

$$\omega(z) = \omega_0 \sqrt{1 + \left(\frac{z\lambda}{\pi\omega_0^2}\right)^2} = 12.1 \text{ mm}. \tag{4.15}$$

With the same formula, we deduce that we need a distance z = 69.1 mm between the LO and the MLO to have a beam radius of 12.1 mm on the MLO. With these parameters, I was able to calculate the characteristics of the required ellipsoidal mirror (MLO). An ellipsoidal mirror is

a part of an ellipsoid of revolution, so it is characterized by its two radii of curvature, which are calculated with the following formula:

$$R(z) = z + \frac{1}{z}\left(\frac{\pi\omega_0^2}{\lambda}\right)^2. \tag{4.16}$$

So, we have $R(69.1) = R_1 = 69.1$ mm and $R(490) = R_2 = 498$ mm, which are the two radii of curvature of the MLO. As we know that the angle θ between the incoming and reflected beams is 90°, it enables us to calculate the shape of the MLO. The ellipsoidal surface of the mirror is the surface created by the red line when we rotate the ellipse, represented on figure 4.11, around its major axis. On figure 4.11 the distances $|F1P|$ and $|F2P|$ correspond to the two radii of curvature R_1 and R_2.

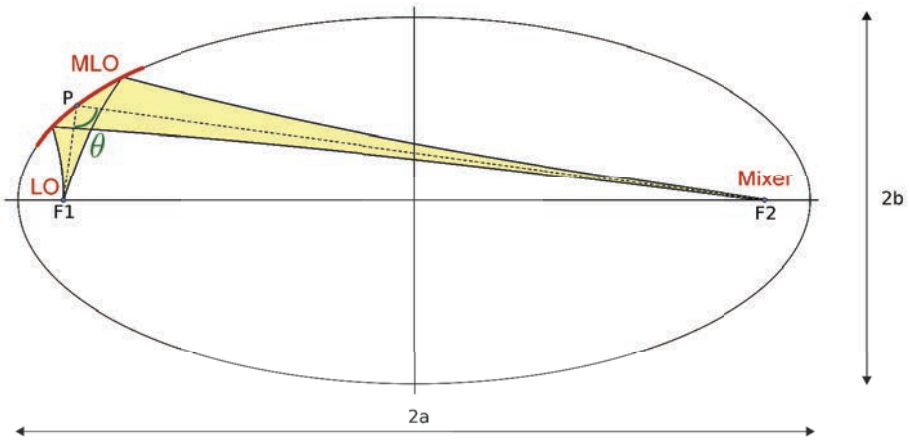

FIGURE 4.11: Schematic of the ellipsoidal mirror (MLO)

Equation 4.15 also enabled me to calculate the beam radius at the position of each optical element (mirrors and grids), to ensure that the beam completely reaches each element and no power is lost (Table 4.1). I made sure that the size of the optical elements was 4 times bigger than the radius of the beam, as explained in section 4.2.3.2. In table 4.1, ω_{ini} is the radius of the beam at the first element of the segment and ω_{end} is the radius of the beam at the last element of the segment. The column *Distance* indicates the length of each segment. We see that the HEB mixer receives two beams with a slightly different radius, it is due to the fact that the two arms of the MPI do not have the same length.

MPI segment	ω_{ini} (mm)	Distance (mm)	ω_{end} (mm)
LO – MLO	0.21	69.00	12.07
MLO – G1	12.07	100.00	9.65
G1 – G2	9.65	100.00	7.24
G2 – T1	7.24	50.00	6.05
G2 – T2	7.24	100.00	4.87
T1 – G2	6.05	50.00	4.87
T2 – G2	4.87	100.00	2.65
G2 – HEB	4.87	140.00	1.93
G2 - HEB	2.65	140.00	1.95

TABLE 4.1: Radius of the beam on each element of the MPI

4.4.2 Calculation of the grids' required characteristics

4.4.2.1 Absorbance of free standing wire grids

We need to consider the power absorption (absorbance) of the grids. Volkov et al. [42] measured it and found less than 1 % at a few hundreds of GHz. So, the absorbance seems to be quite low and almost negligible. So, for this theoretical study I considered the absorbance of the grids negligible. Therefore, we have $R_{//} \approx 1 - T_{//}$ and $R_{\perp} \approx 1 - T_{\perp}$.

However, the absorbance of the parallel polarization is expected to increase with the frequency (cf. Goldsmith [38, page 193]), because it depends on the surface resistance of the metallic wires. As the parallel polarization is mostly reflected by the grid, this increased absorbance should mostly affect the reflected signal, and not the transmitted one. Some experimental results, presented in section 4.6, are in favour of this hypothesis.

4.4.2.2 Transmittance of the grids for normally incident beams

The polarizing wires grids of the MPI, G1 and G2, are very important because their polarizing efficiency has an important impact on the total MPI's efficiency. In this section I determine their required characteritics to efficiently polarize a 2.6 THz signal.

Typical free standing wire grids for THz frequencies are made of tungsten wires (sometimes gold plated), whose diameter is a, and whose spacing is g. The grids' properties are evaluated for 2 different polarizations: when the $\vec{E}$ field is perpendicular to the grid's wires, and when it is parallel (figure 4.12).

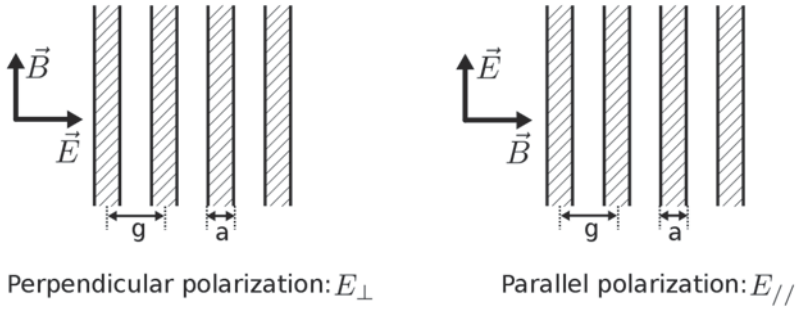

FIGURE 4.12: Perpendicular and parallel $\vec{E}$ polarizations

For these two configurations, I used the formulas presented in the paper from Blanco et al. [43] to calculate and plot the transmittance of a grid, with different parameters. $T_\perp$ is the transmittance of the grid when the $\vec{E}$ field is perpendicular to the wires, and $T_{//}$ is the transmittance of the grid when the $\vec{E}$ field is parallel to the wires. A perfect polarizing grid would have $T_{//} = 0$ and $T_\perp = 1$, and we want our grids to be as close to these values as possible. In this section I consider that the absorbance of the grids is negligible, as explained in section 4.4.2.1. Therefore, we have the following relation between the transmittance T and the reflectance R, for both perpendicular and parallel polarizations:

$$R_{//} \approx 1 - T_{//} \quad \text{and} \quad R_\perp \approx 1 - T_\perp. \tag{4.17}$$

The formulas from Blanco et al. [43] enabled me to calculate the transmittance coefficients expected for wire grids with a regular spacing. The mathematical model used in the article from Blanco et al. seems quite reliable because it has been compared to the results measured by Volkov et al. [42] and with the theoretical study of Suratteau and Petit [44]. To know the influence of the wires' diameter (a) on the grid's efficiency, I plotted the transmittance of the grid for different values of a/g (figure 4.13).

We easily notice that when $a/g = 0.14$, the perpendicular polarization ($E_\perp$) is well transmitted, but the parallel polarization ($E_{//}$) is not completely reflected. When $a/g = 0.29$, both polarizations are less transmitted (and more reflected). As a result, to have an efficient behavior of the grid ($E_\perp$ well transmitted and $E_{//}$ well reflected), it is better to have a ratio a/g between 0.25 and 0.29. We also notice on figure 4.13 that the ratio between the wire spacing g and the wavelength of the signal λ has an effect on the grid's efficiency. On

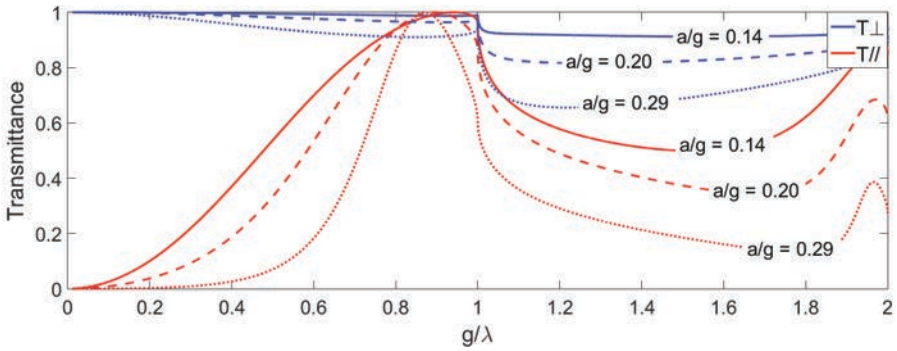

FIGURE 4.13: Transmittance of polarizing grids for different values of a and g

figure 4.14, I plotted the transmittance of the grid for $a/g = 0.25$ and $a/g = 0.29$ and for values of g/λ inferior to 0.5.

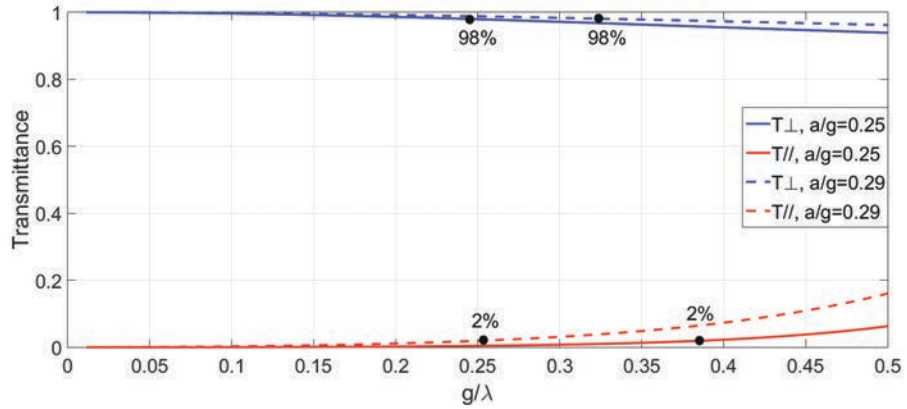

FIGURE 4.14: Transmittance of the grid over g/λ

Figure 4.14 shows that the power efficiency of the grid is better than 98 % ($T_{\perp} > 98$ % and $R_{//} > 98$ %) when $g/\lambda < 0.25$, for $a/g \in [0.25 \;\; 0.29]$. In conclusion, the ratios g/λ and a/g are the two parameters we should take into account to choose our MPI grids.

4.4.2.3 Transmittance of the grids for oblique incident beams

The two grids of our MPI, G1 and G2, make an angle $\beta = 45°$ with the incident beams. This parameter also has to be taken into account to predict the efficiency of our grids. The incidence angle artificially reduces the spacing g between the wires, but the wires' diameter stays identical, so the quotient a/g increases. According to figure 4.13, when a/g increases $T_{//}$ and $T_{\perp}$ decrease. So, the 45° incidence angle reduces the transmittance of both perpendicular and parallel polarizations. This effect can be calculated with the same theoretical

equations as before (cf. Blanco et al. [43]), by dividing the spacing between the wires, g, by $\sqrt{2}$. So, for a 45° incidence angle, the best a/g ratio to have optimum grid parameters for both polarizations is:

$$a/g \in \frac{[0.25 \quad 0.29]}{\sqrt{2}} \quad \Longleftrightarrow \quad a/g \in [0.18 \quad 0.21]. \tag{4.18}$$

4.4.2.4 Selection of our MPI grid

An efficient grid, with a 45° orientation angle, should have a ratio a/g between 0.18 and 0.21, and a ratio g/λ smaller than 0.3 (where a is the wires' diameter, g the wire spacing and λ the wavelength of the beam). The best solution for frequencies up to 3 THz would be: a = 5 μm and g = 25 μm. It corresponds to $a/g = 0.2$, and it gives at 2.6 THz, $T_{//}$ = 0.2 % and $T_{\perp}$ = 99.6 %. However, because of availability and cost reasons, we had to compromise and chose a slightly less efficient grid. The solution we chose was to order the grids G1 and G2 with a = 10 μm and g = 35 μm. It gives $g/\lambda = 0.30$ and $a/g = 0.29$. Figure 4.15 describes the theoretical efficiency of our MPI grids at 600, 1400 and 2600 GHz, for a normal incidence and a 45° incidence angle.

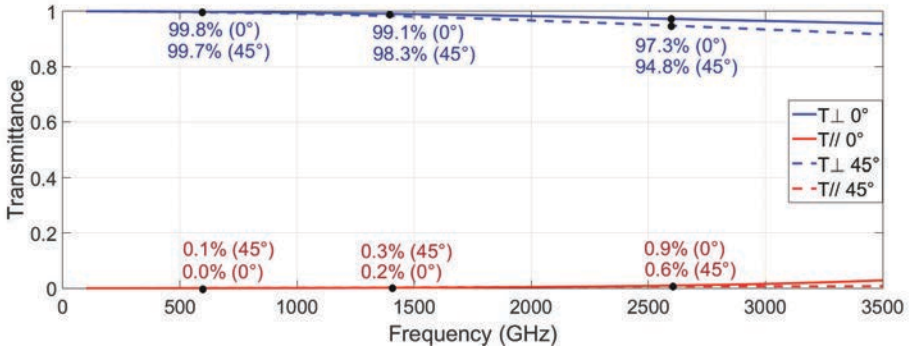

FIGURE 4.15: Transmittance of the grid at our frequencies (600, 1400 and 2600 GHz)

At 2.6 THz, the grids we chose (a = 10 μm and g = 35 μm) should have the following transmittance characteristics:

$$\text{Normal incidence:} \quad T_{\perp} = 97.3\ \% \quad \text{and} \quad T_{//} = 0.9\ \%$$

$$45° \text{ incidence:} \quad T_{\perp} = 94.8\ \% \quad \text{and} \quad T_{//} = 0.6\ \%$$

4.4.2.5 Conclusion

The wire grids we chose show a good theoretical efficiency, except for the perpendicular polarization at 45° and at a frequency of 2.6 THz, where the efficiency drops to 94.8 %. In the future, more efficient grids would be desirable to increase the efficiency of our MPI.

4.5 Test and evaluation of each individual component of the MPI

Losses on the RF signal reduce the sensitivity of the whole heterodyne receiver. That is why it is very important to reduce the MPI losses as much as possible. A beam splitter used at lower frequencies usually loses between 5 % and 10 % of the RF signal, and we want the MPI at 2.6 THz to have less than 20 % losses. In order to evaluate and reduce the MPI losses, it is necessary to evaluate the losses of each component, before assembling the MPI and measuring its total efficiency.

4.5.1 The ellipsoidal mirror (MLO)

4.5.1.1 Roughness of the MLO

The reflection losses of an ellipsoidal mirror are not easily measurable because the waist of the beam changes due to the focusing, so the coupling with the detector is not the same before and after the mirror. That is why, we measured the surface accuracy and roughness of the mirror and compared it with theoretical design to evaluate its performance. We used a profilometer (Dektak 8), with a resolution of 10 nm, to measure the roughness of the mirror's surface. To calculate the roughness, the profilometer measured the vertical variations over a distance of 1 mm on the surface of the mirror. We took about 10 measurements of 1 mm on the mirror's surface to have a good estimation of its roughness. We always measured an rms roughness Rq below 600 nm (and an average roughness Ra below 500 nm). The roughness of the mirror is responsible for the scattering of the beam. According to Ruze's formula (eq. 4.19), the power losses due to the scattering of a 115 μm wavelength (2.6 THz) signal on a metallic surface, whose maximal rms roughness is smaller than 600 nm, are

$$ScatteredPower < 1 - exp\left[-\left(\frac{4\pi Rq}{\lambda}\right)^2\right] = 0.4\ \%. \tag{4.19}$$

As a conclusion, the losses due to the mirror's roughness can be considered as negligible at 2.6 THz (and at lower frequencies).

4.5.1.2 Shape of the MLO

I also studied the shape of the mirror and characterized it with a manual three dimensional machine (Brown and Sharp), whose accuracy is 4 µm. The dimensions of the MLO mirror are 88.8 mm for its major axis, and 62.5 mm for its minor axis. I measured the depth profile along the major axis of the MLO and compared it with the theoretical design (figure 4.16).

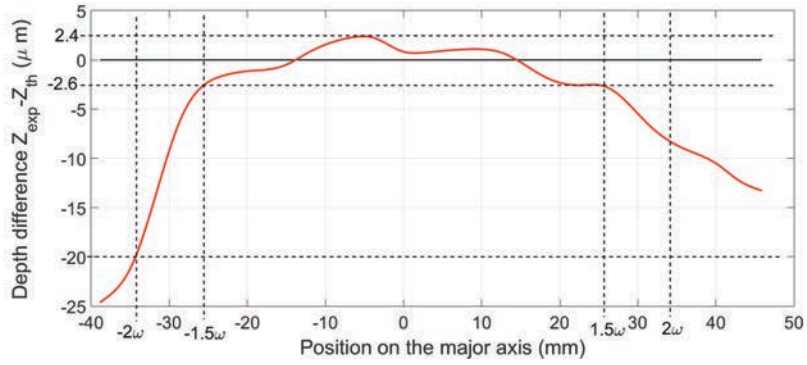

FIGURE 4.16: Shape difference between the manufactured MLO and the theoretical design

The shape difference $Zexp - Z_{th}$ is quite small at the center of the mirror and increases near the edges. The radius of the Gaussian beam received by the MLO is $\omega = 12.1$ mm, as calculated in section 4.4.1. As the angle between the mirror and the beam is 45°, the radius projected on the major axis of the MLO is $12.1 \times \sqrt{2} = 17.1$ mm. As explained in section 4.2.3.2, 98.90 % of the beam power is included in a circle with a radius of 1.5ω (25.6 mm), and 99.97 % of the power is included in a circle with a radius of 2ω (34.2 mm). So, most of the beam (98.9 %) will be reflected by the center of the mirror, where the shape difference is smaller than 5 µm. As a result, the mirror is in accordance with our requirements in terms of roughness and shape accuracy.

4.5.2 The polarizing grids

The wires grids of the MPI, G1 and G2, are very important because they must efficiently separate two polarizations of the signal. The part of the signal whose polarization is parallel to the wires is reflected, while the part of the signal whose polarization is perpendicular to

its wires is transmitted. Our two wire grids are made with tungsten wires and were manufactured by the university of Erlangen. They have an internal diameter of 52 mm (which is larger than 5ω at that position) and should have the dimensions calculated in section 4.4.2: Wires with a diameter $a = 10$ μm and a wire spacing $g = 35$ μm. We first observed the grids with a scanning electron microscope (SEM), to know their real dimensions. Then, I tested them to characterize their efficiency.

4.5.2.1 Observation with a scanning electron microscope

With the SEM observation, we were able to determine that the diameter of the grids' wires is $a = 10.0$ μm (figure 4.17) and the average spacing is $g = 36.7$ μm (figure 4.18).

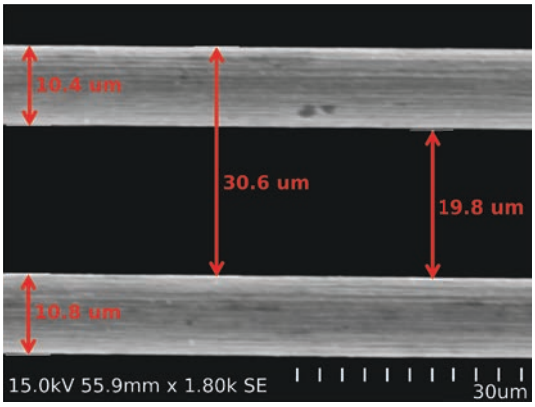

FIGURE 4.17: Thickness of the grids' wires

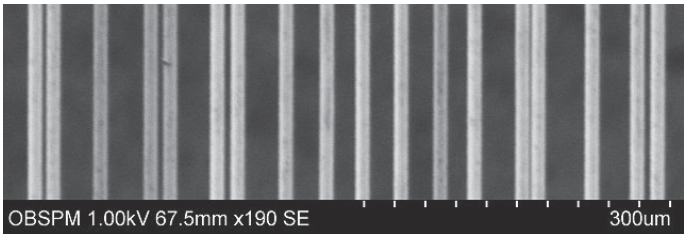

FIGURE 4.18: Spacing of the grids' wires

The wire grids have the expected diameter ($a = 10$ μm), but the average wire spacing is a bit larger than expected (37 μm instead of 35 μm). We can also see in figure 4.18 that the wire spacing is quite irregular. This can be problematic as the spacing irregularities can affect the grids' efficiency.

4.5.2.2 Effects of the irregular wire spacing on the polarizing efficiency

As the spacing irregularities can reduce the efficiency of the polarizing grids, it is useful to know the relation between the grid's efficiency and the wire spacing deviation.

Beunen et al. [45] measured the standard deviation σ of their grids' wire spacing (with 10 μm diameter wires). They found that this deviation σ is usually between 9 μm and 10 μm, and it tends to increase when the wire spacing decreases. With the SEM, we measured the standard deviation of our MPI grid (with a small sample of 30 wires) and found $\sigma = 9.8$ μm. This value is consistent with this paper and indicates that the spacing irregularities of our MPI grids correspond to the normal manufacturing error of free standing wire grids.

Shapiro and Bloemhof [46] measured the effect of the standard deviation on the grid's efficiency. They considered the ratio σ/g and showed that $T_{//}$ increases along with σ/g. Their study was carried out at lower frequencies (up to 490 GHz) and for 25 μm diameter wires. Shapiro et al. showed that between a very regular spacing ($\sigma/g = 0.07$) and a more irregular spacing ($\sigma/g = 0.23$), $T_{//}$ increases by approximately 100 %. This relation is expected to scale with wavelength, so we can apply this study to our grids at 2.6 THz. For our MPI grids, I calculated $\sigma/g = 9.8/37 = 0.26$. So, we can expect the value of $T_{//}$ to be about 110 % higher than the parallel transmittance of an ideally spaced grid.

$$T_{//irreg} = T_{//ideal} + T_{//ideal} \times 110\,\% = 2.1 \times T_{//ideal}. \tag{4.20}$$

4.5.2.3 Testing of the polarizing wire grids

The testing of the grids can enable us to characterize their polarizing efficiency and deduce expected losses for the MPI. I used the 2.6 THz LO to generate the signal. A polarizing grid was used to remove the cross polarization of the LO (which was measured to be about 6 %) and the ellipsoidal mirror MLO was used to focus the signal. The detector I used is an infrared bolometer cooled down to 4.2K which is very accurate (with an accuracy of a few nW). I also needed to chop the signal with a shutter as the bolometer can only measure a pulsed signal. I put the MPI grid I wanted to characterize between the bolometer and the polarizing grid. The schematic of this experiment is shown in figure 4.19. The polarizing

grid is set to only select the main polarization of the LO (which is vertical). By measuring the power received by the IR bolometer for when the wires of the MPI grid were horizontal and vertical (with respect to the MPI support), I was able to deduce $T_{//}$ and $T_{\perp}$. I characterized the MPI grids for a normal incidence (90°) and for a 45° incidence (as it is in the MPI). The results of this experiment are:

$$\text{Normal incidence:} \quad T_{\perp} = 95 \pm 1\ \% \quad \text{and} \quad T_{//} = 3 \pm 1\ \%$$

$$45° \text{ incidence:} \quad T_{\perp} = 95 \pm 1\ \% \quad \text{and} \quad T_{//} = 2 \pm 1\ \%$$

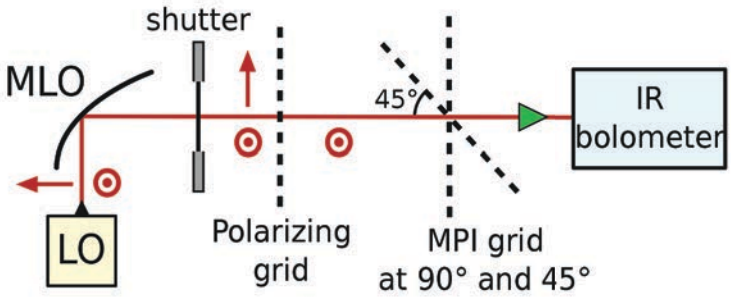

FIGURE 4.19: Schematic of the experiment set up to characterize the MPI grid

The incertainty of these measurements (±1 %) is mostly due to the slow drift of the LO power during the test, and to the air absorbance. The optical path is quite long (about 50 cm) and the water vapor in the air absorbs between 20 % and 40 % of the signal's total power at 2.6 THz (cf. section 4.5.4). So, air draughts can also create some power changes.

4.5.2.4 Conclusion

Table 4.2 shows the measured and simulated (cf. section 4.4.2) efficiency values for our MPI grids at 2.6 THz. The theoretical values of $T_{//}$ and $T_{\perp}$, for a normal incidence and a 45° angle incidence, are calculated in section 4.4.2.4. I also took into account the theoretical effects of the irregular wire spacing on $T_{//}$, which are described in section 4.5.2.2. At 2.6 THz, the irregular wire spacing produces an increase of 110 % of $T_{//}$, which corresponds to a multiplication by a factor 2.1. The experimental values of $T_{//}$ and $T_{\perp}$, for a normal and a 45° angle incidence, are presented in section 4.5.2.3. The absorbance of the metal wires is expected to be very low (1 % or less) for the transmitted signal, so it has not been taken into account in this calculation (cf. section 4.4.2.1).

	Theoretical transmittance (%)	Measured transmittance (%)
$T_{//}(0°)$	$0.9 \times 2.1 = 1.9$	3 ± 1
$T_{\perp}(0°)$	97	95 ± 1
$T_{//}(45°)$	$0.6 \times 2.1 = 1.3$	2 ± 1
$T_{\perp}(45°)$	95	95 ± 1

TABLE 4.2: Synthesis of the grids' theoretical and measured transmittances

Finally, as shown by Table 4.2, the measured and simulated results are very close. It suggests that the theoretical analysis of the grid, based on the theoretical equations from Blanco et al. [43], the 45° incidence angle consideration, and the effects of the irregular spacing, is quite accurate.

4.5.3 Efficiency of the roof-top mirrors

The roof-top mirrors are made of two flat orthogonal faces. As it is quite easy to machine flat faces, we do not have any doubt concerning the surface roughness of these mirrors (they are almost optically polished). However, an uncertainty arises concerning the roof line (the junction of the two faces). The beam reaching a roof-top mirror must be reflected twice so its polarization can be inverted. If a portion of the beam reaches the roof line, it can either be reflected once, or twice but in a wrong direction (because the flat faces are slightly curved near the roof-line). So, the rays reflected by the roof-line can be considered as lost. I measured a 15 % efficiency improvement in our MPI when the roof-top mirrors were not centered on the incoming beam (so the roof line was not illuminated). Consequently, in our MPI I made sure that the incoming beam was reaching a face of the roof-top mirrors, and not the roof line.

4.5.4 Air absorbance

The water vapor contained in the air absorbs some parts of the spectrum. It is important to know the transmittance spectrum of the air to avoid using the frequencies where the air is very absorbent. Moreover, because the air becomes quite absorbent for frequencies above 1 THz, a heterodyne receiver observing above 1 THz would need to operate from a high altitude (plane, stratospheric balloon, satellite). At these altitudes, the MPI can be considered to be in a vacuum and does not suffer any water vapor losses. So, to know the

efficiency of our MPI (and possibly compare it with the efficiency of a beam splitter), we need to remove the air absorbance from the results.

4.5.4.1 Calculation of the precipitable water vapor (pwv)

I used the software *am* (atmospheric model) developed by Scott Paine [47] to calculate the theoretical air transmittance in our lab. The absorbance of the air depends on the precipitable water vapor (pwv) contained in the given path length. This parameter is calculated from the relative humidity (RH), the temperature of the air (T) and the considered path length (L). This calculation is described in appendix B.3. Finally, I obtain the final formula giving the pwv (in mm) as a function of L, T, and RH. With T, in Kelvins, RH in % and L in meters.

$$pwv(RH, L, T) = 1.323 \times \frac{RH.L}{T} \times \exp\left(\frac{17.67(T-273.15)}{T-29.65}\right) \tag{4.21}$$

For an optical path length of 50 cm, an average temperature of 25 °C and an average relative humidity of 30 %, I plotted the transmittance spectrum of the atmosphere from 100 GHz to 3 THz (figure 4.20). The values of temperature and relative humidity were chosen because the correspond to the average values we measured in our lab, and the length of the optical path approximately corresponds to the length of the MPI's optical path.

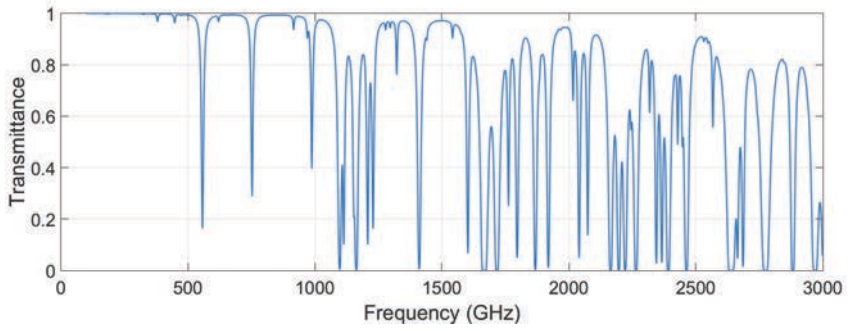

FIGURE 4.20: Atmospheric transmittance for a 50 cm optical path, 30 % of relative humidity and a temperature of 25 °C

4.5.4.2 Theoretical evaluation of the air absorbance in our MPI

In the case of our MPI, the path length (L = 0.5 m) is fixed, but T and RH change over time. In winter, the outside temperature decreases and RH increases, and in summer it is the contrary. These changes induce a variation of the pwv contained in the air. Along the year, the pwv in our lab (and outside) globally varies between 2 µm and 6 µm, which is well represented on the plot, figure 4.21. At 2.6 THz, for a 50 cm optical path, the theoretical transmittance of the air lies between 83 % when pwv = 2.3 µm and 61 % when pwv = 5.8 µm.

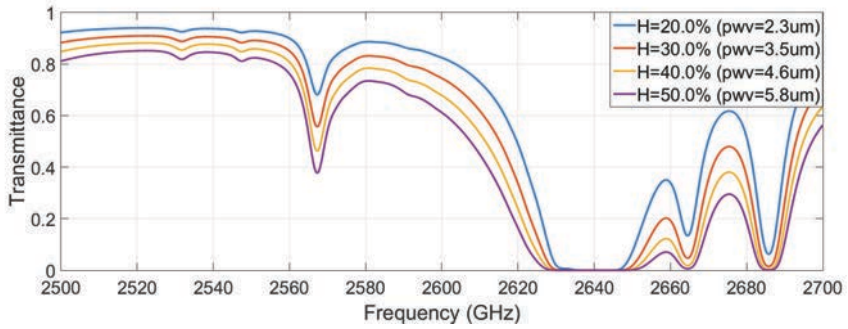

FIGURE 4.21: Atmospheric transmittance for a 50 cm optical path at 25 °C

4.5.4.3 Conclusion

This simulation shows the strong absorption of water vapor in air at THz frequencies and the important variations of this absorption with temperature and relative humidity. Finally, the easiest solution to remove the air absorbance from the MPI's transmittance is to compare the beams produced by the ellipsoidal mirror (MLO) with and without the MPI. To have the same size, both beams have to be measured at the same distance (L = 50 cm) from the MLO. The beam going through the MPI is attenuated by the air and the MPI, while the other beam is only attenuated by the air. By subtracting the intensity of both beams, I am able to accurately determine the real transmittance of the MPI, without the air absorbance.

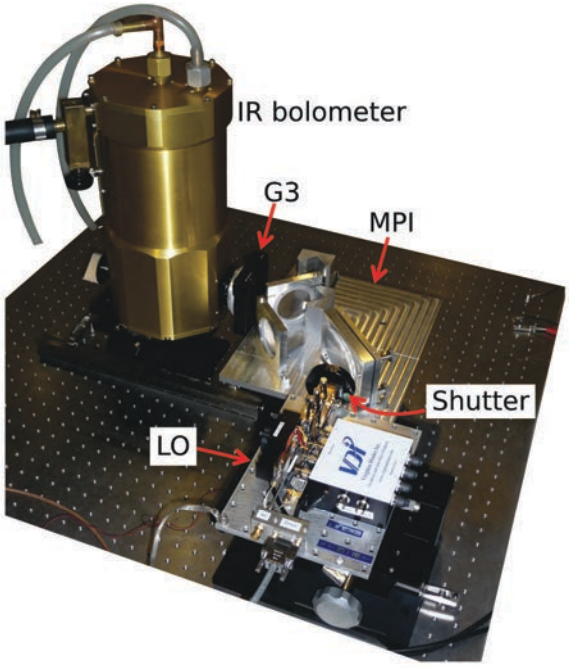

FIGURE 4.22: Set-up of the experiment to measure the efficiency of the whole MPI

4.6 Efficiency of the whole MPI

4.6.1 Presentation of the experiment

After having tested each component of the MPI individually, I tested the whole MPI. Extreme care was taken to align the different elements because I measured that, at 2.6 THz, an inclination angle as small as 0.1° of the mirrors could induce a few % losses at the output of the MPI. I used a 2.6 THz LO source from VDI (Virginia Diodes Inc.) which emits approximately 2 μW. The signal emitted by the LO is mainly vertically polarized but also contains 6 % of horizontally polarized signal (we call it cross-polarization). A very sensitive cryogenic bolometer from IRLabs was used to measure the power of the LO signal after different elements of the MPI. A grid, called G3, fixed on a rotating support was also used to select the vertical or horizontal polarizations of the signal, and remove the cross-polarization. The experiment's set-up is shown in figure 4.22.

4.6.2 Different steps of the experiment

During the experiment, I added the different elements of the MPI one by one, and measured the received power at different steps of the assembly. This allowed me to discriminate the losses due to each element. The different assembly steps are shown in figure 4.23.

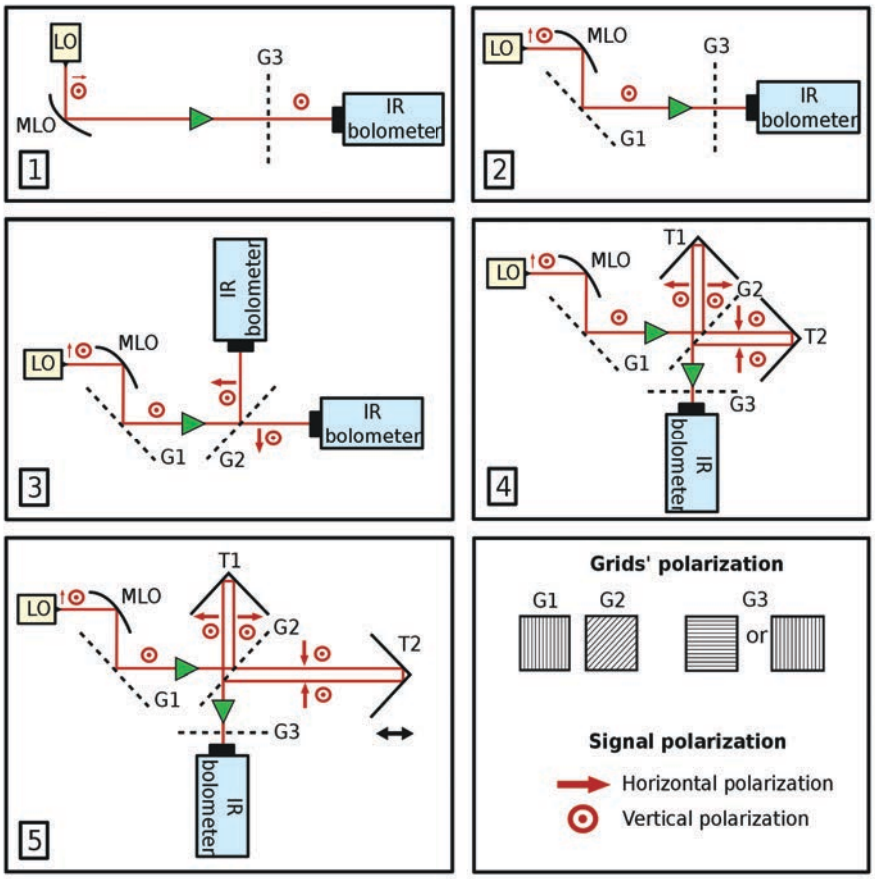

FIGURE 4.23: Consecutive steps of the MPI assembly

I always measured the power at the same distance from the ellipsoidal mirror MLO, to measure the same beam size and have comparable results. The distance between the MLO and the bolometer was set to 43.5 cm because it approximately corresponds to the position of the beam waist. The IR bolometer is very accurate, and I estimate an accuracy of ±1 % for my power measurements, due to the positioning of the bolometer, the air fluctuations, and the possible drift of the LO power.

4.6.2.1 Step 1: Signal reflected by the MLO

I reflected the LO signal with the ellipsoidal mirror MLO and used the grid G3 to only transmit the vertical polarization to the bolometer (figure 4.23-1). The power measured is the reference and it will be used to calculate the efficiency of the MPI.

4.6.2.2 Step 2: Signal reflected by G1

Grid G1 has vertical wires which reflect most of the vertical polarization and transmit most of the horizontal polarization (figure 4.23-2). I measured that 91.5 ± 1 % of the vertically polarized signal was reflected by G1 ($R_{//} = 91.5 \pm 1$ %). According to section 4.5.2.3, $T_{//} = 2 \pm 1$ %, so in the absence of losses, we should have $R_{//} = 98 \pm 1$ %. So, approximately 6 % of the power is missing, and it could be caused by the absorbance of the grid's wires. When I measured the transmittance of the grids, I assumed that the absorbance was inferior or equal to 1 %. However, in reflection the field is mostly parallel to the wires and the current induced in the grid's wires is much stronger, so the absorbance losses are expected to be higher, especially at high frequencies. As we found no articles describing the absorbance losses of polarizing grids at high THz frequencies, we are intending to characterize this effect in the near future.

• The losses due to G1 are $L2 = 8.5 \pm 1$ %.

4.6.2.3 Step 3: Signal reflected and transmitted by G2

I added the grid G2 with a polarizing angle of 45° (figure 4.23-3). The power transmitted by G2 was 49 ± 1 % and the power reflected was 47 ± 1 %, compared to the signal measured in the previous step. According to section 4.5.2.3, the measured transmittance of grid G2 is $T_{\perp} = 95 \pm 1$ % and $T_{//} = 2 \pm 1$ %. So, without any absorbance, and for a perfect polarizing angle of 45°, the transmitted power should be $95/2 + 2/2 = 48.5 \pm 1$ %, and the reflected power, $98/2 + 5/2 = 51.5 \pm 1$ %. The difference between the predicted and the measured reflectance of the grid G2 is certainly be due to the wires' absorbance and/or to a small error in the polarizing angle of the grid. It corresponds to 4 ± 2 % losses.

• The losses due to G2 at the output of the MPI are expected to be $L3 = 2 \times 4 \pm 2$ % (the signals meet the grid G2 twice).

4.6.2.4 Step 4: Signal reflected by T1 and T2

I measured the power at the output of the MPI with both roof-top mirrors at the same distance of 5 cm from G2 (figure 4.23-4). The measured losses of G2 and the two roof-top mirrors are equal to 8 ± 1 % (compared to the signal measured in step 2). It corresponds to the estimated losses L3 of grid G2 alone, so we can deduce that the roof-top mirrors' losses are negligible.

By translating the mirror T2 (along the beam's direction), the polarization of the signal at the output of the MPI is changed (between horizontal, elliptic and vertical polarizations). We need to get a linearly polarized signal (vertical or horizontal) at the output of the MPI. So, I used G3 to, successively, select these two polarizations and I adjusted T2 to get the maximum power. I achieved the same efficiency for both polarizations and had only 2 % cross-polarization losses.

• The losses due to T1 and T2 are negligible and there is a 2 % cross polarization at the output of the MPI, for the vertical and horizontal polarizations. It also confirms the losses of grid G2: $L3 = 8 \pm 1$ %

4.6.2.5 Step 5: Signal at the output of the MPI

Finally, I moved T2 further from G2 to finalize the MPI assembly (figure 4.23-5). T2 was positioned at 10 cm from G2 while T1 stayed at a distance of 5 cm from G2. I measured the power at the output of the MPI, with and without G3. I measured an additional power loss of 3 ± 1 % and an additional cross polarization of 3 ± 1 %, compared to step 4.

An explanation for the total power loss is the air absorbance. The path of the beam reaching T2 was increased by 10 cm. By using the software *am* from Paine [47] (cf. section 4.5.4), I calculated that this path increase corresponds to an additional air absorbance of 5 % of the considered beam. It represents a reduction of 2.5 % of the total power at the output of the MPI, which is consistent with my measurement. The increase of the cross polarization is caused by two effects. The air absorbance has weakened the signal coming from T2, so the coupling with the signal coming from T1 is not as efficient as before because the amplitudes of the signals from the two MPI sidearms recombine with different levels. Moreover, when

the two beams recombine after G2, they now have a different size (because of the path difference), making the coupling even less efficient.

• The losses due to the air absorbance are $L5 = 3 \pm 1$ %, and the increase of the cross polarization at the output of the MPI is 3 ± 1 %.

4.6.3 Conclusion

Finally, by comparing the measured beam power at the input (cf. step 1), and at the output (cf. step 5) of the MPI, I calculated a total power transmittance of 81 ± 1 % and a polarized transmittance of 76 ± 1 %. It corresponds well to the total power and polarized transmittances obtained by considering the losses of all the individual elements measured from step 2 to step 5:

$$T_{Tot\ power} = (1 - L2) \times (1 - L3) \times (1 - L5) = 82 \pm 2\ \%. \tag{4.22}$$

$$T_{Polarized} = T_{Tot\ power} \times (1 - 0.05) = 78 \pm 2\ \%. \tag{4.23}$$

Where $L2 = 8.5 \pm 1$ %, $L3 = 8.0 \pm 1$ % and $L3 = 3.0 \pm 1$ %.

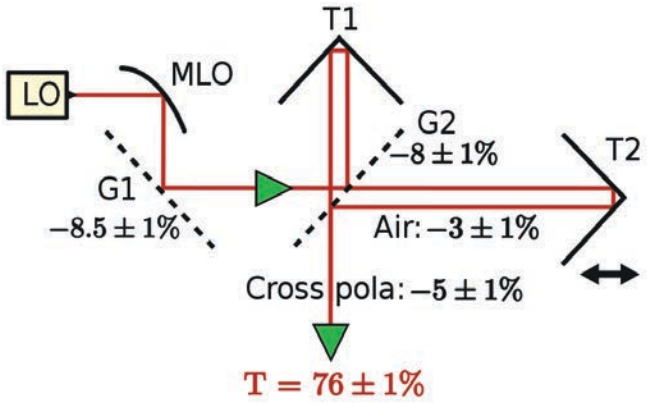

FIGURE 4.24: Schematic showing the losses of the different elements of the MPI

The losses of the different elements of the MPI are gathered in figure 4.24. As the RF signal is transmitted by the grid G1, and not reflected, there will be less losses. So, the expected efficiency of the MPI for the RF signal is 84 % for the total power and 79 % for the polarizing

efficiency. These results are quite good, especially at 2.6 THz where the alignment is very critical.

4.7 Conclusion

Usually, a beam splitter is used to superimpose the LO and RF signals before they reach the mixer of a heterodyne receiver. However, this technique requires lots of LO power and our 2.6 THz LO does not emit enough power to correctly pump our HEB mixer after having been reflected by a beam splitter. That is why we decided to build a Martin Puplett interferometer (MPI), which can superimpose both RF and LO signals with theoretically very little losses. The mixer needs to receive the LO and RF signals superimposed and with the same polarization. The superposition of the LO and RF signals is done by a first polarizing wire grid. Then, the rotation of the polarization of only one of the two signals is done by the MPI, composed of a second polarizing wire grid and two roof-top mirrors. Our MPI also used an ellipsoidal mirror to focus the LO beam. The design of this mirror was based on Gaussian beam optics equations, which were presented in the first part of this chapter. The polarizing wire grids are crucial elements of an MPI and their characteristics have an important impact on the efficiency of the MPI. A theoretical model enabled me to determine the required characteristics for our grids at 2.6 THz. Then, the testing of the grids allowed me to confirm the theoretical model, as the measured characteristics of the grids were close to the calculated ones. After evaluating all the components of the MPI individually, I finally assembled them to set up the MPI. The test of the MPI suggested that at 2.6 THz, the absorbance of polarizing grids with 10 μm diameter tungsten wires is not negligible, unlike what is usually assumed at lower frequencies. Finally, our MPI was able to transmit the LO beam with 76 % efficiency in the required polarization, and should, simultaneously, transmit the RF signal with an efficiency close to 79 %. These results are good, especially at 2.6 THz where the alignment of the components is extremely critical. As a result, this MPI is operational and efficient enough to be used as a diplexer in our 2.6 THz heterodyne receiver. In the future, the replacement of the polarizing grids by more efficient ones will allow us to increase the efficiency of the MPI.

Chapter 5

Phase gratings

5.1 Background and theory

5.1.1 Motivation

Early THz heterodyne systems concentrated on high spectral resolution and large bandwidth (with many spectral channels), but they usually only had one spatial pixel (i.e. HIFI instrument on Herschel satellite [8]). Recently, arrays of heterodyne receivers have been developed to simultaneously measure spectra at several positions in the sky. In heterodyne receivers, each pixel has a mixer. So, observing with several pixels involves pumping all these mixers with an LO. The most efficient way of doing it is to split the LO beam into several beams to specifically illuminate each mixer. Phase gratings are the perfect tool for achieving this goal.

In this chapter, I start by presenting the different kinds of existing phase gratings for THz frequencies: stepped gratings and Fourier gratings. Then, I describe a more general approach I developed in order to design any kind of phase grating. We called the gratings created with this new approach *Global gratings*. In the last part of the chapter, I describe the design, simulation, manufacturing, and testing processes which enabled me to make two Global grating prototypes.

5.1.2 Presentation of the phase gratings

A phase grating is an element which locally changes the phase of an incoming beam. In the case of a transmissive element (lens), the variation of its thickness creates a proportional phase variation within the beam. In the case of a reflective element (mirror), the depth variations of the illuminated surface generate the same proportional phase variations. As a result, the different parts of the incoming beam which have been phase shifted interfere, and the constructive interferences generate new beams. That is why phase gratings can be used to divide the incoming LO beam into several output beams, as shown on figure 5.1.

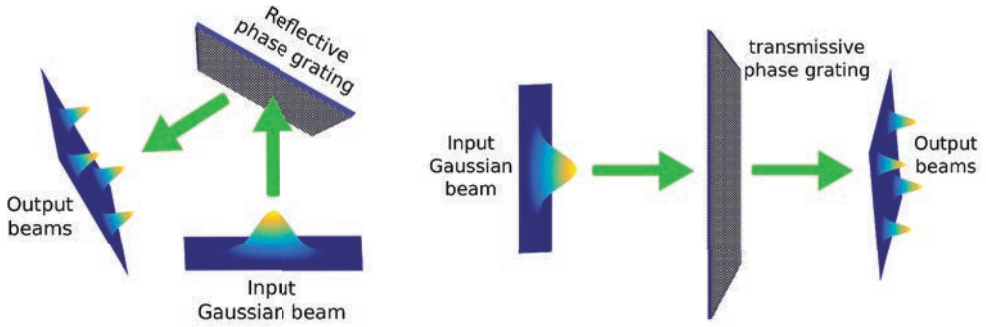

FIGURE 5.1: Reflective and transmissive phase gratings

Several heterodyne receivers already use phase gratings to observe with several pixels, such as CHAMP [48] (since 1998), SMART [49] (since 2001), Desert STAR [50] (since 2003), upGREAT [11] (since 2015).

5.2 The stepped phase gratings

5.2.1 Overview of the stepped phase gratings

The Dammann grating is a two dimensional array of identical rectangular cells. It is only composed of one level steps, as illustrated by figure 5.2, while multilevel gratings are made of multiple level steps. The latter are more complicated to design and to manufacture but can achieve higher efficiencies. The stepped grating concept can be applied to transmissive or reflective materials, so it is possible to make stepped lenses or mirrors. Stepped phase gratings have been used as LO multiplexers in several radio telescopes. The CHAMP instrument uses two stepped phase gratings to feed 2x8 mixers with two LOs, at frequencies

around 500 GHz (cf. Güsten et al. [48]). The Dammann grating (DG) is the simplest stepped phase grating, and has been first designed and created in 1977 by Dammann and Klotz [51].

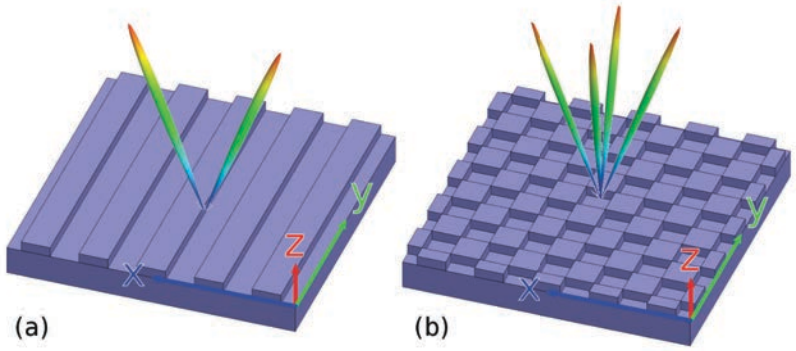

FIGURE 5.2: Examples of Dammann grating designs, splitting the input beam into 2 beams (a), and 4 beams (b)

A typical set-up for a multi-beam generation by a phase grating is shown on figure 5.3. The first lens is used to focus the diverging beam emitted by the LO. The DG is positioned at the minimum waist position of the first lens, where the Gaussian beam has a planar wavefront. As the refractive index of the DG is higher than the air's index, the part of the beam going through the steps is phase shifted compared to the part of the beam going through the grooves. It induces a phase modulation within the beam, which creates destructive and constructive interferences. Then the resulting radiation pattern can be observed in the output focal plane of the second lens. Multistep gratings work like Dammann gratings, but several phase shifts can be introduced to increase the efficiency.

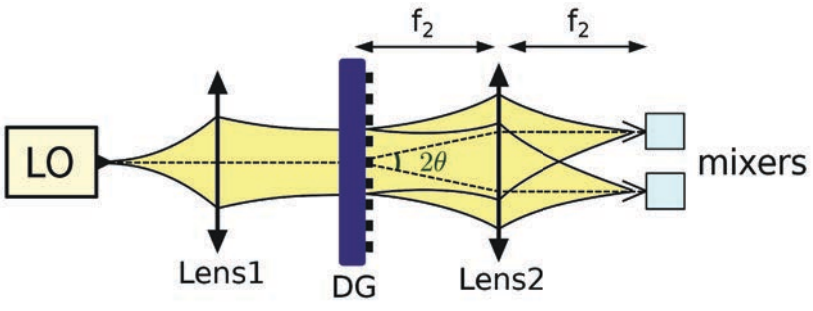

FIGURE 5.3: Optical setup of a phase grating

5.2.2 Theory of Dammann gratings

The electromagnetic wave propagation is defined by Maxwell's equations. However, under several conditions listed in appendix C.1, we can approximate Maxwell's equations with a Fourier transform to calculate the far-field generated by a surface field distribution within a given aperture (here the phase grating).

The theory of Dammann gratings (DG) has been described by several authors, such as Mait et al. [52], O'Shea et al. [53] and, of course, Dammann and Klotz [51]. The theoretical calculation of the far-field produced by a DG is briefly presented below, and described in appendix C.2. We consider the case of a transmissive one-dimensional DG, only composed of periodic grooves, as in figure 5.2a. The period of the DG has been normalized to $\Delta u = 1$, where u is the position on the grating profile. The DG is a binary grating which implies a phase step difference of π, so its transmission is $T(u) = \pm 1$. In the case of periodic gratings, the diffraction pattern is discrete and composed of beams of several beams emitted at specific angles. These angles are calculated with the grating's equation:

$$n\lambda = \Delta u.sin(\theta_n), \tag{5.1}$$

where $n \in \mathbb{Z}$ is the considered diffractive order, Δu is the real spatial period of the grating (not normalized), and θ_n is the angle between an n-order beam's direction and the normal of the grating, as illustrated in figure 5.4.

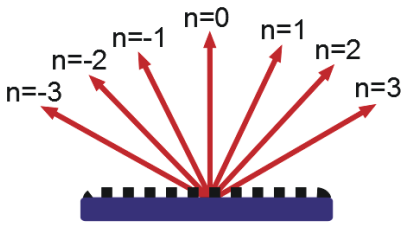

FIGURE 5.4: Output beams of all possible diffraction orders

In practice, the diffracted beam's order is not infinite as it is limited with respect to the angular range [-90°, 90°]. So, the real diffracted orders produced by the grating are:

$$n = \pm \left\lfloor \frac{\Delta u.sin(\theta_n)}{\lambda} \right\rfloor, \tag{5.2}$$

where $\theta_n \in$ [-90°, 90°] and $\lfloor\ \rfloor$ is the *floor()* function.

5.2.3 Test of a transmissive Dammann grating

We bought a DG from the company Tydex Optics (figure 5.5). This grating is made of high resistivity float zone silicon (HRFZ-Si) and it works in transmission. This grating was designed to generate 2 beams separated by an angle $2\theta = 40°$ at a frequency of 1.39 THz. The frequency of 1.39 THz rather than 2.6 THz was chosen because the LO power at 2.6 THz is too little to allow accurate tests. Moreover, it has a parylene anti-reflective coating on both faces, to reduce the losses.

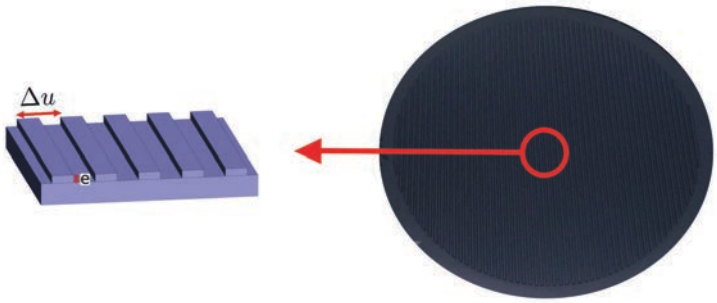

FIGURE 5.5: HRFZ Silicon Dammann grating from Tydex optics

5.2.3.1 Theoretical dimensions of the Dammann grating

This grating is made for a frequency of 1.39 THz ($\lambda = 216$ µm). According to the gratings' equation 5.1, an angle $2\theta = 40°$ between the output beams corresponds to a spatial period of:

$$\Delta u = \frac{\lambda}{sin\theta} = 632 \text{ µm}. \tag{5.3}$$

So the grooves and steps should both have a spatial period of 632 µm. The steps must produce a path difference of $\lambda/2$ in order to create a phase shift of π rad. So, the height of the steps, e, must satisfy the equation:

$$e \times (n_{Si} - n_{air}) = \frac{\lambda}{2}, \tag{5.4}$$

$$\text{and,} \qquad e = 44.7\ \mu\text{m}, \tag{5.5}$$

where $n_{Si} = 3.417$ is the refractive index of the HRFZ Silicon, and $n_{air} = 1$. The diffraction pattern of a 2 beam DG is investigated in more detail in appendix C.3. Equations 5.3 and 5.5 predict that a HRFZ Silicon DG producing 2 beams at -20° and +20° angles should have 44.7 µm high steps replicated with a period of 632 µm.

5.2.3.2 Measurement of the Dammann grating's dimensions

We inspected the bought HRFZ Si Dammann grating by measuring it with a profilometer (Dektak 8) and a scanning electron microscope. It enabled me to compare its real dimensions with the theoretical ones, predicted by equations 5.3 and 5.5.

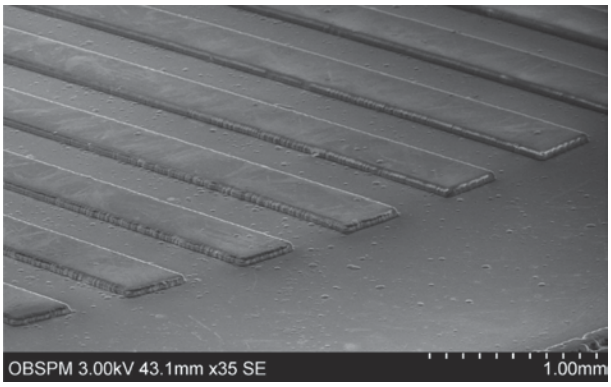

FIGURE 5.6: The Dammann grating edge viewed with a SEM

The picture from the SEM (figure 5.6) distinctly shows the steps of the grating covered by the anti-reflective coating.

The profilometer has a resolution better than 1 µm and gives very detailed measurements of the grating's profile (figure 5.7). I measured a height of $e_{exp} = 45$ µm and a spatial period of $\Delta_{exp} = 620$ µm. These values are very close to the theoretical ones I calculated previously ($e_{th} = 44.7$ µm and $\Delta u_{th} = 632$ µm).

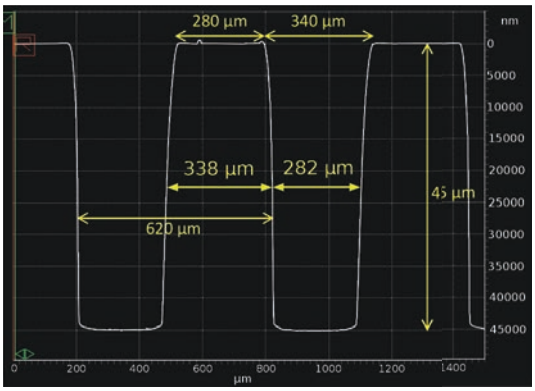

FIGURE 5.7: The grating's surface measured with a profilometer

5.2.3.3 Measurement of the Dammann grating's efficiency

I used a 1.39 THz source from the company Virginia Diodes Inc. (VDI) which has a maximum output power of 40 µW. I mounted the LO, a shutter (to modulate the signal), a lens, and the DG on a rotating support (figures 5.8 and 5.9). In front of the support, a static Golay cell power meter was used to measure the received power. By rotating the support, I was able to characterize the shape of the output beams in the horizontal plane.

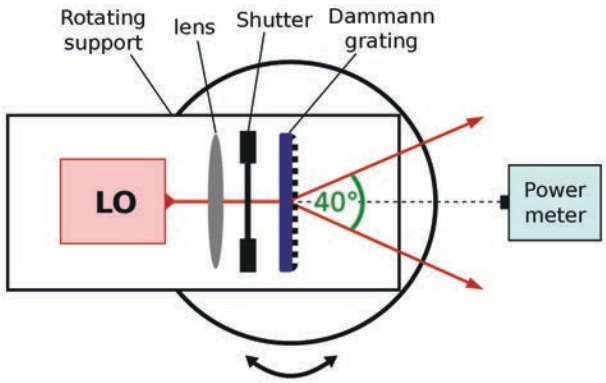

FIGURE 5.8: Schematic of the experiment to test the DG

Figure 5.10 shows the profile of the beams produced by Tydex' Dammann grating. The angle between the two beams is $40 \pm 1°$, as expected, and the maximum intensity of the beams corresponds to 33 ± 2 % and 32 ± 2 % of the input beam's intensity. The shape of the output beams has been measured and it is very close to the shape of the input beam. The accuracy of ±2 % is due to the optical alignment of the Dammann grating, the power drift of the LO with time, and the accuracy of our Golay cell power meter. We can conclude that this transmissive DG works as expected. The angles and the shape of the two output beams

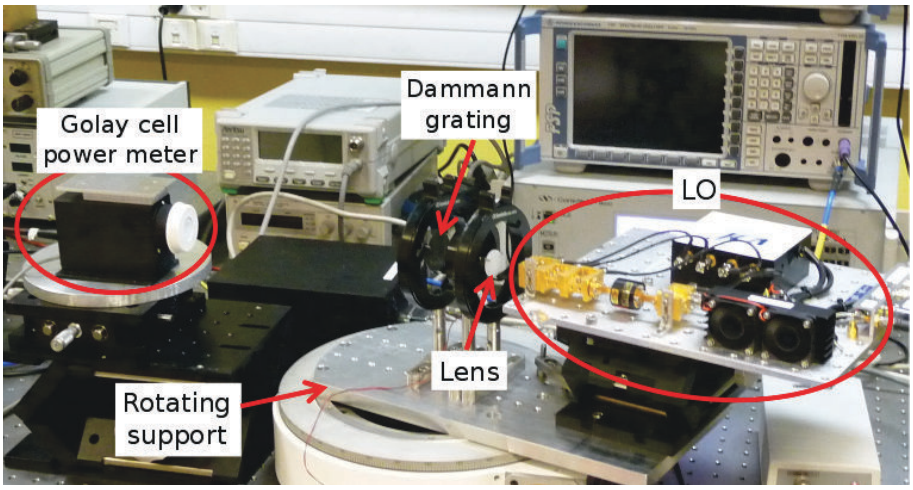

FIGURE 5.9: Picture of the experiment to test the DG

correspond to the predicted angles, only the total efficiency of this DG with 65 ± 2 % is less than the 100 % theoretically expected (cf. appendix C.3).

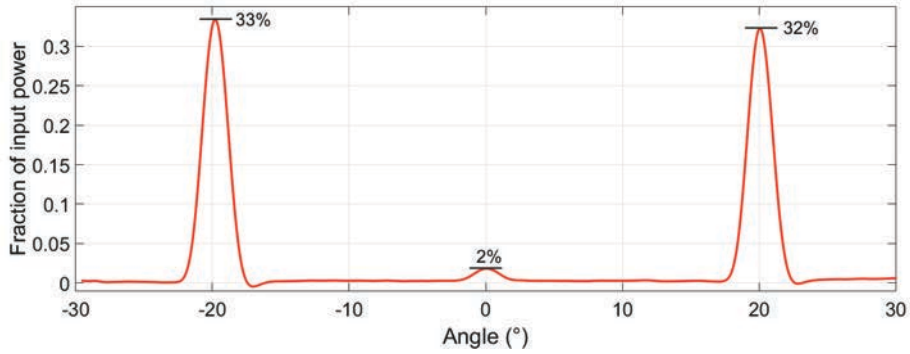

FIGURE 5.10: Angle and power of the output beams

Several factors can make the real efficiency of the DG differs from its theoretical efficiency:

- Even with an anti-reflective coating, about 10 %-15 % of the input signal is reflected by the surfaces of the grating, lost, or produces unpredictable multi-reflections inside the grating (see section 5.5.4.3 for more details).
- The geometry of the grating is not perfect. Dimensional defaults can favor unwanted orders like the beam at 0° which contains 2 % of the input power.
- Several parameters such as scattering, diffraction, absorption and shadowing are not taken into account by the theory using the Fourier transform, and can further reduce

the efficiency of the grating. More complete and accurate theoretical results are obtained with electromagnetic simulations, as described in section 5.4.4.

5.3 The Fourier grating

The Fourier grating is a kind of phase grating which was first developed in 2001 by Graf and Heyminck [54] [55]. It works as any other phase grating, but, unlike stepped gratings, it is smooth, produces a continuous phase modulation and can usually reach a higher efficiency than stepped gratings. The phase structure of Fourier gratings is designed by using finite Fourier series, with about 13 coefficients per spatial dimension. The coefficients are calculated with a random search followed by an optimization process. Fourier gratings, being smooth, are like stepped gratings with an infinite number of steps, which is a real improvement. However, as they are generated by Fourier series, they are limited by the possibilities of Fourier series. Fourier gratings cannot have sharp edges and must be periodic. Fourier gratings have been mostly used in reflection and manufactured as Fourier mirrors. A useful improvement, made by Heyminck et al. [55], has been to combine Fourier mirrors and focusing mirrors (ellipsoidal or parabolic). It enabled them to remove the focusing element between the LO and the Fourier grating, which contributed to a small reduction of the losses and an easier alignment of the quasi-optical elements. Fourier gratings have been used in several heterodyne receivers:

- The SMART instrument [49], embedded on KOSMA telescope, consists of two 2x4 pixel sub-arrays, operating at two different frequencies (490 GHz and 810 GHz).
- The upGREAT instrument [11], embedded on SOFIA [12] airplane, has two 7 pixel arrays operating between 1.9 and 2.5 THz, and one 7 pixel array at 4.745 THz.
- The Desert STAR instrument [50] on the Heinrich Hertz telescope (HHT) [56] has 7 pixels operating at 345 GHz.

5.4 The Global phase grating

5.4.1 General presentation

I have developed a general kind of phase grating, not restricted to discrete steps or Fourier series. This phase grating can be non-periodic, have sharp edges, be completely smooth or be stepped, and has no design constraints. It includes all kinds of phase grating design, including Fourier and Dammann gratings. We call it *Global phase grating*. As it has more possibilities than Fourier and Dammann gratings, it can usually reach a higher efficiency and it can produce any kind of far-field pattern. As it can be non-periodic, it can also be adapted to the shape (intensity and phase profiles) of the incoming beam. This feature could be useful if we design a grating whose cells' size is close to the beam size. The challenges of the Global phase grating, compared to Fourier and Dammann gratings, are the required computing power for the design, and the manufacturing process. Global gratings can have any shape, be partly continuous and partly discrete for example. This diversity of shapes can be difficult to manufacture. The shape of Global gratings is not represented by a mathematical function, like the Rectangle function for Dammann gratings or the Fourier series for Fourier gratings.

5.4.2 Numerical calculation

5.4.2.1 Architecture of the main program

The numerical program I developed to calculate Global phase gratings' profiles runs on Matlab. It takes advantage of the numerous Matlab built-in functions and uses Matlab's parallel processing feature to increase the calculation speed. To design the grating, I start from the desired far-field beam pattern and use a method based on the far-field to near-field transformation. The steps performed by the program are listed below and described in figure 5.11.

1. The desired radiation pattern is chosen by the user and it is composed of several Gaussian beams positioned at the desired positions. Once it has been defined, the far-field radiation pattern is mapped onto the aperture field of the grating via an inverse FFT.
2. The physical realization constraints are imposed (i.e. the finite size of the grating).

3. The size of the input Gaussian beam used by the program corresponds to the size of our LO beam once it has been collimated by a focusing element (lens or mirror). This Gaussian beam is mapped onto the the aperture field of the grating via a FFT.

4. The phase profile of the Global phase grating is calculated as the difference between the phase front of the incoming Gaussian beam and the phase profile required to generate the desired far-field pattern. The resulting phase profile is coupled to the Gaussian amplitude profile of the incoming beam. The result corresponds to the aperture field distribution produced by the grating.

5. An FFT is used to calculate the far-field pattern generated by this aperture field when illuminated by the LO Gaussian beam.

6. The constraints on the output radiation pattern are imposed (shape of the beam, side lobe level, etc.). The radiation pattern is compared to the desired radiation pattern to calculate the efficiency of the phase profile.

These steps are repeated for each possible far-field phase distribution (cf. section 5.4.2.2), then the phase profile producing the best radiation pattern is automatically selected. This method produces the Global phase grating design, which can be non-periodic and have any shape. The successive steps of the program are indicated on figure 5.11 by the numbers 1 to 6.

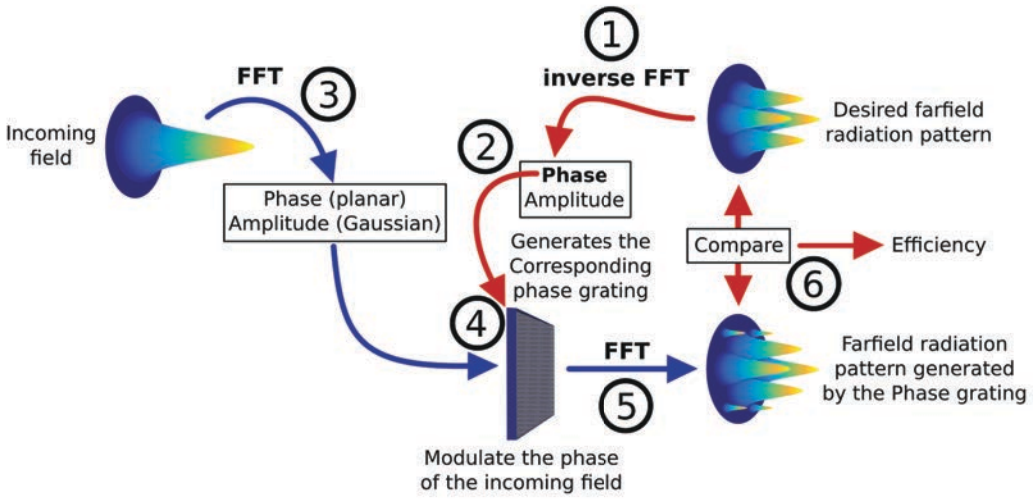

FIGURE 5.11: Schematic of the program calculating the phase profile of the Global grating

5.4.2.2 Different phase distributions in the far-field beam pattern

The far-field beam pattern is composed of Gaussian beams positioned at different positions, but all these beams do not need to have the same phase. Each individual beam must have a uniform and constant phase front, because the mixer it feeds will be less efficient if the incoming beam has a distorted phase front. However, as each beam feeds a different mixer, they can all be phase shifted with one another (as long as there is no cross-correlation of the beams required). This consideration gives an additional degree of freedom. Numerical calculations seem to indicate that the phase profiles giving the best far-field patterns (close to the desired one) are for beam phases of 0 or π rad. So, I decided to successively assign to each beam of the desired far-field pattern, one of these two phase values. As a result, I get 2^N possible far-field patterns (where N is the number of beams). This number can often be reduced by symmetrical considerations. For each of the 2^N (or less) iterations of the main program, the efficiency of the grating is calculated. At the end, the most efficient grating profile is selected.

This process is well illustrated by the design of a 4 beam far-field pattern. For this unique far-field radiation pattern, $2^4 = 16$ possible phase distributions exist, depending whether each beam has a phase of 0 rad or π rad. These 16 phase distributions are reduced to 4 by symmetrical considerations, and are identified in figure 5.12.

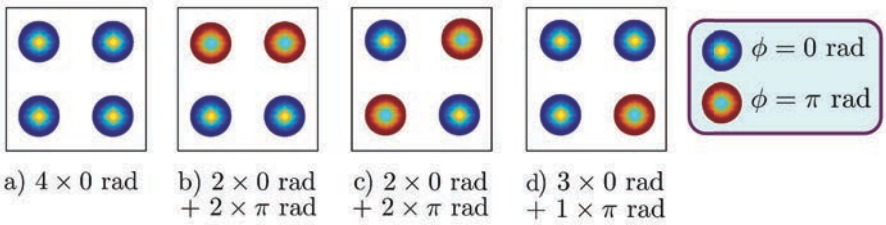

FIGURE 5.12: Desired 4 beam far-field patterns with 4 different phase distributions

These 4 different phase distributions within the desired far-field beam pattern are generated by 3 different phase profiles with different efficiencies, as illustrated by figures 5.13, 5.14 and 5.15. The two first phase distributions (figures 5.12a and 5.12b) are produced by the same phase profile, shown in figure 5.13b. The different phase distributions are produced by a different positioning of the phase profile relative to the beam. When the phase profile is centered on the beam axis the beam pattern shown in figure 5.12a is obtained. When the phase profile is shifted from the beam axis of $1/8^{th}$ of its period in the x and y directions,

the beam pattern shown in figure 5.12b is obtained. Figures 5.13b, 5.14b and 5.15b show the different far-field patterns produced by the corresponding phase profiles. The power percentage of each beam indicates the efficiency of the phase grating. All far-field patterns are perfectly symmetric in both horizontal and vertical directions. The desired beams are the 4 most powerful ones which form a square in the middle of the far-field beam pattern plots. The other smaller beams are unwanted higher order beams.

The first phase grating profile (figure 5.13a) corresponds to a Dammann grating, which means that Dammann gratings are a particular solution of Global gratings. We also see in figure 5.13b that its efficiency is not so good, as each of the 4 main beams only concentrates 20.3 % of the total power. It results in a total power efficiency of 81 %. The remaining 19 % are split between the multiple unwanted higher order beams.

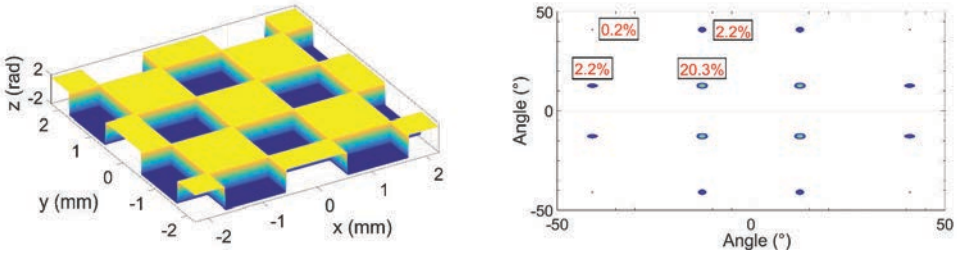

(A) Phase grating profile (B) Far-field beam pattern

FIGURE 5.13: Phase grating generating the far-field pattern of figs. 5.12a and 5.12b

The two other phase grating profiles (figures 5.15a and 5.14a) are partially continuous with some sharp edges. So, these solutions do not belong to the Dammann grating nor the Fourier grating families. We see in figures 5.14b and 5.15b that their efficiencies are better than the one reached by the Dammann grating phase profile (figure 5.13a) and are, respectively, 94.6 % and 92.1 %.

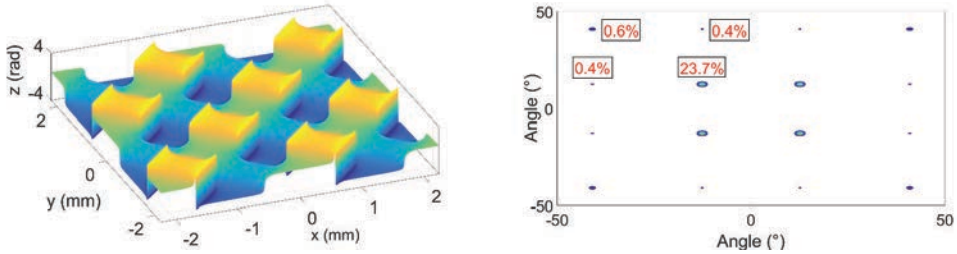

(A) Phase grating profile (B) Far-field beam pattern

FIGURE 5.14: Phase grating generating the far-field pattern of fig. 5.12c

Finally, this code automatically finds the phase profile which generates the desired radiation pattern the which contains the most power. In this example, the 4 beam radiation pattern

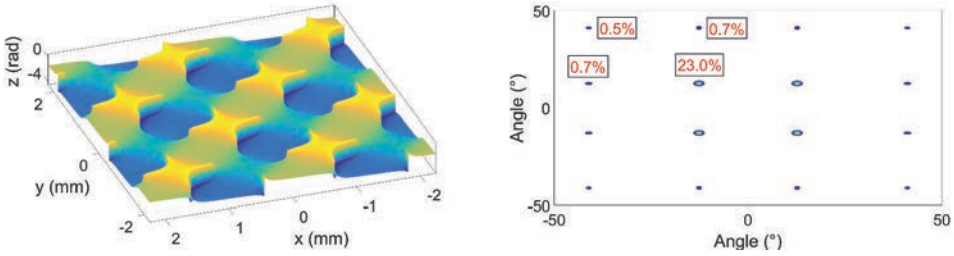

(A) Phase grating profile (B) Far-field beam pattern

FIGURE 5.15: Phase grating generating the far-field pattern of fig. 5.12d

was best generated by the grating design shown in figure 5.14a. This phase grating has a theoretical efficiency of 94.6 % for an angle of 12.6° between each beam and the x and y axises. If we increase this angle, the unwanted higher order beams are at angles larger than 90° and disappear, which greatly improves the grating's efficiency. For example, with the same phase profile and an angle of 20° between the 4 beams and the x and y axises, the grating reaches a theoretical efficiency of 99.99 %.

5.4.3 Conversion of a phase profile into a grating's surface

A phase profile generated by the numerical program can be used to create, either, a transmissive or a reflective phase grating. This phase profile only has to be scaled differently, depending whether we want to use it to create a transmissive or a reflective grating.

5.4.3.1 Surface of a transmissive grating

The relief of the transmissive grating modifies the phase front of the incoming beam because its refractive index is different from the refractive index of the air. So, a phase shift is introduced between different parts of the beam which do not travel along the same electrical distance inside the grating. Equation 5.6 expresses the relation between the height of the grating's relief and the resulting phase modulation.

$$z = \frac{\phi \lambda}{2\pi.(n_{dielec} - n_{air})}, \tag{5.6}$$

where z is the height of the dielectric relief, n_{dielec} is the refractive index of the dielectric, $n_{air} = 1$, and ϕ is the phase shift generated by the dielectric relief.

If the grating is designed for a normal incident beam, the horizontal dimensions (along x and y) of the grating remain the same as in the phase profile generated by the program. Only, the vertical (along z) dimension of this profile needs to be scaled by the previous formula, and the phase relief is converted into an amplitude relief. If the incident beam is not normal to the grating, the surface of the grating profile also has to be scaled in the horizontal direction to compensate for the incidence angle.

5.4.3.2 Surface of a reflective grating

The relief of the reflective grating modifies the phase front of the incoming beam by changing the path length of different parts of the beam. A part of the beam reflected by a high relief will travel a shorter distance in the air than a part of the beam reflected by a lower relief of the mirror. So, a phase shift is introduced between different parts of the beam which do not travel the same distance in the air. This phase modulation is proportional to twice the relief amplitude of the grating, as expressed by the formula:

$$z = \frac{\phi \lambda}{4\pi}, \tag{5.7}$$

where z is the amplitude of the mirror's relief. However, this formula is only valid for an incident beam normal to the mirror's surface. As we do not want the diffracted beams to be reflected back to the source, I designed our reflective grating to receive an oblique incident beam.

We need to know the relation between the relief of the grating and the corresponding phase shift. It is based on equation 5.7 but it also depends on the angle θ of the incident beam. Figure 5.16 illustrates the case where two rays of an oblique incident beam, r_1 and r_2, are reflected by the surface of a grating. They both make an angle θ with the normal of the mirror. r_2 is reflected by a high relief of the grating, while r_1 is reflected by a low relief.

The path difference between the two rays is $\delta_{tot} = \delta_1 + \delta_2$, and z_{obl} is the depth between the considered high and low parts of the surface's relief. The path difference δ_{tot} can be calculated with the following formula,

$$\delta_{tot} = 2z_{obl}.cos(\theta). \tag{5.8}$$

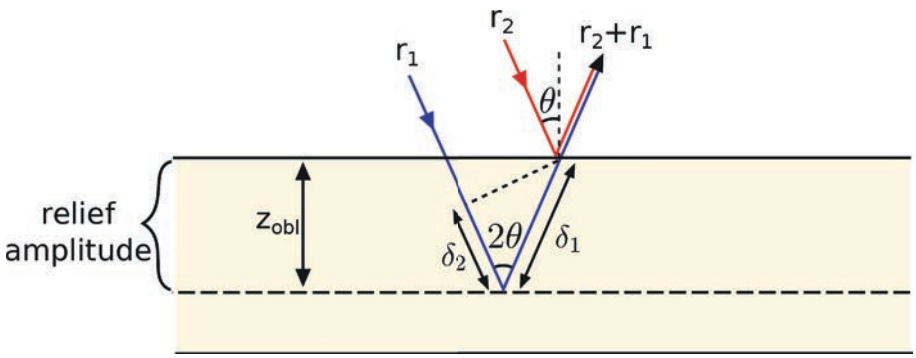

FIGURE 5.16: Reflection of the interfering beams on the surface of a phase grating

Then, the relation between the phase shift ϕ, the depth amplitude z_{obl}, and the incidence angle θ can be deduced:

$$z_{obl} = \frac{\phi\lambda}{4\pi.cos(\theta)} = \frac{z}{cos\theta}. \tag{5.9}$$

The vertical dimension of the phase profile needs to be scaled with equation 5.9, so the phase relief of the grating profile is converted into an amplitude relief. However, as the incident beam is oblique, we also need to scale the horizontal dimension of the phase profile to compensate the angle. We assume that the incoming beam belongs to the plane xz, so the grating has to be scaled along the x direction.

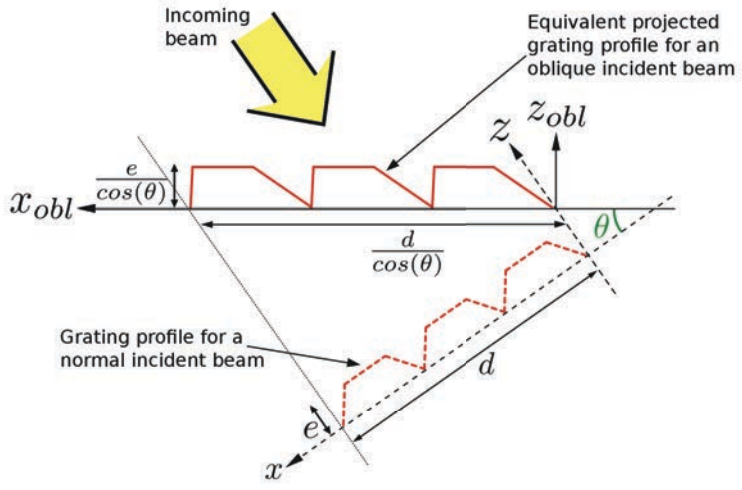

FIGURE 5.17: Example of a projected grating's relief for an oblique incident beam

Figure 5.17 shows how the original phase profile is projected in order to work with an oblique incident angle. The projection changes the shape of the original phase profile, and scales

its horizontal and vertical dimensions. Both x and z dimensions are divided by $cos(\theta)$. The shape of the relief also needs to be modified so the relief reached by the oblique beam corresponds to the initial phase profile relief reached by a normal incident beam. This scaling and shape modification are done with the following formulas:

$$z_{obl} = \frac{z}{cos(\theta)} \tag{5.10}$$

$$x_{obl} = \frac{x}{cos(\theta) + z_{obl}.sin(\theta)} \tag{5.11}$$

5.4.4 Electromagnetic simulations

5.4.4.1 Interest of electromagnetic simulations

Electromagnetic simulations were used to test grating designs produced by the numerical program and to check the efficiency of the design. Electromagnetic simulations are very useful because they take into account more parameters than the numerical program. As electromagnetic simulation software are based on Maxwell's equations, they are able to generate the far-field radiation pattern of a grating without using the FFT function, unlike the numerical program. So, they can accurately simulate the radiation pattern of finite size gratings. Moreover, electromagnetic simulations can take into account lots of parameters, such as the materials' losses, the direction of the source's electric field, diffraction, scattering, the multiples reflexions at the surface of a mirror, etc. It is also possible to modify some parts of the grating's design (due to some manufacturing requirements for example) and simulate the new grating design to evaluate the impact of the changes on the grating's efficiency.

Among the 3 different elecromagnetic software I tested (HFSS, CST and FEKO), FEKO dealt better with the dimensions of the grating and the far-field calculations. So, FEKO is the electromagnetic software I chose to simulate the efficiency of our phase grating designs.

5.5 Reflective and transmissive phase grating prototypes

We decided to make two phase grating prototypes, a transmissive and a reflective one. They both were designed to generate 4 beams out of one incoming Gaussian beam at 610 GHz. In this section, I describe the design, simulation, check and test processes of two phase grating prototypes, according to the following outline:

- Design considerations: Description of the requirements for the two prototypes (number and position of beams, angles, frequency, materials).
- Numerical calculation: Calculation of the phase profile which can efficiently generate the 4 beams.
- Surface definition: The phase profile found by the numerical program is used to calculate the relief's dimensions of the grating prototypes.
- Electromagnetic simulations: The gratings' surface is simulated with FEKO in order to check and improve its efficiency.
- Mechanical design and manufacturing: 3D drawings of the prototypes are created and sent to an external company for manufacturing.
- Geometrical verification: Check of the geometrical dimensions of the manufactured gratings.
- Test of the gratings: Test of the phase grating prototypes' efficiency.
- Conclusion.

In most of these subsections, I successively describe the results concerning the transmissive grating and the reflective grating.

5.5.1 Design considerations for the two prototypes

The development of the phase grating started with the CIDRE project, whose heterodyne receiver was planned to work with 4 pixels at a frequency close to 2.7 THz. For this project, we needed to divide the LO signal into 4 beams to feed 4 HEB (Hot Electron Bolometer)

mixers. As our 2.6 THz LO source does not emit a lot of power (about 2 μW), we needed a very efficient phase grating. The CIDRE project has been suspended, but the development of this new kind of phase grating continues, as it can be very useful for other heterodyne projects or for the CIDRE project if its development is resumed.

We decided to make 2 phase grating prototypes, a transmissive and a reflective one. These gratings were designed to generate a 4 beam radiation far-field pattern from one Gaussian input beam, with the 4 output beams positioned in the 4 corners of a square. This pattern was chosen because we already designed and made an array of 4 HEB mixers for the CIDRE project. For easier testing and manufacturing, the prototypes were designed for 610 GHz with large angles between the 4 beams. The angle of the output beams was set to 12.6° between each beam and the optical axis. The materials of the two prototypes were chosen to comply with the manufacturing company' requirements. The reflective grating was made with brass (ductile and easy to mill) and the transmissive grating was made with TPX® polymethylpentene (PMP) plastic. High density polyethylene (HDPE) has a lower absorption but as it is softer than TPX®, it would have been a lot harder to mill.

5.5.2 Numerical calculation

We applied the numerical program to the desired far-field beam pattern (4 beams positioned in square). The results generated by the program were the 3 different phase profiles shown in figures. 5.13, 5.15 and 5.14. We selected the most efficient of these phase profiles (figure 5.14), which has a theoretical efficiency of 94.6 %. This phase profile will be used to create the transmissive and reflective gratings. In the case of the reflective grating, the incident beam, traveling in the xz plane, will reach the grating with an angle of 25°. To prevent the sharp edges of the phase profile from cutting the incident beam and projecting shadows on the grating's surface, the phase design was rotated by 45°. As shown on figure 5.18, the sharp edges are now along the x axis and do not project any shadow on the phase grating when the input beam is in the xz plane.

As a result, the far-field beam pattern has also been rotated by 45° and is now diamond shaped (figure 5.19).

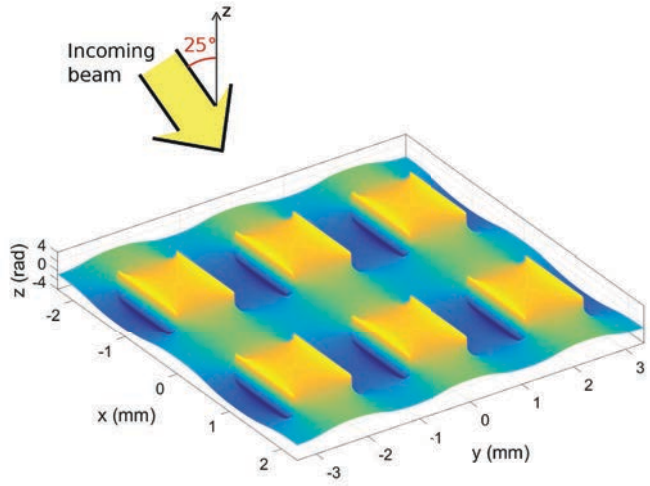

FIGURE 5.18: Reflective phase grating generating a 4 beam far-field pattern

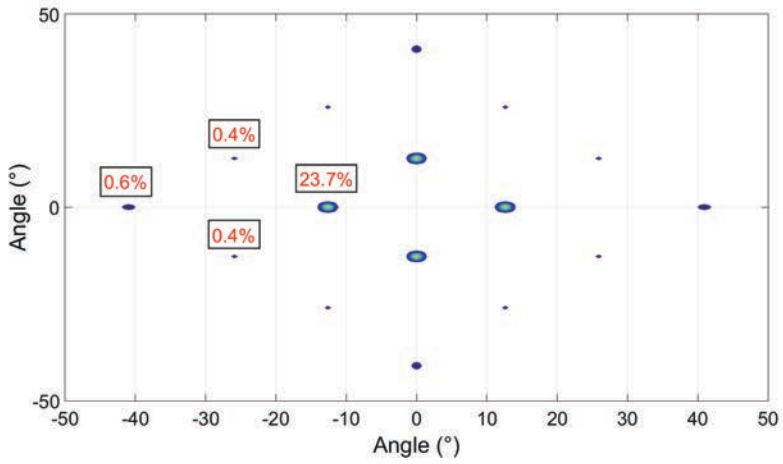

FIGURE 5.19: Far-field generated by the phase profile of figure 5.18

5.5.3 Design of the transmissive and reflective phase gratings

5.5.3.1 Transmissive phase grating

As described in section 5.4.3.1, we need to scale the vertical dimension of the phase profile to convert the phase modulation into a thickness modulation. The transmissive grating is designed for a normal incident beam and will be made out of TPX®. According to the article from Podzorov and Gallot [57], the refractive index of the TPX® at ambient temperature is 1.4565. This value allows us to use equation 5.6, and calculate the amplitude relief of the grating.

5.5.3.2 Reflective phase grating

As for the transmissive grating, we need to scale the vertical dimension of the phase profile to convert the phase relief into an amplitude relief. For the reflective grating, we also need to scale the phase profile in the horizontal direction to compensate for the angle of the oblique incident beam, as explained in section 5.4.3.2. Electromagnetic simulations showed us that large incident angles modify the amplitude and the reflection angle of each of the diffracted beams, with respect to what is theoretically calculated by my numerical program (cf. section 5.5.2). We did not find any satisfying explanation for this effect, but I tried to minimize it by choosing a small incident angle, but large enough to make sure there will not be too many alignment difficulties during the experiment. As a result, I chose an incident beam angle of $\theta = 25°$ to the normal. Equation 5.9 is used to calculate the amplitude relief of the grating's surface. To compensate the effect of the incident angle, the grating profile also has to be scaled in the horizontal direction. As the incoming beam lies in the xz plane, the grating was scaled in the x direction by using equation 5.11.

5.5.4 Electromagnetic simulations

The software FEKO was used to perform the electromagnetic simulations of the phase grating profiles. As explained in section 5.4.4, it enabled me to obtain more precise efficiency and behavior results than with the numerical program. I was able to modify the geometry of the gratings in order to improve their efficiency. The two grating prototypes are perfectly periodic and their surface is made with the basis cell calculated by the numerical program, duplicated along x and y directions. To create gratings larger than the incoming beam, it is necessary to duplicate the basis cell hundreds of times. In my simulations, I approximated the incoming Gaussian beam with a planar wave. This approximation is valid because the cells are much smaller than the Gaussian beam size, and we can consider that the intensity received by each cell is equally distributed over its surface. This planar wave approximation enabled me to use a smaller grating by only duplicating the basis cell a few times, generally to form a 5x5 cell array. By simulating the far-field produced by this smaller grating illuminated with a planar wave, I was able to get accurate results of the diffracted beams' intensity and directivity. However, I could not get valid results concerning the beams' size, because this characteristic is related to the area of the grating illuminated by the incoming beam.

5.5.4.1 Reflective phase grating

Electromagnetic simulations were used to compare the efficiency of the initial grating illuminated with a normal incident wave, and the efficiency of the scaled grating illuminated with a 25° angle incident beam. This comparison is useful to determine the effect of the incident beam angle on the grating's efficiency, and it enabled me to correct some of these effects to improve the grating's efficiency.

Normal incident wave

I first simulated the far-field generated by the initial grating illuminated with a normal incident wave (figure 5.20).

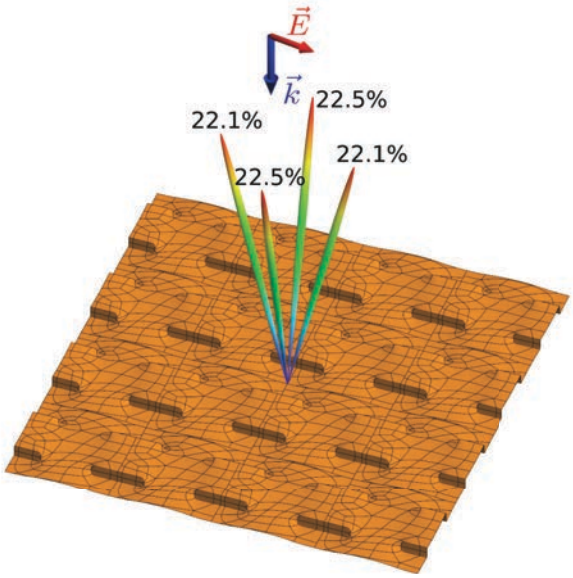

FIGURE 5.20: Far-field pattern of the designed phase grating surface with a normal incident plane wave, simulated with FEKO software

We see that the 4 beams are identical. To get the power percentage of each beam, I simulated the reflection of the plane wave on a flat mirror with the same dimensions as the phase grating. Then, I divided the intensity of the 4 beams generated by the grating, by the intensity of the beam reflected by the flat mirror. By summing the intensity of the 4 beams, I get a total power efficiency of 89.2 % for this grating. It is close to the initial efficiency of 94.6 % predicted by the numerical calculation (cf. section 5.5.2). The 5.4 % difference between both results is due to the multiple side lobes generated by the grating in the electromagnetic simulation. The numerical simulation only considers the power lost by the unwanted

diffraction modes of the main beams, and not the side lobes. Thus it under-estimates the total power losses of the grating.

Oblique incident wave

The angle of the incoming wave was set to 25° and I scaled the grating to adapt its relief to this angle (in accordance with the method described in section 5.4.3.2). The electromagnetic simulation showed an unexpected power disparity between the 4 beams of the far-field pattern, as shown on figure 5.21. Moreover, the total power efficiency of the grating dropped down to 84.8 %, which is 4.4 % below the power efficiency obtained with a normal incident wave.

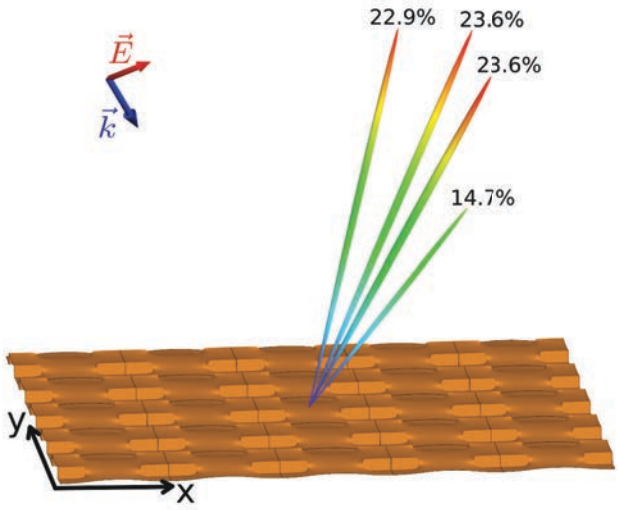

FIGURE 5.21: Far-field pattern of the designed phase grating with a 25° incident plane wave

I solved this disparity by adjusting the requested intensity for each beam in the numerical program, in order to compensate the unbalance shown by the simulation. As a result, it also changed the shape of the phase profile. Figure 5.22 shows the resulting changes in the phase profile.

Figure 5.22 is a top view of the grating. We notice that the sharp edges have been modified. They were initially straight and they are now curved in order to correct the unbalanced beam pattern. Electromagnetic simulations show that this modified phase grating produces a far-field beam pattern with four beams of equivalent intensities, as desired. These four beams are shown on figure 5.23, and we can see that the power difference between them is now less than 2 %.

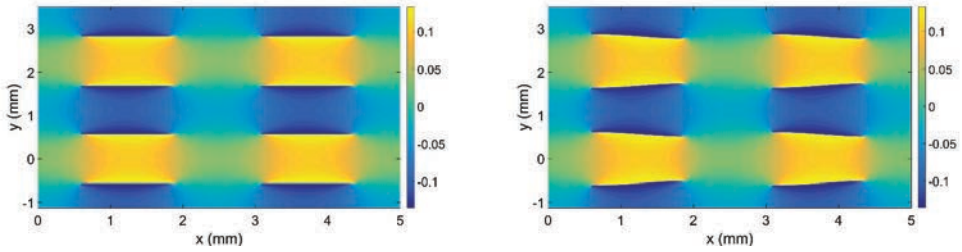

(A) Initial phase profile (B) Modified phase profile

FIGURE 5.22: Modification of the phase profile to compensate the power disparity between the 4 beams

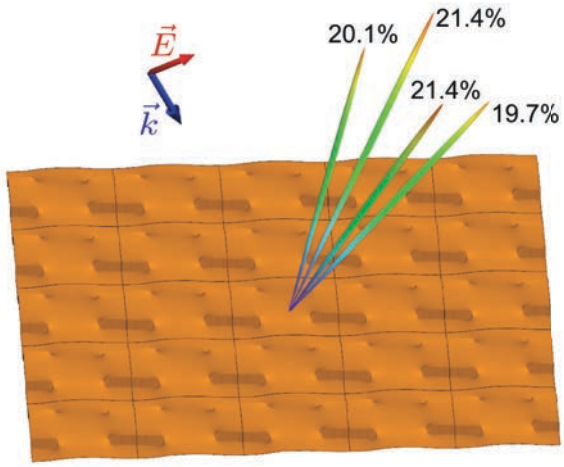

FIGURE 5.23: Far-field pattern of the designed phase grating with a 25° incident plane wave

The vector $\vec{k}$ indicates the direction of the input wave and $\vec{E}$ represents its electric field direction. By summing the intensities of the 4 beams, we find a total efficiency of 82.5 % for the simulated phase grating. This value is 6.7 % lower than the simulated efficiency for the grating with a normal incident wave. We can deduce that, according to electromagnetic simulations, the angle of the incident wave has an important effect on the grating's efficiency, and a grating designed for a normal incident wave has a better efficiency.

5.5.4.2 Transmissive phase grating

The simulation of the transmissive grating was problematic with FEKO because I was not able to accurately simulate the propagation of a Gaussian beam inside a dialectric. Generating a Gaussian beam requires some computing power, and simulating its transmission through a dielectric medium larger than the beam was not possible with our computers. Thus, I was only able to accurately simulate reflective gratings. As both the transmissive

and the reflective gratings are based on the same initial phase profile, I assumed that they would give similar results. So, I approximated the transmissive grating with a reflective grating illuminated by a normal incident plane wave (like the transmissive grating will be). This simulation has already been presented in the previous section 5.5.4.1, and it gave 4 equivalent beams with a total efficiency of 89.2 % (figure 5.20). However, some additional losses have to be considered, as the transmissive grating will absorb and reflect a part of the incoming beam.

5.5.4.3 Expected absorption and reflection losses in the transmissive grating

The transmissive grating, made of TPX®, will generate some inevitable losses. A part of the beam will be reflected at the surface of the grating, because TPX® does not have the same refractive index as air. The beam going through the grating will be attenuated because TPX® is not perfectly transparent at 610 GHz. We need to calculate the losses due to these two contributions in order to properly evaluate the efficiency of the transmissive phase grating. The power absorption coefficient of TPX® is α, in cm^{-1}. The transmission T_{TPX} of a thickness z of TPX® is calculated with Lambert's law (cf. Chantry et al. [58]):

$$T_{TPX} = e^{-\alpha z} \tag{5.12}$$

According to the article from Podzorov and Gallot [57], the power absorption coefficient of TPX® at 610 GHz is about 0.16 cm^{-1}. They also specify that they bought the TPX® from the company Goodfellow, exactly like us. So, the absorption coefficient and refractive index values they found should correspond very well to our TPX®.

The transmitted and reflected power at each side of the grating can be calculated by using Fresnel's formulas (cf. Born and Wolf [59, page 40]). The transmission, reflection and absorption coefficients are illustrated by figure 5.24, where n_1 is the refractive index of air and n_2 the refractive index of TPX®. θ_1 is the angle of the incident beam and θ_2 is the angle of the refracted beam. The TPX® grating has been designed to be used with a normal incident beam, so the angles θ_1 and θ_2 will be very small and close to zero. I_0 is the intensity of the incoming beam, T_{12}, T_{21}, R_{12} and R_{21} are the power transmission and power reflection coefficients at the interfaces $n_1 \rightarrow n_2$ and $n_2 \rightarrow n_1$. T_{abs} is the transmission coefficient of

the material which directly depends on its absorption coefficient (α), as described by the previous formula (Lambert's law), and h is the average thickness of the grating.

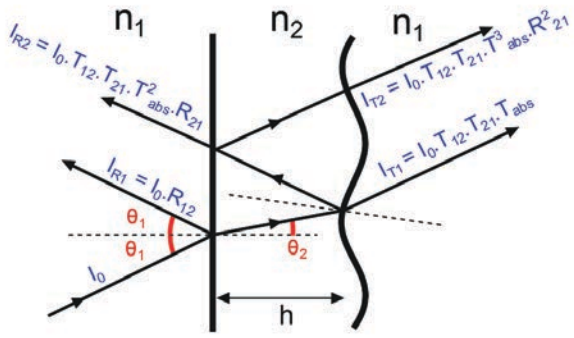

FIGURE 5.24: Intensities transmitted and reflected at the grating's interfaces

From Fresnel's formulas, we are able to calculate the power transmitted by the first beam (I_{T1}) and the power reflected by the first interface (I_{R1}). The other beams are produced by the multiple internal reflections inside the grating. As the surface of the grating is not flat we cannot predict where these beams will be reflected inside the material and where they will come out. So, we consider the corresponding power as lost. The transmission coefficients (T_{12} and T_{21}) depend on the electrical field polarization. However, for small angles, Snell-Descartes' law leads to the following approximation: $n_1\theta_1 \approx n_2\theta_2$. This simplification allows us to have the same transmission coefficients for all electrical field polarizations. The corresponding simplified Fresnel formulas are:

$$T_{12} = T_{21} = \frac{4n_1n_2}{(n_1+n_2)^2} = 0.965 \tag{5.13}$$

$$R_{12} = R_{21} = \left(\frac{n_1-n_2}{n_1+n_2}\right)^2 = 0.035 \tag{5.14}$$

Where n_1 is the refractive index of the air and n_2 is the refractive index of the TPX®. We can now use these formulas to calculate the power percentage transmitted by the transmissive grating:

$$I_{T1} = I_0.T_{12}.T_{21}.T_{abs} = 0.932.I_0.e^{-\alpha.z} \tag{5.15}$$

For a power absorption coefficient $\alpha = 0.16$ cm^{-1} and an average thickness of 2 mm, the total transmitted power is $I_{T1} = 0.902.I_0$. So, about 90 % of the input power should be transmitted by the transmissive grating, and 10 % will be lost, absorbed by the TPX®, reflected, or transmitted after multiple reflections inside the TPX®.

5.5.4.4 Conclusion

Electromagnetic simulations with FEKO enabled me to get more precise estimations of the efficiency of the reflective and transmissive grating prototypes. The reflective grating was simulated with a 25° angle incident beam and the four output beams produced by the grating have approximately the same size and contain 82.5 % of the initial input beam power. The transmissive grating was scaled to be simulated in reflection because transmissive simulations are not very accurate and reliable yet. The four output beams contain 89.2 % of the initial input beam power. This better efficiency is explained because the incident beam is normal to the grating. However, due to the absorption inside the transmissive grating and the reflections at each interface (air-TPX® and TPX®-air), I expect to have 10 % additional losses. So, the estimated efficiency of the transmissive grating is about 79 %.

5.5.5 Mechanical design

The relief of both prototypes was smoothed (interpolated with NURBS surfaces) and converted into a 3D solid with the software Autodesk Inventor. To know what minimum size the phase gratings should have, it is important to consider the size of the incoming beam. The incoming 610 GHz collimated beam I will use with the phase grating has a waist comprised between 5 mm and 10 mm, depending on the focusing element I will use. More than 99 % of the input Gaussian beam energy is included inside a circle whose diameter is 4 times the radius of the beam (as explained in section 4.2.3.2). So, I need to duplicate the basis grating cell enough times to cover a surface larger than 4 times the radius. For the reflective grating, the cells are duplicated 20 times in both directions, generating a surface of 44.8 mm x 49.4 mm. The x dimension is a bit larger than the y dimension because the cell has been scaled to take into account the oblique incident angle. For the transmissive grating, the basis cell is duplicated 19 times in both directions, generating a grating surface with a diameter of 42.6 mm. Both 3D models are shown on figure 5.25. These two 3D designs were sent to the French company Vuichard to be manufactured.

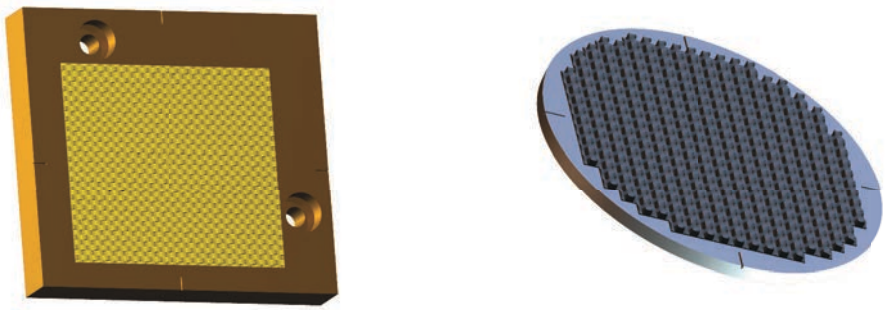

(A) Reflective grating (B) Transmissive grating

FIGURE 5.25: Final 3D designs of the 2 phase grating prototypes

5.5.6 Geometrical measurements of the 2 prototypes

5.5.6.1 Reflective phase grating

The reflective grating is made of brass and was milled with a 200 µm diameter ball-shaped end mill. A picture of the reflective phase grating is shown on figure 5.26. We can notice that the manufactured prototype is optically very close to the initial 3D design shown on figure 5.25A.

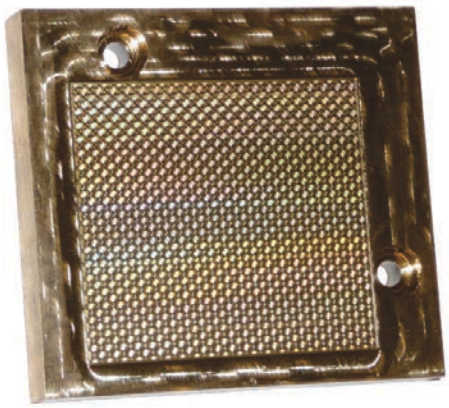

FIGURE 5.26: Manufactured reflective phase grating

We measured the mirror with a microscope to have more precise pictures of its surface (figure 5.27). As we can see on figure 5.27b, the higher and lower parts of the grating do not have the same width, while theoretically they should. The width difference measured with the microscope is (1.12-0.80) = 0.32 mm, which is quite large. This difference was caused

by a machining error which resulted in 30° inclined edges, between the lower and upper parts, instead of vertical edges.

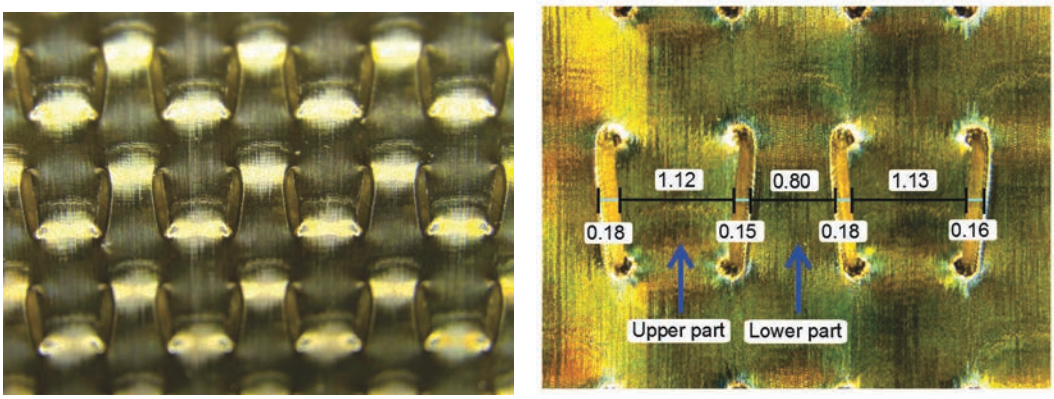

(A) Picture of a central region of the grating (B) Detail of the relief's width (in mm)

FIGURE 5.27: Picture of the reflective phase grating taken with a microscope

Several scans of the mirror have been made with the profilometer, and the 2 most significant are shown by figures 5.28 and 5.29. The scan in the x direction (figure 5.28) shows a very good agreement with the theoretical profile. The maximum error in the vertical direction (along z) is 2 ± 1 μm and the maximum error in the horizontal dirction (along x) is 5 ± 1 μm.

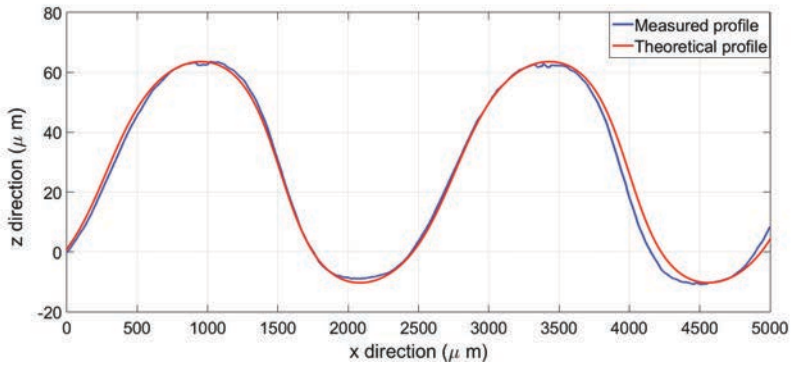

FIGURE 5.28: x scan of the grating's surface

The scan in the y direction (figure 5.29) shows the important error already visible on the microscope photo (figure 5.27b). The edges between the lower and upper parts are oblique and not vertical as they should be. This difference is very important and the microscope pictures show us that it is globally repeated for each cell over the grating's surface. We expect an important impact of this error on the grating's efficiency. The company which manufactured the grating confirmed that they did not define the end mill correctly in the machining program, which resulted in oblique edges instead of vertical edges. The angle of the oblique edges, compared to the vertical axis, is about 30°. As this error considerably

changes the grating's geometry and its efficiency, I simulated the far-field pattern created by our reflective grating with oblique edges. The electromagnetic simulation of this modified model is presented in section 5.5.7.

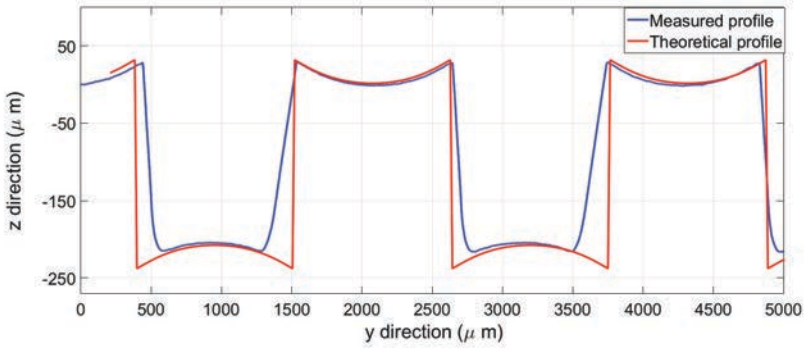

FIGURE 5.29: y scan of the grating's surface

The roughness average of the reflective grating, Ra, has been measured below 0.4 μm, which is very good and better than our requirements.

5.5.6.2 Transmissive phase grating

The geometry of the transmissive grating was not measured because TPX® is quite soft and could be damaged by the very sharp peak of the profilometer. However, the microscope pictures show a good regularity and the cells seem to correspond well to the 3D design (figure 5.30).

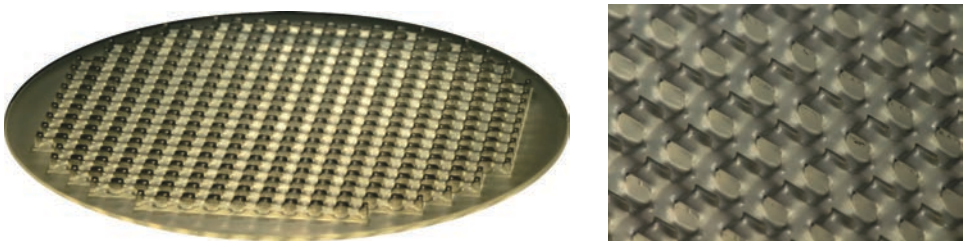

(A) Transmissive phase grating (B) Phase grating zoomed

FIGURE 5.30: Pictures of the transmissive phase grating, made of TPX®

5.5.7 Electromagnetic simulation of the manufactured reflective grating

To match the reflective grating we have received from the manufacturer, I modified the shape of the initial cell of the grating by inclining the vertical edges. I managed to create a modified

design very close to the manufactured grating, with similar inclined edges, as illustrated by figure 5.31b.

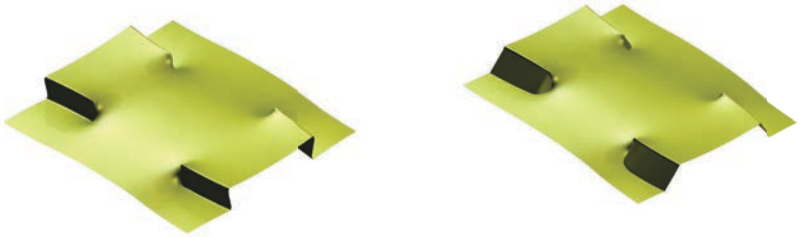

(A) Initial surface with vertical edges (B) Modified surface with oblique edges

FIGURE 5.31: Modification of grating's shape in accordance with the manufactured grating

The modified cell was duplicated to generate the reflective grating surface, and simulated with FEKO to evaluate the change in the far-field produced by the inclination of the edges. The simulation produced the far-field radiation pattern showed on figure 5.32.

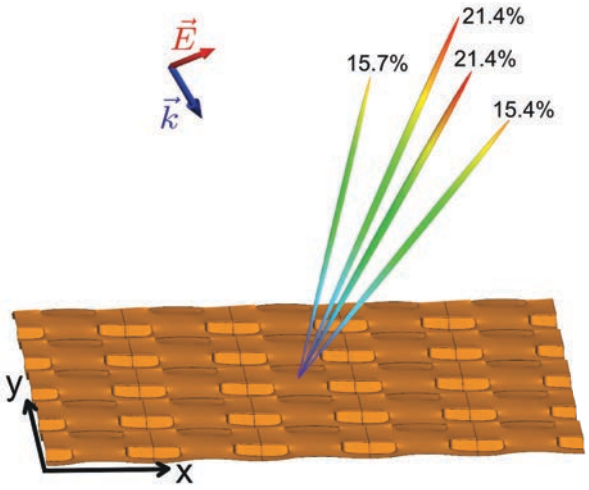

FIGURE 5.32: Far-field pattern generated by the grating with oblique edges

The 2 beams along the y direction are not modified (same angle and same intensity as with the original grating design). However, the power falling in the two beams along the x direction is lower than in the original beam pattern.. This simulation predicts that this shape modification reduces the power of each of these 2 beams by 4.3 %. It gives a total efficiency of 73.9 %, instead of the 82.5 % predicted for the original grating. Finally, this estimation allows us to know what efficiency we can expect from this reflective grating with oblique

edges. We can deduce from this simulation the efficiency we could achieve if the shape of the grating were correct.

5.5.8 Test of the 2 prototypes

To test the two prototypes, I used a 610 GHz LO source to generate the signal, and a Golay cell power meter to measure the power of the beams generated by the gratings. The LO and the gratings were fixed on a rotating platform, so I could easily measure the horizontal radiation pattern of the gratings by rotating the platform. I also set the Golay cell power meter at the same distance from the focusing mirror, with and without the phase grating. So, the beams it saw had always the same size and I compared the power received with and without the phase grating to deduce the relative power of each beam, and the efficiency of the grating.

5.5.8.1 Reflective phase grating

The set-up of the experiment is showed in figure 5.33. To measure the intensity and position of the 2 beams positioned in the horizontal plane, I rotated the platform holding the LO and the grating. To measure the 2 beams positioned in the vertical plane, I vertically translated the Golay power meter and adjusted its inclination. Then, once the Golay power meter was centered on each of these two beams, I rotated the platform to make an horizontal scan of each beam. The accuracy of the measurements is ±1 % and takes into account of the alignment difficulties and the possible power variations of the LO. The Golay power meter was used with a lock-in amplifier to increase its accuracy.

The results of the experiment are showed in figure 5.34. The two horizontal beams (along x direction, as in figure 5.32) contain 16 ± 1 % and 20 ± 1 % of the input beam power. The 2 vertical beams (along y direction, as in figure 5.32) contain 20 ± 1 % of the input beam power. The corresponding efficiency of this reflective phase grating is approximately 76 %, really close to the 73.9 % predicted by the electromagnetic simulation. Moreover, the angles of the beams are very close to the theoretical ±12.6° expected for this phase grating. Figure 5.34 shows the angles of the two beams in the horizontal plane: -12.4 and 13.2 ±0.2°. The angles of the beams in the vertical plane were calculated from distance measurements

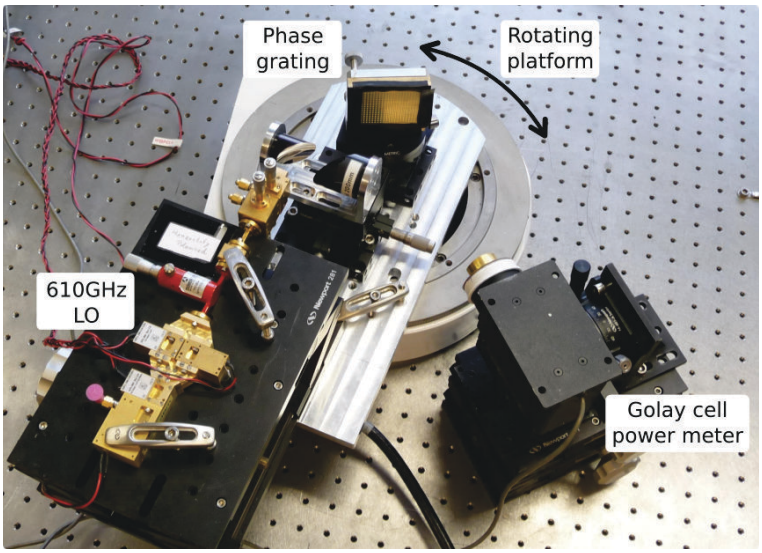

FIGURE 5.33: Set-up of the experiment to measure the efficiency of the reflective phase grating

between the different elements of the set-up. These angles are less accurate, but very close to expected ±12.6°: 11.6 and 12.4 ± − 0.5°.

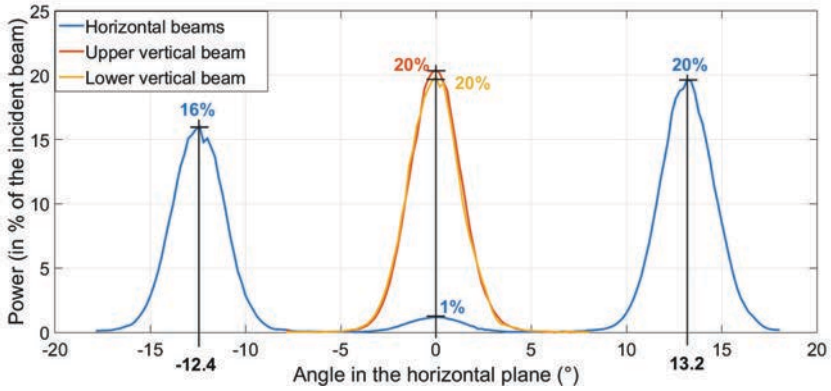

FIGURE 5.34: Power and position of the 4 beams created by the reflective grating

Finally, we can conclude that the efficiency of the reflective phase grating is 76 ± 2 %, and the fours beams are emitted at angles of ±12.6 ± 0.6°. As the efficiency reduction due to the manufacturing error is estimated to about 8.6 %, we can expect the well manufactured reflective grating to have an efficiency about 84 %.

5.5.8.2 Transmissive phase grating

The set-up of the experiment to test the transmissive grating is shown in figure 5.35. I used the same 610 GHz LO source and Golay cell power meter as for the test of the reflective grating. I used a lens made of HDPE (High Density Polyethylene) to focus the LO signal. The rotating platform was holding the LO, the focusing lens and the transmissive grating.

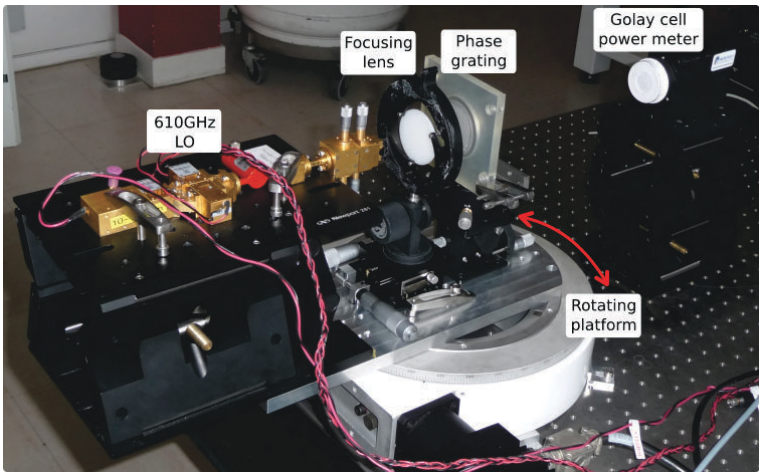

FIGURE 5.35: Set-up of the experiment to test the transmissive grating

By rotating the platform I was able to perform horizontal scans of the beams generated by the phase grating. I measured the intensity and angle of the two beams generated in the horizontal plane. Then, I rotated the transmissive grating by 90° to be able to scan the two other beams. Figure 5.36 shows the intensity of the 4 beams generated by the transmissive phase grating.

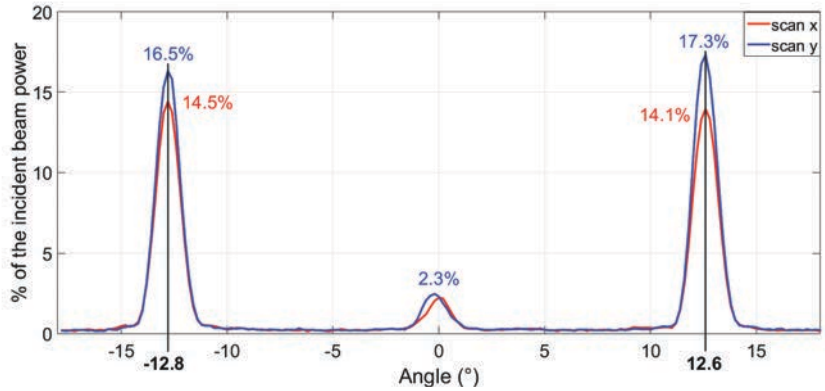

FIGURE 5.36: Power and position of the 4 beams created by the transmissive grating

The two beams of the x scan (along the x direction, as on figure 5.32) are slightly more intense than the two beams of the y scan (along the y direction, as on figure 5.32). The accuracy of these measurements is ±1 %, like for the test of the reflective grating. The angles of the generated beams are very close to the expected 12.6°, with an angle difference smaller than 0.3°. By summing the intensity of the four main beams, we get a total efficiency of 62±2 %. This efficiency is good but lower than expected: the electromagnetic simulation (in reflection) and the expected transmission and reflection losses gave an expected efficiency of 79 %.

Measurement of the TPX® absorption

To obtain the real absorption of our TPX®, I tested a flat sample whose thickness is close to our grating's average thickness. The sample was positioned between the LO and the Golay cell power meter. I compared the power received by the power meter with and without the sample. I rotated the sample between -20° and +20° because the losses change with the beam angle. I measured losses varying between 6 % and 15 %, depending on the angle of incidence. These losses variations have two causes: the power reflected at the interfaces between the sample and the air depends on the angle of incidence of the beam, and the interferences between the beams getting out of the grating after multiple internal reflections also depend on the angle of incidence (cf. 5.5.4.3).

As the machined face of my grating prototype is not flat, the angle between the incident beam and the grating is not constant over the surface and strongly depends on the relief. That is why I expect a smaller variation of the losses with the beam incident angle. This hypothesis is in accordance with my experiment because when I rotated the transmissive grating, the transmittance variation did not exceed 2 %. Therefore, we can estimate that the losses of the TPX® grating are between 6 % and 15 %, and not too dependent on the angle of incidence of the beam. This result is in accordance with the 10 % losses estimated for the TPX® grating in section 5.5.4.3.

Conclusion

We have approximately 17 % difference between the expected efficiency of the transmissive grating prototype (79 %) and the measured one (62 ± 2 %). The different unwanted

diffraction modes seem to be slightly higher than expected (like the mode at 0° which is at 2 %). These diffraction modes are not easily measurable as they are numerous and very weak, but it seems that their intensity is about twice higher than expected. If all these unwanted modes are more intense, it could explain the additional losses. An error during the manufacturing process and some inaccurate dimensions could be the cause of these modes. So, we will try to measure the surface of the transmissive grating without damaging it with the profilometer, and further investigate the simulation with FEKO, to be able to simulate the grating in transmission.

5.5.9 Noise temperature measurement of the receiver with a phase grating

As the phase grating prototypes showed a very good efficiency, I was able to integrate the transmissive grating in our heterodyne receiver and to measure the noise temperature of the receiver at 610 GHz. The noise temperature is an important parameter of heterodyne receivers because it determines their sensitivity. See section 2.3.2 for a description of the noise temperature measurement. The goal of this experiment was to make sure that one of the beams created by the phase grating could pump our HEB mixer, and that the phase grating was not reducing the sensitivity of the receiver. I positioned the grating just before the beam splitter, as shown on figure 5.37.

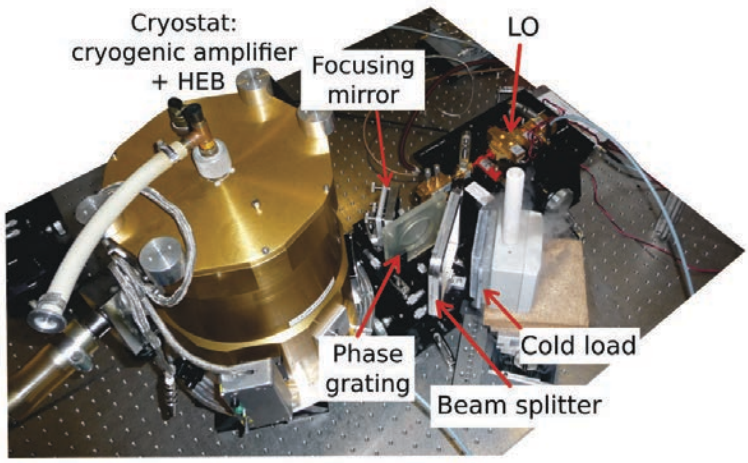

FIGURE 5.37: Set-up of the noise temperature measurement with the transmissive phase grating

The LO beam was divided into 4 beams which were all reflected by the beam splitter. The 4 of them were superimposed with the hot or cold load signal which was transmitted by the beam splitter. Finally, I positioned the HEB mixer to receive one of these four beams and I

measured the IF power when the receiver was seeing a hot or a cold load. The difference between these two power measurements enabled me to calculate the noise temperature of the heterodyne receiver. I measured the noise temperature with and without the phase grating to see if it induces a sensitivity loss for the receiver (figure 5.38).

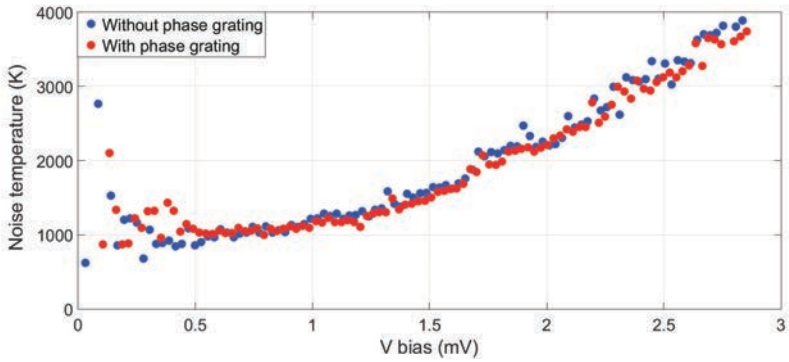

FIGURE 5.38: Noise temperature of the receiver, with and without the phase grating

I obtained approximately the same noise temperature with and without the phase grating. When using the HEB mixer, I need to bias it to a very sensitive point (with a low noise temperature), but also to a stable point, in order to get reliable measurements. Bias points fulfilling these requirements are usually located between 0.5 mV and 1 mV. Within this range, I obtained a noise temperature of 1000 Kelvins which is acceptable for a HEB based heterodyne receiver. This test proves that the phase grating prototypes do not have any effect on the sensitivity of the receiver, and are ready to be included in our next 4 pixel heterodyne receiver.

5.6 Conclusion

Phase gratings are used in most multi-pixel THz heterodyne receivers to split the LO signal into multiples beams and specifically illuminate each mixer. Phase gratings used in actual THz heterodyne receivers are either stepped gratings (cf. Dammann and Klotz [51]) or Fourier gratings (cf. Graf and Heyminck [54] [55]). Both kinds of gratings are efficient to generate a limited number of patterns (number and position of beams) and must be periodic. To overcome these limitations, I created a new kind of phase grating, the Global phase grating. It does not have the constraints of stepped and Fourier gratings, and can theoretically produce any kind of far-field pattern.

Two Global phase grating prototypes were made to test the efficiency of this new kind of phase grating. One prototype is a transmissive grating, made out of plastic (TPX®) and the other is a reflective grating made out of brass. Both were designed to generate 4 beams at 610 GHz. The relief geometry of these prototypes is partly continuous and partly discrete. So, this solution is specific to Global phase gratings and does not belong to stepped nor Fourier grating families. After some electromagnetic simulations and 3D mechanical designs, they were both manufactured and tested. I measured an efficiency of 76 ± 2 % for the reflective grating, and 62 ± 2 % for the transmissive grating. Moreover, the efficiency of the reflective grating has been reduced by a machining error. The efficiency of the correctly machined grating is estimated to 84 %.

Finally, these two first phase grating prototypes are successful in dividing the LO beam into 4 approximately equal beams, with a good efficiency. The reflective grating, especially, shows a very good efficiency. The noise temperature test also showed that the phase gratings were not reducing the sensitivity of the receiver. Therefore, they are ready to be used in a multi-pixel heterodyne receiver. The design and production of a 4 beam Global phase grating at 2.6 THz is planned, to be part of our multi-pixel heterodyne receiver.

Chapter 6

Conclusion

The goal of this PhD was to test, improve and characterize a 2.6 THz heterodyne receiver. There are only a handful of heterodyne receivers at such high frequencies, and some aspects are extremely challenging. During the PhD, I especially focused on three major aspects of our prototype heterodyne receiver:

1. The stability of our heterodyne receiver and of its different elements.
2. The coupling between the LO and the RF signals with a Martin Puplett interferometer.
3. The splitting of the LO signal into several beams, in order to feed several mixers and enable us to create a multi-pixel heterodyne receiver.

1) *Stability*: The quality of a heterodyne receiver is defined by two major characteristics, its sensitivity and its stability. The sensitivity (or noise temperature) of our receiver is one of the best worldwide (cf. Delorme et al. [28]), so I concentrated my work on the stability, usually more difficult to measure and quantify. With a stable receiver, the noise integrates down over long timescales. Unstable receivers only allow short integration times without increasing the noise. The more stable the receiver is, the longer it can integrate the observed signal, and the less noisy the measurements are. Because the Allan variance is directly related to the noise present in an instrument's measurement, I used it to calculate the stability of our heterodyne receiver. I wrote an Allan variance calculation program, optimized for our digital spectrometer's data, and I developed a specific measurement process to accurately measure the stability of the different components of our heterodyne receiver. I found that, with the

600 GHz LO, the stability results are comparable to those of other heterodyne receivers, such as GREAT and HIFI. By measuring the Allan variance of all the components of the receiver, I have been able to identify the HEB bias supply and the 1.4 THz LO as the least stable elements.

2) *Optical coupling of LO and RF signals*: At frequencies above 2 THz, multiplier chain local oscillators (LOs) usually do not emit enough power to be used with a beam splitter and efficiently pump a HEB mixer. To overcome this problem, we chose another diplexer for our heterodyne receiver: a Martin Puplett interferometer (MPI). It can transmit the LO signal a lot more efficiently than a beam splitter but it is more complicated to align. The MPI I designed and built was able to transmit 76 % of the LO power at 2.6 THz at the desired polarization, and we estimate a transmittance around 79 % for the RF signal. As a result, this MPI is fully operational and can be used as a diplexer in a 2.6 THz heterodyne receiver.

3) *Splitting of the LO signal*: The future of heterodyne receivers will be in array receivers which will allow us to get detailed spectra of the universe at many positions in the sky simultaneously. I have tackled one of the major challenges of focal plane arrays: the distribution of the local oscillator (LO) to the mixers. Phase gratings are used in other THz receivers to split the LO beam and feed several mixers. However, these existing phase gratings have several limitations, such as the number of beams they can efficiently produce, and the shape they can have. To overcome these limitations, I have developed a more versatile kind of gratings, we called *Global gratings*, which can efficiently produce any number of beams, at any position, with an efficiency equal or better than that of the existing phase gratings at THz frequencies. I wrote a program to numerically calculate the profile of Global phase gratings, and I developed an electromagnetic simulation process to test and improve the design of the gratings. These numerical tools enabled me to design two phase grating prototypes to efficiently split the LO beam into 4 different beams. These two phase grating prototypes, a transmissive and a reflective one, were optimized for 610 GHz (because it is easier to manufacture and to test than at 2.6 THz). The prototypes were tested with a 610 GHz LO and I measured an efficiency of 76 ± 2 % for the reflective grating, and 62 ± 2 % for the transmissive grating. Moreover, the efficiency of the reflective grating is expected to be higher once the machining error will be corrected. The efficiency of the correctly machined grating is estimated to be 84 %. These two first Global phase grating prototypes were successful in dividing the LO beam into 4 approximately equal beams. These excellent results validate

the design and fabrication processes of this new kind of grating. Therefore, Global gratings are ready to be used in the next generation of array receivers.

In conclusion, the work accomplished during this PhD constitutes an important step toward the realization of a very stable and highly sensitive 2.6 THz multi-pixel heterodyne receiver using a MPI diplexer. The future multi-pixel heterodyne receiver could be used in CIDRE, if the project is resumed later, or significantly contribute to international space projects, like Millimetron [1], CCAT [2], GUSSTO or THEO.

Appendix A

Gaussian beam optics

A.1 Theory of the Gaussian beam optics

This section contains a theoretical explanation of Gaussian beam optics' equations. For a more complete description, see Goldsmith [38] and Davis [40].

A.1.1 The wave equation

The distribution of the electric and magnetic field vectors in vacuum and inside materials is accurately described by the Maxwell's equations. Under some conditions listed below, the Maxwell's equations can be used to express the wave equation for the electric field.

- The beam must propagate through an uncharged and non-conducting medium.
- The medium or material crossed by the beam must be linear, uniform, isotropic and homogeneous (the permeability μ and the permittivity ϵ do not vary in the presence of electric or magnetic fields).

All these conditions are easily fulfilled in vacuum or in free space, where the wave equation for the electric field can be written as

$$\nabla^2 \vec{E} = \epsilon\mu \frac{\partial^2 \vec{E}}{\partial t^2}, \tag{A.1}$$

where ∇^2 is the Laplacian operator, $\vec{E}$ is the electric field of the wave, t is the time. In vacuum, $\mu = \mu_0$ and $\epsilon = \epsilon_0$.

A.1.2 The Helmholtz equation

We consider a monochromatic paraxial electromagnetic radiation (paraxial means that the beam propagates close to the optical axis of the system, and makes a small angle with this optical axis). Under this condition, the electric field of the radiation satisfies the Helmholtz equation:

$$\nabla^2 E(x,y,z) + k^2 E(x,y,z) = 0, \tag{A.2}$$

where k is the wave number ($k = 2\pi\nu\sqrt{\epsilon\mu}$) and ν the frequency of the radiation. We assume that the electric and magnetic fields are mutually perpendicular, and also perpendicular to the axis of propagation. One of the solutions of the Helmholtz equation A.2 is a quasi-plane wave propagating along the z axis:

$$E(x,y,z) = u(x,y,z)\exp(-jkz), \tag{A.3}$$

where u is a complex function defining the difference between a plane wave and the considered beam. We substitute the quasi-plane wave solution (equation A.3) in the Helmholtz equation A.2:

$$\frac{\partial^2 u}{\partial x^2} + \frac{\partial^2 u}{\partial y^2} + \frac{\partial^2 u}{\partial z^2} - 2jk\frac{\partial u}{\partial z} = 0. \tag{A.4}$$

A.1.3 The paraxial wave equation

The wave is propagating along the z axis, and, according to the paraxial approximation, the amplitude u along the z axis changes slowly and is small compared to the variations of u along the x and y axises. Therefore, we can consider the third term of equation A.4 as negligible compared to the other terms. This enables us to simplify equation A.4, to finally obtain the paraxial wave equation in cartesian coordinates:

$$\frac{\partial^2 u}{\partial x^2} + \frac{\partial^2 u}{\partial y^2} - 2jk\frac{\partial u}{\partial z} = 0, \tag{A.5}$$

and, in cylindrical coordinates:

$$\frac{\partial^2 u}{\partial x^2} + \frac{\partial^2 u}{\partial y^2} - 2jk\frac{\partial u}{\partial z} = 0. \tag{A.6}$$

The paraxial wave equation A.5 has several solutions, known as Gaussian beam modes. One of these solutions, especially used to determine the Gaussian beam optics equations, is the fundamental Gaussian mode (equation A.7).

A.1.4 The fundamental Gaussian mode equation

This fundamental Gaussian mode, $u(r,z)$, has a Gaussian amplitude distribution in the direction orthogonal to the propagation axis. It corresponds well to the Gaussian beams emitted by our lab sources with feedhorns at THz frequencies. That is why the equations of Gaussian beam optics are well adapted to characterize the propagation of Gaussian beams in quasioptical systems.

$$u(r,z) = \exp\left[-j\left(P(z) + \frac{k}{2q(z)}r^2\right)\right], \tag{A.7}$$

where r is the radial distance to the propagation axis ($r = \sqrt{x^2+y^2}$), $P(z)$ represents a phase shift factor and $q(z)$ is called the beam parameter. We substitute this expression of $u(r,z)$ in the paraxial equation in cylindrical coordinates (equation A.6):

$$-2jk\left(\frac{e^{-jP(z)}}{q} + \frac{\partial e^{-jP(z)}}{\partial z}\right) + \frac{k^2 r^2 e^{-jP(z)}}{q^2}\left(\frac{\partial q}{\partial z} - 1\right) = 0. \tag{A.8}$$

This equation have to be valid for any r and z. As the first part only depends on z while the second part depends on r and z, each of the two parts of this equation must be equal to zero. This condition gives two relations:

$$\frac{\partial q}{\partial z} = 1, \tag{A.9}$$

$$\text{and,} \quad \frac{\partial e^{-jP(z)}}{\partial z} = -\frac{e^{-jP(z)}}{q}. \tag{A.10}$$

A.1.5 Expression of the beam parameter

Equation A.9 has for solution: $q(z) = q(z_0) + (z - z_0)$, where z_0 is the beam waist location on the z axis (see section 4.2.3.1 for the definition of the beam waist). We define $z_0 = 0$, therefore, we have:

$$q(z) = q(0) + z, \tag{A.11}$$

where $q(z)$ is a complex number which depends on the radius of curvature of the beam $R(z)$, and on its radius $\omega(z)$. The radius ω of the beam corresponds to the radial distance at which the electric field is divided by e compared to its value on the axis of propagation. Both ω and R vary with z. The beam parameter can be expressed as,

$$\frac{1}{q(z)} = \frac{1}{R(z)} - \frac{j\lambda}{\pi\omega^2(z)}, \tag{A.12}$$

where λ is the wavelength of the radiation. By injecting this expression of the beam parameter into equation A.7, we obtain:

$$u(r,z) = \exp\left[-j\left(P(z) + \frac{\pi r^2}{\lambda R(z)}\right) - \frac{r^2}{\omega^2(z)}\right], \tag{A.13}$$

because $k = 2\pi/\lambda$. At z=0 and r=0, we have, $u(0,0) = \exp(-jP(0))$. It enables us to deduce the relative field radial distribution at z=0:

$$u(r,0) = u(0,0)\exp\left(\frac{-r^2}{\omega_0^2}\right), \tag{A.14}$$

where ω_0 is the beam waist (which we usually consider positionned at z=0). At z=0, the wavefront of the beam is planar, so the radius of curvature R is infinite. From equations A.11 and A.12, we can now deduce:

$$\frac{1}{q(z)} = \frac{1}{q(0)+z} \qquad \text{and} \qquad q(0) = \frac{j\pi\omega_0^2}{\lambda}, \tag{A.15}$$

$$\text{which gives,} \quad \frac{1}{q(z)} = \frac{1/q(0)}{1+z/q(0)} = \frac{\frac{1}{z}\left(\frac{z\lambda}{\pi\omega_0^2}\right)^2 - j\frac{\lambda}{\pi\omega_0^2}}{1+\left(\frac{z\lambda}{\pi\omega_0^2}\right)^2}. \tag{A.16}$$

A.1.6 The radius of curvature and the beam radius

By using equations A.16 and A.12, we finally deduce some really useful equations describing the evolution of the radius of curvature and the radius of the beam along its propagation axis:

$$R(z) = z + \frac{1}{z}\left(\frac{\pi\omega_0^2}{\lambda}\right)^2, \tag{A.17}$$

$$\omega(z) = \omega_0\sqrt{1+\left(\frac{\lambda z}{\pi\omega_0^2}\right)^2}. \tag{A.18}$$

A.1.7 The phase shift factor

To deduce the complete expression of the fundamental Gaussian mode equation A.7, we need to find the expression of the phase shift factor $P(z)$. As demonstrated by Goldsmith [38, page 15], we have:

$$\frac{e^{-jP(z)}}{e^{-jP(0)}} = \frac{\omega_0}{\omega(z)}e^{j\phi_0(z)}, \tag{A.19}$$

where ϕ_0 is the Gaussian beam phase shift, also called Gouy phase shift. It corresponds to the phase shift between the considered Gaussian beam and a plane wave at the same frequency.

$$tan(\phi_0(z)) = \frac{\lambda z}{\pi\omega_0^2}. \tag{A.20}$$

A.1.8 Final expression of the fundamental Gaussian mode

The equation the Gaussian beam phase shift A.19 is injected into equation A.13 to obtain the complete expression of the fundamental Gaussian beam mode (we assume that $P(0) = 0$ and $e^{-jP(0)} = 1$).

$$u(r,z) = \frac{\omega_0}{\omega(z)} \exp\left(\frac{-r^2}{\omega^2(z)} - \frac{j\pi r^2}{\lambda R(z)} + j\phi_0(z)\right). \tag{A.21}$$

A.1.9 Electric field distribution of a Gaussian beam

The fundamental Gaussian beam mode equation A.21 is used in the solution of the Helmholtz equation A.3 to find the expression of the electric field distribution of a Gaussian beam along its propagation axis.

$$E(r,z) = \frac{\omega_0}{\omega(z)} \exp\left(\frac{-r^2}{\omega^2(z)} - jkz - \frac{j\pi r^2}{\lambda R(z)} + j\phi_0(z)\right). \tag{A.22}$$

Finally, the electric field distribution is normalized, so $\int_0^\infty |E|^2 2\pi r.dr = 1$:

$$E(r,z) = \sqrt{\frac{2}{\pi\omega^2(z)}} \exp\left(\frac{-r^2}{\omega^2(z)} - jkz - \frac{j\pi r^2}{\lambda R(z)} + j\phi_0(z)\right). \tag{A.23}$$

The normalized electric field distribution of a Gaussian beam (equation A.23) enables us to calculate the value of the electric field of the Gaussian beam at any position (r,z).

A.2 Gaussian beam characteristics

Several characteristics of Gaussian beams can be deduced from the equations of section A.1. These characteristics are represented in figure A.1 and the equations describing them are listed in table A.1.

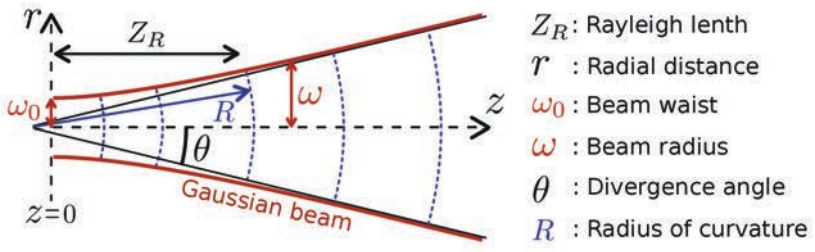

FIGURE A.1: Characteristics of a Gaussian beam

Characteristics	Equations
E field normalized distribution	$E(r,z) = \sqrt{\frac{2}{\pi\omega^2}} \exp\left(\frac{-r^2}{\omega^2} - jkz - \frac{j\pi r^2}{\lambda R} + j\phi_0\right)$
Beam radius	$\omega = \omega_0 \sqrt{1 + \left(\frac{\lambda z}{\pi\omega_0^2}\right)^2}$
Radius of curvature	$R = z + \frac{1}{z}\left(\frac{\pi\omega_0^2}{\lambda}\right)^2$
Beam waist radius	$\omega_0 = \frac{\omega}{\sqrt{1+\left(\frac{\pi\omega^2}{\lambda R}\right)^2}}$
Distance to the beam waist	$z = \frac{R}{1+\left(\frac{\lambda R}{\pi\omega^2}\right)^2}$
Relative power distribution in the radial direction	$\frac{P(r,z)}{P(0,z)} = \exp\left(\frac{-2r^2}{\omega^2}\right)$
Fractional power included in an aperture of radius r	$FP(r) = 1 - \exp\left(\frac{-2r^2}{\omega^2}\right)$
Farfield divergence angle	$\theta = tan^{-1}\left(\frac{\lambda}{\pi\omega_0}\right)$
Rayleigh length	$Z_R = \frac{\pi\omega_0^2}{\lambda}$
Gaussian beam phase shift	$\phi_0 = tan^{-1}\left(\frac{\lambda z}{\pi\omega_0^2}\right)$

TABLE A.1: Gaussian beam optics' main equations

Appendix B

Functioning of the Martin Puplett interferometer

B.1 Rotation of the polarization of the RF signal in the MPI

The MPI is composed of the grid G2 and the two roof-top mirrors, T1 and T2 (figure B.1). The first grid G1 is only used to superimpose the LO and RF signals. The polarizations of the signals s_{LO} and s_{RF} are orthogonal because the LO signal is reflected by the grid G1, while the RF signal is transmitted. The goal of the MPI is to rotate the polarization of one of the two signals. We consider the case where the polarization of the LO signal, initially horizontal, is unchanged while the polarization of the RF signal, initially vertical, is rotated by 90°. So both are horizontally polarized at the output of the MPI.

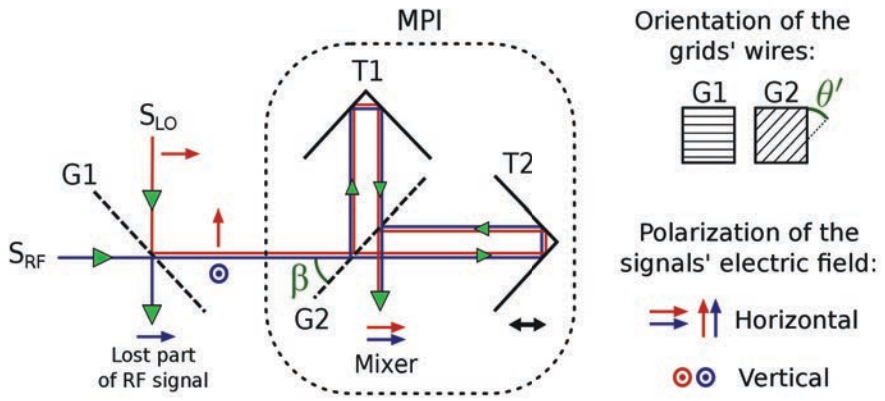

FIGURE B.1: MPI with two grids, to be used with an heterodyne receiver

After being reflected and transmitted by G1, the LO and RF signals reach G2, which makes an angle $\beta = 45°$ with the optical axis. G2 splits each incoming signal into 2 signals with the same power (one is reflected and the other is transmitted). It requires the wires of G2 to be 45° inclined. However, the MPI grid G2 is not perpendicular to the input signals, but makes an angle $\beta = 45°$. So, we have to take into account the projected angle of the grid's wires on the input signal's plane. Figure 4.6 shows this projection and we can deduce that the wires of G2 must have an inclination angle $\theta' = 35.26°$ with the vertical (cf. section 4.3.2.1). The two roof-top mirrors reflect both signals (initially transmitted and reflected by G2) back to G2 (figure B.1). The specificity of roof-top mirrors is that they reflect the signals without changing their polarization (in the referential of the beam), as explained in section 4.3.2.2. However, in the referential of the MPI, the polarization of the signals is rotated by $2\theta = 90°$ when they reach the roof-top mirrors, where θ is the initial polarization of the signals. So, the signal initially transmitted by G2 is reflected by G2, and vice versa. Finally, both signals recombine after G2 at the output of the MPI. The translation of the roof-top mirror T2 changes the path difference ΔZ between the two arms of the MPI ($\Delta Z = ||G2-T1|-|G2-T2||$) and can modify the polarization of any signal going through the MPI:

- If $\Delta Z = n\lambda$, the polarization of the signal going through the MPI is not changed.
- If $\Delta Z = (n + \frac{1}{2})\lambda$, the polarization of the signal going through the MPI is rotated by 90° at the output of the MPI.
- For other values of the ΔZ, the polarization of the signal going through the MPI is elliptic at the output of the MPI.

where $n \in \mathbb{N}$ and λ is the wavelength of the signal.

As the LO and RF signals have slightly different frequencies, there are path differences ΔZ which are equal, at the same time, to $n_1\lambda_{LO}$ and to $(n_2 + \frac{1}{2})\lambda_{RF}$, (with $n_1, n_2 \in \mathbb{N}$). As a result, these path differences ΔZ do not rotate the polarization of the LO signal but rotate the polarization of the RF signal by 90°. Figure B.2 shows how the MPI rotates the polarization of the RF signal without changing the LO signal's one.

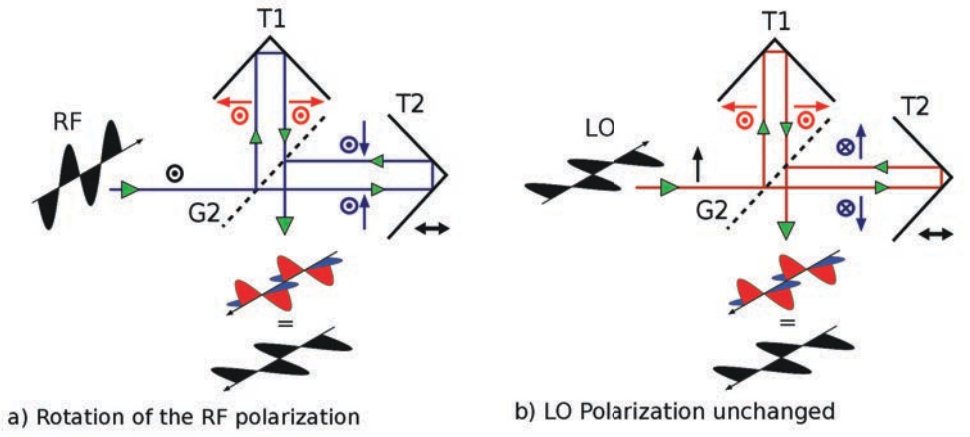

FIGURE B.2: Interferences at the output of the MPI and rotation of only the RF polarization

B.2 Bandwidth of the MPI

For a given path difference ΔZ, only distinct frequencies of the RF spectrum, f_{RF}, are rotated by 90° by the MPI. The polarization of the rest of the RF spectrum stays the same or is elliptical. We consider f_{rf} any frequency of the RF spectrum and calculate how its polarization is rotated by the MPI. The efficiency of the polarization rotation for different RF frequencies f_{rf} by the MPI allows us to calculate the bandwidth of the MPI. The path difference ΔZ between the two arms of the MPI needs to satisfy:

$$\Delta Z = n_1 \lambda_{LO} = \left(n_2 + \frac{1}{2}\right)\lambda_{RF}, \tag{B.1}$$

where n_1 and $n_2 \in \mathbb{N}$, λ_{LO} and λ_{RF} are the wavelengths of the LO and RF signals respectively. Once the RF signal is split by the grid G2, it produces the two signals s_1 and s_2 whose polarizations are, respectively, 45° and -45°. We let A_1 be the amplitude of the signal s_1, and A_2 the amplitude of the signal s_2 when they recombine at the output of the MPI. We consider s_1 at a point M where its amplitude is maximum, so we have $A_1 = \frac{A_0}{\sqrt{2}}$. With A_0 the amplitude of the initial incoming RF signal (before G2). The amplitude A_2 of the signal s_2 at M, for a given path difference ΔZ (optimized for the frequency f_{RF}) depends on the frequency f_{rf} of the RF signal:

$$A_2 = \frac{A_0}{\sqrt{2}} \times cos\left(\frac{2\pi\Delta Z}{\lambda_{rf}}\right). \tag{B.2}$$

By using equation B.1, we can write,

$$A_2 = \frac{A_0}{\sqrt{2}} \times cos\left(\frac{2\pi n_1 f_{rf}}{f_{LO}}\right). \tag{B.3}$$

We now introduce the variable $\delta f = f_{LO} - f_{rf}$, corresponding to the difference between the LO frequency and a frequency f_{rf} of the RF spectrum:

$$A_2 = \frac{A_0}{\sqrt{2}} \times cos\left(\frac{2\pi n_1 (f_{LO} - \delta f)}{f_{LO}}\right) = \frac{A_0}{\sqrt{2}} \times cos\left(\frac{2\pi n_1 \delta f}{f_{LO}}\right). \tag{B.4}$$

We define the frequency difference $\Delta f = f_{LO} - f_{RF}$, where f_{RF} is the RF frequency for which the MPI is optimized:

$$\Delta f = f_{LO} - f_{RF} = c.\frac{\lambda_{RF} - \lambda_{LO}}{\lambda_{RF}\lambda_{LO}}, \tag{B.5}$$

where c is the speed of light.

By combining equations B.1 and B.5, and introducing the variable $\delta n = n_1 - n_2$ ($n_1, n_2 \in \mathbb{N}$), we deduce,

$$\Delta f = \frac{f_{LO}(\delta n - \frac{1}{2})}{n_1}. \tag{B.6}$$

We finally inject this expression in equation B.4 and obtain,

$$A_2 = \frac{A_0}{\sqrt{2}} \times cos\left(\frac{2\pi(\delta n - \frac{1}{2})\delta f}{\Delta f}\right). \tag{B.7}$$

As the s_1 and s_2 signals are polarized at 45° and -45° (due to G2), they both can be divided into vertical and horizontal polarizations ($||\vec{e_v}||$ and $||\vec{e_h}||$).

$$A_1 = \frac{A_0}{\sqrt{2}}\left(cos\frac{\pi}{4}||\vec{e_v}|| + sin\frac{\pi}{4}||\vec{e_h}||\right) = \frac{A_0}{2}||\vec{e_v}|| + \frac{A_0}{2}||\vec{e_h}||. \tag{B.8}$$

$$A_2 = \frac{A_0}{\sqrt{2}} \times cos\left(\frac{2\pi(\delta n - \frac{1}{2})\delta f}{\Delta f}\right)\left[cos\left(-\frac{\pi}{4}\right)||\vec{e_v}|| + sin\left(-\frac{\pi}{4}\right)||\vec{e_h}||\right]. \tag{B.9}$$

$$A_2 = \frac{A_0}{2} \times cos\left(\frac{2\pi(\delta n - \frac{1}{2})\delta f}{\Delta f}\right)||\vec{e_v}|| - \frac{A_0}{2} \times cos\left(\frac{2\pi(\delta n - \frac{1}{2})\delta f}{\Delta f}\right)||\vec{e_h}||. \quad \text{(B.10)}$$

At the output of the MPI, s_1 and s_2 are superimposed, so the amplitude A of the output signal is composed of A_1 and A_2.

$$A = \frac{A_0}{2}\left[1 + cos\left(\frac{2\pi(\delta n - \frac{1}{2})\delta f}{\Delta f}\right)\right]||\vec{e_v}|| + \frac{A_0}{2}\left[1 - cos\left(\frac{2\pi(\delta n - \frac{1}{2})\delta f}{\Delta f}\right)\right]||\vec{e_h}||. \quad \text{(B.11)}$$

We are only interested in the horizontal polarization of the RF signal because, in this example, it is the polarization of the LO signal. So we can plot the power transmission of the horizontal component of the output signal (figure B.3):

$$T = \frac{1}{2}\left[1 - cos\left(\frac{2\pi(\delta n - \frac{1}{2})\delta f}{\Delta f}\right)\right]. \quad \text{(B.12)}$$

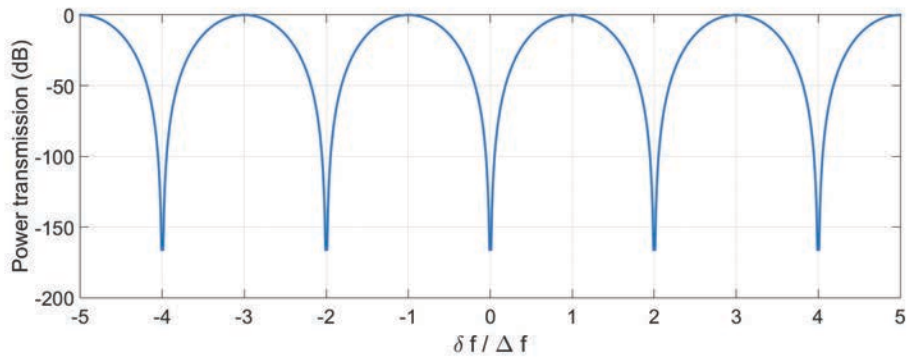

FIGURE B.3: Bandwidth of the MPI for the horizontal component of the RF signal

We can verify that, for $f_{rf} = f_{RF}$, $\delta f/\Delta f = 1$. So, the transmission of the MPI is maximum at the RF frequency line for which the path difference ΔZ was optimized.

B.3 Water vapor absorption

The absorption of the air depends on the precipitable water vapor (pwv) contained in a given path length. This parameter is calculated from the relative humidity (RH) and the temperature of the air. The relative humidity and the temperature first enables us to calculate

the saturated vapor pressure (e_s). To do so, we used the Bolton equation [60] which provides an approximate value of the saturated vapor pressure at a given temperature. This formula is accurate enough in our case, as its error is smaller than 0.3 % when the temperature stays between -35 °C and 35 °C.

$$e_s = 611.2 \times \exp\left(\frac{17.67(T-273.15)}{T-29.65}\right), \tag{B.13}$$

where T is in Kelvins, and e_s in Pascals. It easily allows us to calculate the partial vapor pressure of water (P_{H_2O}) in the air:

$$P_{H_2O} = \frac{RH \times e_s}{100} \qquad \text{where RH is in \%.} \tag{B.14}$$

With the ideal gas law, we calculate the number of moles of H_2O contained inside a volume of 1 $m^2 \times L$, where L is the length of the optical path in the air: $PV = nRT$.

- P is P_{H_2O}, the vapor pressure of water, in Pa
- T is the absolute air temperature, in Kelvins
- R is the universal gas constant (R = 8.314 J.K^{-1}.mol^{-1})
- $V_g = L \times 1$ m^2

It enables us to write:

$$n = \frac{P_{H_2O}.V_g}{RT}, \tag{B.15}$$

from which we deduce the mass of water vapor, M, contained in the volume V_g: $M = n \times M_{H_2O}$. Where M is in grams, and M_{H_2O} (= 18 g.mol^{-1}) is the molar mass of water.

Dividing this mass M by the density of liquid water (1 g.cm^{-3}) gives us the volume of liquid water, V_l (in cm^3), contained inside V_g. We only need to divide both volumes by 1 m^2 to get the thickness of precipitable water vapor (pwv), in cm, corresponding to the water vapor column along the optical path, L, in meters. Finally, we obtain the final formula giving pwv (in mm) as a function of L, T, and RH.

$$pwv(RH, L, T) = \frac{611.2 \times RH \times L \times M_{H_2O} \times 10^{-3}}{8.314 \times T} \times \exp\left(\frac{17.67(T - 273.15)}{T - 29.65}\right), \quad \text{(B.16)}$$

$$pwv(RH, L, T) = 1.323 \times \frac{RH.L}{T} \times \exp\left(\frac{17.67(T - 273.15)}{T - 29.65}\right), \quad \text{(B.17)}$$

where T is the temperature in Kelvins, RH the relative humidity in % and L the optical path length (in m).

Appendix C

Theory of the Dammann grating

C.1 Approximation of the Maxwell's equations

The electromagnetic wave propagation can be calculated with the Maxwell's equations. However, it involves really heavy and complicated calculations. So, this method is not appropriate for iteratively determining the best phase profile to generate the desired farfield beam pattern. In order to quickly calculate the beam pattern created by a phase profile, it is possible to accurately approximate the Maxwell's equations with easier methods, if some requirements are respected. These requirements, listed in O'Shea et al. [53, Chapter 2], are detailed below:

- The beam must propagate through an uncharged and non-conducting medium.
- The medium or material crossed by the beam (in the case of a transmissive grating) must be homogeneous, uniform, isotropic and linear (the permeability μ and the permittivity ϵ do not vary in the presence of electric or magnetic fields).
- The temporal component of the electric field can be ignored.
- The beam must propagate from an input plane, through an aperture plane where is located the phase grating, to an evaluation plane, where the beam pattern is observed.
- The beam size at the position of the aperture plane is large compared with the wavelength.

- The distance between the aperture plane and the output plane is large compared with the wavelength.

Under these requirements, the propagation of the electromagnetic waves can be calculated with the Rayleigh-Sommerfeld integral equation. Moreover, when the distance between the aperture plane (where is located the phase grating) and the output plane (where we observe the beam pattern) is very large compared with the beam diameter (far-field approximation), the Rayleigh-Sommerfeld equation can be simplified. The far-field diffraction pattern of any object located in the aperture plane can, then, be calculated by using a Fourier transform.

In our case, all these requirements are respected and we are only interested in the far-field beam pattern. So, to determine the phase profile which produces the desired far-field beam pattern, the numerical program only relies on the Fourier transform (it uses the fast Fourier transform method). Later, some electromagnetic simulations are performed with a dedicated software, FEKO, based on the Maxwell's equations. This method gives more accurate far-field results but takes a much longer time. I used electromagnetic simulations to check, adjust and improve a phase profile initially calculated by the numerical program.

C.2 Detail of the phase modulation generated by the Dammann grating

The theory of the Dammann grating (DG) is useful to understand the other phase gratings. It has been investigated by several authors, such as Mait et al. [52], O'Shea et al. [53] and, of course, Dammann and Klotz [51]. We consider the case of a transmissive one-dimensional Dammann grating, only composed of periodic grooves, as in figure 5.2a.

The transmission function of a one-dimensional Dammann grating (DG) is $G(u)$. Where u is the spatial coordinate on the surface of the DG. As the DG is periodic, it is more convenient to consider only the transmission function $T(u)$ over one period, Δu, as illustrated by figure C.1. The period of the DG has been normalized to $\Delta u = 1$. The DG is a binary grating which implies a phase step difference of π, so $T(u) = \pm 1$ These phase changes positions are defined by the transition points: z_1, z_2, ..., z_{N_z}. In the case of an even number of transition points, the transmission function $T(u)$ can be defined by the following equation:

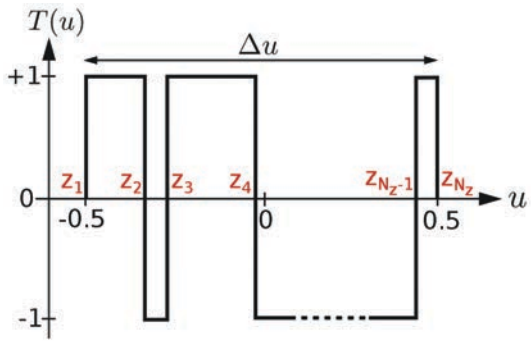

FIGURE C.1: Transmission function of a single period even ordered Dammann grating

$$T(u) = \sum_{k=1}^{N_z-1} (-1)^{k+1} rect\left(\frac{u-(z_{k+1}+z_k)/2}{z_{k+1}-z_k}\right). \tag{C.1}$$

Then, if the DG is very large compared to its period and is larger than the incoming beam, it can be considered as infinite. So, the transmission $G(u)$ can be written:

$$G(u) = T(u) * comb(u) = T(u) * \sum_{m=-\infty}^{\infty} \delta(u - m\Delta u) \tag{C.2}$$

where Δu is the spatial period of the DG, δ the Dirac function, $comb$ the Dirac comb function, and $*$ the convolution sign. The diffraction pattern of the DG, $u(x)$, is given by :

$$u(x) = iFFT[G(u).\Psi(u)] = g(x) * \psi(x), \tag{C.3}$$

where Ψ is the field distribution of the incident beam and $g(x)$ and $\psi(x)$ are the inverse Fourier transforms of $G(x)$ and $\Psi(x)$.

$$g(x) = t(x) \sum_{m=-\infty}^{\infty} \delta(x - m\Delta x). \tag{C.4}$$

The diffraction pattern of the DG directly depends on $t(x)$, the inverse Fourier transform of $T(u)$, the transmission function of the grating's basis cell. In the case of a periodic grating, the diffraction pattern is discrete and composed of several beams emitted at specific angles. These angles are calculated with the grating equation:

$$n\lambda = \Delta u.sin\theta_n, \tag{C.5}$$

where $n \in \mathbb{Z}$ is the considered diffractive order, Δu is the real spatial period of the grating (not normalized), and θ_n is the angle between the order and the normal of the grating. It is illustrated by figure 5.4. In reality, we do not see the diffracted beams of an infinite number of orders, because there cannot be any beam above the angle of 90°. So, the number of visible diffraction orders is $n_{max} = \lfloor n \rfloor$, where $\lfloor \rfloor$ is the floor function.

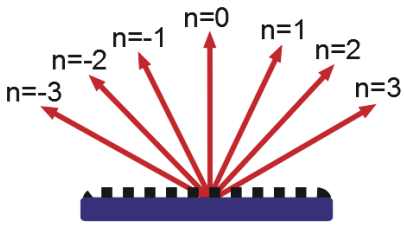

FIGURE C.2: Output beams of all possible diffraction orders

The beams of discrete orders propagate at angles θ_n, therefore the Fourier transform of the grating is only defined for $x = n/\Delta u$. As $\Delta u = 1$, $x = n$. The Fourier transform of the unit cell, $t(n)$, defines the amplitude and relative phase of each diffracted beam whose order is $n \geq 1$.

$$t(n) = \int_{-0.5}^{0.5} T(u).e^{2i\pi un}.du, \tag{C.6}$$

$$t(n) = \sum_{k=1}^{N_z-1} (-1)^{k+1} \int_{z_k}^{z_{k+1}} e^{2i\pi un}.du, \tag{C.7}$$

$$t(n) = \frac{1}{2\pi n} \sum_{k=1}^{N_z-1} (-1)^{k+1} [sin(\alpha_{k+1}) - sin(\alpha_k) + i(cos(\alpha_k) - cos(\alpha_{k+1}))], \tag{C.8}$$

where $\alpha_k = 2\pi n z_k$. The amplitude and phase of the order $n = 0$ beam is calculated by replacing n inside the Fourier transform equation.

$$t(n = 0) = \int_{-0.5}^{0.5} T(u).du, \tag{C.9}$$

$$t(n=0) = \sum_{k=1}^{N_z-1} (-1)^{k+1}(z_{k+1} - z_k). \tag{C.10}$$

To calculate the efficiency of the grating, we use the following equation:

$$\eta(n) = \frac{|t(n)|^2}{\sum_{k=-n_{max}}^{n_{max}} |t(k)|^2}, \tag{C.11}$$

where n_{max} is the maximum number of diffraction orders of the grating. The efficiency corresponds to the power of a given beam, divided by the power of all the visible beams.

C.3 Example of a 1x2 Dammann grating

In the case of a DG dividing 1 incoming beam into 2 diffracted beams, the transmission function of the grating's basis cell only has 4 transition points, as shown in figure C.3.

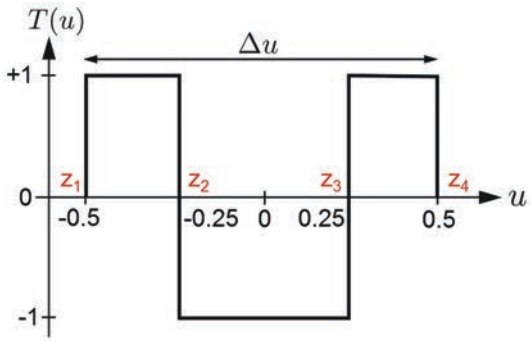

FIGURE C.3: Transmission function of a Dammann grating's basis cell, producing 2 diffracted beams

The diffraction pattern of the grating's basis cell is, for the orders $n \geq 1$:

$$\begin{aligned} t(n) = \frac{1}{2\pi n}[&sin(\alpha_1) - 2sin(\alpha_2) + 2sin(\alpha_3) - sin(\alpha_4) \\ &-i(cos(\alpha_1) - 2cos(\alpha_2) + 2cos(\alpha_3) - cos(\alpha_4))], \end{aligned}$$

$$t(n) = \frac{1}{2\pi n}[-4sin(\alpha_2)] = \frac{-2}{\pi n} sin(2\pi n(-0.25)), \tag{C.12}$$

$$t(n) = \frac{2}{\pi n} sin\left(\frac{\pi n}{2}\right), \tag{C.13}$$

where $\alpha_2 = -\alpha_3 = 2\pi n \times (-0.25)$. For $n = 0$, we calculate: $t(0) = z_1 - 2z_2 + 2z_3 - z_4 = 0$

This example exactly corresponds to the transmissive Dammann grating we bought from Tydex Optics (cf. section 5.2.3). In order to determine the theoretical efficiency of the DG, we need to apply some physical parameters, such as the wavelength λ of the diffracted beam, and the spatial period of the grating, Δu. As measured in the section 5.2.3, the period of the grating is 640 µm, it has been designed to work at a wavelength of $\lambda = 220$ µm. According to the grating equation C.5, it corresponds to a maximum number of order $n_{max} = 2$. From the efficiency equation C.11, we deduce that:

- $\eta(n = 0) = 0$ %
- $\eta(n = 1) = \eta(n = -1) = 50$ %
- $\eta(n = 2) = \eta(n = -2) = 0$ %

For these specific values of λ and θ_1, each beam of the +1 and -1 orders has a theoretical efficiency of 50 %. For a slightly smaller θ_1 angle, we would obtain $n_{max} = 3$, which would reduce the efficiency of the +1 and -1 order beams because some power would be present in the -3 and +3 order beams.

Bibliography

[1] W. Wild, A. Baryshev, T. de Graauw, N. Kardashev, S. Likhachev, G. Goltsman, and V. Koshelets. Instrumentation for millimetron - a large space antenna for thz astronomy. *19th International Symposium on Space Terahertz Technology*, 2008.

[2] S. J. E. Radford, R. Giovanelli, T. A. Sebring, and J. Zmuidzinas. Ccat. *Submillimeter Astrophysics and Technology: A Symposium Honoring Thomas G. Phillips*, 417(ASP Conference Series), 2009.

[3] H-P. Röser. High-resolution heterodyne spectrometer for the kao (kuiper airborne observatory). *Proc. SPIE, Infrared Spaceborne Remote Sensing II*, 2268:263–269, 1994.

[4] D. P. Marrone, R. Blundell, H. Gibson, S. Paine, D. C. Papa, and E. Tong. Characterization and status of a terahertz telescope. *15th International Symposium on Space Terahertz Technology*, 2004.

[5] M. C. Wiedner, S. Bedorf, F. Bielau, M. Emprechtinger, U. E. Graf, and C. E. Honingh. Condor-an astronomical heterodyne receiver at 1.25-1.5 thz. *XXVIII General Assembly of International Union of Radio Sciences (URSI)*, 2005.

[6] M. C. Wiedner, G. Wieching, et al. First observations with condor, a 1.5 thz heterodyne receiver. *Astronomy and Astrophysics*, 454:L33–L36, 2006.

[7] D. Teyssier et al. Herschel/hifi in-flight commissioning and performance. *21st International Symposium on Space Terahertz Technology*, 2010.

[8] F. P. Helmich et al. Herschel-hifi: The heterodyne instrument for the far-infrared. *EAS Publications series*, 52:15–20, 2011.

[9] Th. de Graauw, F. P. Helmich, et al. The herschel -heterodyne instrument for the far-infrared (hifi). *Astronomy and Astrophysics*, 518(L6), 2010.

[10] S. Heyminck, U. U. Graf, R. Güsten, J. Stutzki, and H. W. Hübers. Great: the sofia high-frequency heterodyne instrument. *Astronomy and Astrophysics*, 542(L1), 2012.

[11] C. Risacher, R. Güsten, et al. The upgreat heterodyne array receivers for far infrared astronomy. *39th International Conference on Infrared, Millimeter, and Terahertz waves (IRMMW-THz)*, pages 1–2, 2014.

[12] E. T. Young, E. E. Becklin, et al. Early science with sofia, the stratospheric observatory for infrared astronomy. *The Astrophysical Journal Letters*, 749(2):L17, 2012.

[13] C. K. Walker, C. Kulesa, et al. The stratospheric thz observatory (sto): Preparations for science flight. *22nd International Symposium on Space Terahertz Technology*, 2011.

[14] D. J. Hayton, J. L. Kloosterman, Y. Ren, T. Y. Kao, J. R. Gao, T. M. Klapwijk, Q. Hu, C. K. Walker, and J. L. Reno. A 4.7 thz heterodyne receiver for a balloon borne telescope. *Proc. SPIE, Millimeter, Submillimeter, and Far-Infrared Detectors and Instrumentation for Astronomy VII*, 9153, 2014.

[15] H.B. Callen and T.A. Welton. Irreversibility and generalized noise. *Phys. Rev.*, 83(1): 34–40, 1951.

[16] A. R. Kerr, M. J. Feldman, and S.-K. Pan. Receiver noise temperature, the quantum noise limit, and the role of the zero-point fluctuations. *8th International Symposium on Space Terahertz Technology*, 1997.

[17] E. Kollberg and S. Yngvesson. Quantum noise contribution to the receiver noise temperature of heb thz heterodyne receivers. *13th International Symposium on Space Terahertz Technology*, 2002.

[18] G. Chattopadhyay, I. Mehdi, J. S. Ward, E. Schlecht, A. Skalare, P. H. Siegel, et al. Development of multi-pixel heterodyne array instruments at submillimeter wavelength. *IEEE Asia-Pacific Microwave Conference*, 2004.

[19] A. Maestrini, L. Gatilova, J. Treuttel, F. Yang, Y. Jin, A. Cavanna, D. Moro Melgar, F. Tamazouzt, T. Vacelet, A. Féret, and J-M. Krieg. A 520-620 ghz schottky receiver front-end for planetary science and remote sensing with less than 1500 k dsb noise temperature at room temperature. *36th ESA Antenna Workshop on Antennas and RF Systems for Space Science*, 2015.

[20] J. Treuttel, L. Gatilova, A. Maestrini, D. Moro-Melgar, F. Yang, F. Tamazouzt, T. Vacelet, Y. Jin, A. Cavanna, J. Mateos, A. Féret, and C. Chaumont. A 520-620 ghz schottky receiver frontend for planetary science and remote sensing with 1070k-1500k dsb noise temperature at room temperature. *Accepted to IEEE Transactions on Terahertz Science and Technology*, 2015.

[21] B. Thomas, J. Siles, J. Gill, C. Lee, K. Cooper, A. Maestrini, S. Gulkis, I. Mehdi, et al. 560 ghz, 664 ghz and 1.2 thz schottky based mmic sub - harmonic mixers for planetary atmospheric remote sensing and fmcw radar. *22nd International Symposium on Space Terahertz Technology*, 2011.

[22] M. Carter, B. Lazareff, D. Maier, J.-Y. Chenu, A.-L. Fontana, Y. Bortolotti, C. Boucher, A. Navarrini, S. Blanchet, A. Greve, D. John, C. Kramer, F. Morel, S. Navarro, J. Pe nalver, K. F. Schuster, and C. Thum. The emir multi-band mm-wave receiver for the iram 30-m telescope. *Astronomy and Astrophysics*, 538:A89, 2012.

[23] T de Graauw et al. The atacama large millimeter/submillimeter array. *36th International Conference on Infrared, Millimeter and Terahertz Waves (IRMMW-THz)*, pages 1–4, 2011.

[24] D. Maier, J. Reverdy, L. Coutanson, D. Billon-Pierron, C. Boucher, A. Barbier, et al. Fully integrated sideband - separating mixers for the noema receivers. *25th International Symposium on Space Terahertz Technology*, 2014.

[25] J. L. Hesler, T. Crowe, et al. High-power solid-state terahertz sources. *SPIE Newsroom*, 2015.

[26] Y. Ren, P.J. de Visser, J.N. Hovenier, W. Zhang, P. Khosropanah, J.R. Gao, T.M. Klapwijk, S.C. Shi, T-Y. Kao, S. Kumar, and Q. Hu. 3.5 thz surface emitting distributed feedback qcl operated at 70 k as local oscillator. *21st International Symposium on Space Terahertz Technology*, 2010.

[27] Y. Ren, M. Cui, J.N. Hovenier, J.R. Gao, T.M. Klapwijk, S.C. Shi, T-Y. Kao, Q. Hu, et al. Frequency locking of a 3.5 thz quantum cascade laser using a gas cell. *22nd International Symposium on Space Terahertz Technology*, 2011.

[28] Y. Delorme, R. Lefèvre, W. Miao, A. Féret, W. Zhang, T. Vacelet, F. Dauplay, L. Pelay, J. Spatazza, M. Ba Trung, J-M. Krieg, Y. Jin, P. Khosropanah, and J. R. Gao. A quasi-optical nbn heb mixer with 800k dsb noise temperature at 2.5 thz. *22nd International Symposium on Space Terahertz Technology*, 2011.

[29] R. Lefèvre, Y. Jin, A. Féret, T. Vacelet, W. Miao, L. Pelay, F. Dauplay, M. Ba-Trung, G. Gay, J.-C. Villégier, J. Spatazza, J.-M. Krieg, and Y. Delorme. Terahertz nbn hot electron bolometer fabrication process with a reduced number of steps. *23rd International Symposium on Space Terahertz Technology*, 2012.

[30] D. J. Benford, M. C. Gaidis, and J. W. Kooi. Transmission properties of zitex in the infrared to submillimeter. *10th International Symposium on Space Terahertz Technology*, 1999.

[31] D.W. Allan. *Statistics of atomic frequency standards*. PhD thesis, 1966.

[32] J. A. Barnes. Characterization of frequency stability. *Instrumentation and Measurement, IEEE Transactions*, IM-20(2):105–120, 1971.

[33] R. Schieder and C. Kramer. Optimization of heterodyne observations using allan variance measurements. *Astronomy and Astrophysics*, 373:746–756, 2001.

[34] J. W. Kooi. Advanced receivers for submillimeter and far infrared astronomy. 2008.

[35] A. Makdissi. Alavar5.2. http://www.alamath.com/alavar/, 2003.

[36] T. Berg, S. Cherednichenko, V. Drakinskiy, P. Khosropanah, H. F. Merkel, E. L. Kollberg, and J. W. Kooi. Stability of heb receivers at thz frequencies. *Proceedings of SPIE*, 5498: 605–615, 2004.

[37] P. R. Roelfsema et al. In-orbit performance of herschel-hifi. *Astronomy and Astrophysics*, 537(A17):1–13, 2011.

[38] P. F. Goldsmith. Quasioptical systems : Gaussian beam quasioptical propogation and applications. 1998.

[39] D. R. Golish. Quasioptical systems & components for terahertz astronomy. 2008.

[40] C. C. Davis. Lasers and electro-optics fundamentals and engineering. 2014.

[41] J. C. G. Lesurf. Millimetre-wave optics, devices and systems. 1990.

[42] A. A. Volkov, B. P. Gorshunov, A. A. Irisov, G. V. Kozlov, and S. P. Lebedev. Electrodynamic properties of plane wire grids. *International journal of infrared and millimeter waves*, 3 (1):19–43, 1982.

[43] A. Blanco, S. Fonti, and A. Piacente. Transmission coefficients of free-standing wire grids in the far infrared: A theoretical approach for easy computation. *Infrared Phys*, 26(6):357–363, 1986.

[44] J. Y. Suratteau and R. Petit. Numerical study of perfectly conducting wire gratings in the resonance domain. *International journal of infrared and millimeter waves*, 6(9): 831–865, 1985.

[45] J. A. Beunen, A. E. Costley, G. F. Neill, C. L. Mok, T. J. Parker, and G. Tait. Performance of free-standing grids wound from 10-um-diameter tungsten wire at submillimeter wavelengths: computation and measurement. *Journal of the Optical Society of America*, 71 (2):184–188, 1981.

[46] J. B. Shapiro and E. E. Bloemhof. Fabrication of wire-grid polarizers and dependence of submillimeter-wave optical performance on pitch uniformity. *International journal of infrared and millimeter waves*, 11(8):973–980, 1990.

[47] S. Paine. am atmospheric model. https://www.cfa.harvard.edu/~spaine/am/, 2014.

[48] R. Güsten et al. Champ — the carbon heterodyne array of the mpifr. *Proceedings of SPIE*, 3357, 1998.

[49] U. E. Graf, S. Heyminck, E. A. Michael, S. Stanko, C. E. Honingh, K. Jacobs, R. T. Schieder, J. Stutzki, and B. Vowinkel. Smart: The kosma sub-millimeter array receiver for two frequencies. *Proceedings of SPIE*, 4855:322–329, 2003.

[50] C. E. Groppi, C. K. Walker, C. Kulesa, D. Golish, A. S. Hedden, and P. Gensheimer. Desertstar: a 7 pixel 345 ghz heterodyne array receiver for the heinrich hertz telescope. *Proceedings of SPIE*, 4855:330–337, 2003.

[51] H. Dammann and E. Klotz. Coherent optical generation and inspection of two-dimensional periodic structures. *Optica Acta*, 24(4):505–515, 1977.

[52] J. N. Mait et al. Design of binary-phase and multiphase fourier gratings for array generation. *Journal of the Optical Society of America*, 7(8), 1990.

[53] D. C. O'Shea, T. J. Suleski, A. D. Kathman, and D. W. Prather. Diffractive optics: Design, fabrication, and test. 2003.

[54] U. U. Graf and S. Heyminck. Fourier gratings as submillimeter beam splitters. *IEEE Trans. on Antennas and Propagation*, 49(4):542–546, 2001.

[55] S. Heyminck, U. U. Graf, et al. Array-receiver lo unit using collimating fourier-gratings. *12th International Symposium on Space Terahertz Technology*, pages 563–570, 2001.

[56] T. Klein, G. Ediss, R. Güsten, H. Hauschildt, C. Kasemann, et al. Lo beam array generation at 480 ghz by use of phase gratings. *8th International Symposium on Space Terahertz Technology*, pages 482–489, 1997.

[57] A. Podzorov and G. Gallot. Low-loss polymers for terahertz applications. *Applied Optics*, 47(18):3254–3257, 2008.

[58] G. W. Chantry et al. Far infrared and millimeter-wave absorption spectra of some low-loss polymers. *Chemical Physics Letters*, 10:473–477, 1971.

[59] M. Born and E. Wolf. Principles of optics. 1970.

[60] D. Bolton. The computation of equivalent potential temperature. *Monthly Weather Review*, 108(7):1046, 1980.